

ASCA Observations of Seyfert 1 galaxies:

III. The Evidence for Absorption & Emission due to Photoionized Gas

I.M. George^{1,2}, T.J. Turner^{1,2}, Hagai Netzer³, K. Nandra^{1,4}, R.F. Mushotzky¹, T. Yaqoob^{1,2}

ABSTRACT

We present the results from a detailed analysis of the 0.6 - 10 keV spectra of 23 *ASCA* observations of 18 objects. We find that in most cases the underlying continuum can be well-represented by a powerlaw with a photon index $\Gamma \sim 2$. However we find strong evidence for photoionized gas in the line-of-sight to 13/18 objects. We present detailed modelling of this gas based upon the ION photoionization code. Other studies have been made of the 'warm absorber' phenomenon but this paper contains the first consideration of the importance of the covering-fraction of the ionized gas and a direct comparison between models of attenuation by ionized versus neutral material.

We find the X-ray ionization parameter for the ionized material is strongly peaked at $U_X \sim 0.1$. The column densities of ionized material are typically in the range $N_{H,z} \sim 10^{21}-10^{23} \text{cm}^{-2}$, although highly ionized (and hence psuedo-transparent) column densities up to 10^{24}cm^{-2} cannot be excluded in some cases. We also investigate the importance of the emission-spectrum from the ionized gas, finding that it significantly improves the fit to many sources with an intensity consistent with material subtending a large solid angle at the central source. Allowing a fraction of the continuum to be observed without attenuation also improves the fit to many sources, and is definitely required in the case of NGC 4151. A deficit of counts is observed at ~ 1 keV in the sources exhibiting the strongest absorption features. We suggest this is likely

¹Laboratory for High Energy Astrophysics, Code 660, NASA/Goddard Space Flight Center, Greenbelt, MD 20771

²Universities Space Research Association

³School of Physics and Astronomy and the Wise Observatory, The Beverly and Ramond Sackler Faculty of Exact Sciences, Tel Aviv University, Tel Aviv 69978, Israel.

⁴NAS/NRC Research Associate

to be the signature of a second zone of (more highly) ionized gas, which might have been seen previously in the deep Fe *K*-shell edges observed in some *Ginga* observations. We find evidence that the ionized material in NGC 3227 and MCG-6-30-15 contains embedded dust, whilst there is no such evidence in the other sources

We discuss these results in the context of previous studies and briefly explore the implications in other wavebands.

Subject headings: galaxies:active – galaxies:nuclei – galaxies:Seyfert – X-rays:galaxies

1. INTRODUCTION

Prior to the launch of *ASCA*, the paradigm for Seyfert 1 galaxies, was that the 2–10 keV regime can be well represented by a powerlaw continuum of (photon) index $\Gamma \sim 1.9$ (e.g. Nandra & Pounds 1994). Spectra obtained using the Large Area Counter (LAC) onboard *Ginga* also revealed emission line features superimposed on this underlying ‘primary’ continuum attributable to Fe *K*-shell fluorescence in the 6.4–7.1 keV band. A flattening of the spectra was observed above ~ 10 keV thought to be the ‘Compton-reflection hump’. Evidence for a *K*-shell absorption edge in the 7.1–8.9 keV band due to highly-ionized Fe was also reported in a number of cases (Nandra & Pounds 1994). The combination of these features offers an explanation as to why simple powerlaw models to the data obtained by earlier instruments typically revealed flatter ($\Gamma \sim 1.7$) spectra (e.g. Turner & Pounds 1989). There are a few exceptions to this rule, most notably NGC 4151 which exhibits a continuum noticeably flatter than the average ($\Gamma \sim 1.5$) and absorption within a substantial column of gas ($\sim 10^{22} \text{ cm}^{-2}$) along the line of sight covering most (but possibly not all) of the central continuum (e.g. Yaqoob, Warwick, Pounds 1993 and references therein).

This picture has been generally supported by *ASCA* observations, with the addition that the higher spectral resolution afforded by the onboard instruments have shown the Fe *K α* line to be significantly broadened (Mushotzky et al. 1995; Tanaka et al 1995). However, the situation in the soft (< 1 keV) X-ray regime is somewhat less clear. Historically, a confusing variety of spectral and temporal properties have been seen and/or implied in Seyfert 1 galaxies in the soft X-ray regime. A number of sources seemed to show a steep and rapidly variable ‘soft excess’ which could be characterised by either a low-temperature thermal component (e.g. Arnaud et al. 1985) or a steep second powerlaw (e.g. Turner & Pounds 1989; Turner, George & Mushotzky 1993). Data obtained using the solid-state spectrometer (SSS) onboard the *Einstein Observatory* showed evidence for a complex spectral form in the soft X-ray regime (Turner et al 1991), in some cases this was thought to be due to leakage of the primary continuum through a patchy absorber (e.g. Reichert et al. 1985).

Evidence for absorption by ionized material along the line-of-sight to active galactic nuclei (AGN) was first obtained in observations of the QSO MR2251-178. Using data from the Monitor Proportional Counter (MPC) onboard the *Einstein Observatory*, Halpern (1984) reported the column density in this source to have increased by a factor $\gtrsim 4$ between two observations separated by ~ 1 yr. The excess flux observed in a subsequent observation using the High Resolution Imager (HRI) on the *Einstein Observatory* led Halpern to suggest an explanation in terms of material with a column density $\sim 10^{22} \text{ cm}^{-2}$, but photoionized such as to be transparent below the *K*-edge of OVII at 740 eV. Such an interpretation

was strongly supported by *EXOSAT* observations of MR2251-178. Pan, Stewart & Pounds (1990) found an inverse correlation between the inferred column density and the source flux, and demonstrated that this was consistent with the behaviour expected from photoionized material along the line-of-sight. Similar behaviour was observed in NGC 4151 (Fiore, Perola & Ramano 1990; Yaqoob & Warwick 1991) and MCG-6-30-15 (Nandra, Pounds & Stewart 1990), establishing the effect for low and high luminosity sources. Supporting evidence for such “warm absorbers” was provided by *Ginga* observations of emission-line AGN which revealed iron *K*-shell features in some sources, suggestive of an origin in ionized material with column densities $\gtrsim 10^{23} \text{ cm}^{-2}$. Nandra & Pounds (1994) find this to be a common occurrence, with 12 out of 27 sources in their sample of Seyfert 1 galaxies and Narrow Emission Line Galaxies (NELGs) showing such a component. However, the low spectral resolution of *Ginga* meant that the results were likely to be sensitive to the assumptions concerning the adjacent Fe *K*-shell emission line.

Confirmation of the existence of warm absorbers came from *ROSAT* Position Sensitive Proportional Counter (PSPC) observations, which revealed absorption edges attributable to ionized oxygen in numerous sources (e.g. MCG-6-30-15, Nandra & Pounds 1992; 3C351, Fiore et al. 1993; NGC 3783, Turner et al. 1993a). Early *ASCA* observations (e.g. MCG-6-30-15, Fabian et al. 1994, Reynolds et al. 1995; NGC 3783, George, Turner & Netzer 1995) immediately confirmed the PSPC results and showed evidence for warm absorbers in many other sources (e.g. NGC 3227, Ptak et al 1994; NGC 4051, Mihara et al 1994; Guainazzi et al 1996; EXO 055620-3820.2, Turner, Netzer & George 1996; Mrk 290, Turner et al 1996; PG1114+445, George et al. 1997a). Furthermore Reynolds (1997) finds evidence for such a component in at least half of a sample of *ASCA* observations of 24 type-1 AGN. The presence of highly-ionized, absorbing gas intrinsic to Seyfert 1 nuclei is further confirmed by the presence of ‘associated absorbers’ seen in the UV in many sources. Discussion of these observations and the attempts to relate the UV and X-ray absorbers made to-date is postponed to §8.9.2.

Comparison of *ASCA* data with the predictions of detailed photoionization calculations have revealed spectroscopic evidence for a second ionized absorber in NGC 3516 (Kriss et al. 1996a). In addition the absorption edges due to ionized oxygen appear to vary in a way which is inconsistent with the behaviour of a single absorber in at least some sources. In MCG-6-30-15, the depth of the OVIII edge changes on a timescale $\sim 10^4$ s with no corresponding change in the OVII edge (Reynolds et al 1995; Otani et al. 1996), whilst the converse is true in NGC 4051 (Guainazzi et al. 1996).

The presence of emission lines at energies $\lesssim 1$ keV has been suggested in a number of previous observations (e.g. Turner et al 1991). A blend of emission lines due to OVII

(0.568–0.574 keV) has been claimed in the *ASCA* data from NGC 3783 (George, Turner & Netzer 1995) and potentially seen in other sources (e.g. IC 4329A, Cappi et al. 1996). However the reality of such features has since been disputed, because of the realization of specific inadequacies in the low energy calibration of the *ASCA* instrumentation (see §2.3).

Here we present the third in a series of papers describing the X-ray properties of a sample of 18 Seyfert 1 galaxies, using data obtained by *ASCA*. The sample is comprised of 23 *ASCA* observations of Seyfert class 1.0–1.5 galaxies (as defined by Whittle 1992) performed prior to 1994 May 01. In Nandra et al. (1997a, hereafter Paper I), we presented imaging and timing data for this sample. In that paper we demonstrate that all of the sources show evidence for variability on timescales of minutes-hours, with an amplitude anti-correlated with the source luminosity, confirming previous results. We also showed that for a number of sources the variability amplitude is greater in soft X-rays ($\lesssim 2$ keV) than in hard X-rays (for 10 of the 18 sources on timescales of ~ 1 hr). In Nandra et al. (1997b, hereafter Paper II), we presented the 3–10 keV spectra of the sample sources, and found 14 out of the 18 sources to contain an iron $K\alpha$ line which is resolved in the *ASCA* SIS, with mean width $\sigma \simeq 0.4 \pm 0.1$ keV for a Gaussian profile. However, we found many of the line profiles to be asymmetric, suggesting an origin from the innermost regions of the putative accretion disk.

In this paper, we present the 0.6–10.0 keV spectra of the sample sources. The extension of the spectral analysis down to 0.6 keV requires consideration of the properties of the circumnuclear absorbing material as well as any steepening of the spectrum at low energies. We present detailed modelling of absorption by photoionized material and discuss likely emission contributions as well as combinations of several emission and absorption components. We present the range of properties applicable to our sample, and discuss the characteristics and statistics of the ionized absorbers. We also consider the the importance of allowing a fraction of the underlying continuum to be unattenuated by ionized gas, and the inclusion of the emission features expected from the ionized material. As will become apparent below, there is an obvious variation in signal-to-noise ratio between different datasets and hence there are variations in detectability of the ionized gas. As in the two previous papers our intention is to study the mean properties of the sample and we only include detailed notes on individual sources as an Appendix.

We describe the observations and data reduction in §2, and the photoionization models in §3. Our spectral fitting procedure is introduced in §4, and the results presented in §5 and §6. In §7 we discuss the objects for which there is more than one observation within our sample. Our results are discussed within the general context of the physical properties AGN in §8. We summarize our overall findings in §9 along with outlining a number of important

issues that remain to be resolved.

2. OBSERVATIONS AND DATA REDUCTION

The *ASCA* satellite consists of four identical, co-aligned X-ray telescopes (XRTs; Serlemitsos et al. 1995). Two solid-state imaging spectrometers (known as SIS0 and SIS1), each consisting of four CCD chips, sit at the focus of two of the XRTs, and provide coverage over the ~ 0.4 –10 keV band (Burke et al. 1994). Two gas imaging spectrometers (known as GIS2 and GIS3) sit at the focus of the other two XRTs, and provide coverage over the ~ 0.8 –10 keV band (Ohashi et al. 1996 and references therein). Further details on the satellite, its instrumentation and performance can be found in Tanaka, Inoue & Holt (1994), Makishima et al. (1996), and in the *ASCA Data Reduction Guide*⁵ and references therein.

2.1. The Sample

Our sample is listed in Table 1 along with the redshift (z) of the source, the axial ratio (a/b) of the host galaxy, the effective Galactic hydrogen column density along that line-of-sight ($N_{H,0}^{gal}$) as derived from 21 cm measurements, a number of parameters indicative of the multiwaveband spectra of the objects, and X-ray luminosity in two bands. The mean flux at 220 nm ($\langle f_{220} \rangle$) in the rest-frame of the source, and the mean ratio of the flux at 125 nm (rest-frame) to f_{220} for observations carried out within 48 hours of each other from the *IUE* observations were calculated from Courvoisier & Paltani (1992). The errors quoted for $(f_{125}/f_{220})_{obs}$ and $\langle f_{220} \rangle$ are 1σ or 10%, whichever is the larger, and datasets flagged ‘dubious’ by Courvoisier & Paltani were excluded. The observed flux at 2 keV (f_{2keV}) in the rest-frame of the source is from the best-fitting model presented in §5 (in all cases the statistical error is larger than the differences in f_{2keV} between different models). In the case of objects for which we have more than one dataset, f_{2keV} is the exposure-weighted mean. The radio-to-optical *energy* spectral index, α_{ro} , is calculated using $\langle f_{220} \rangle$ and the observed flux at 5 GHz from Veron-Cetty & Veron (1993). The optical-to-X-ray *energy* spectral index, α_{ox} , is calculated using $\langle f_{220} \rangle$ and f_{2keV} . It should be stressed that these values of α_{ro} and α_{ox} are based non-simultaneous observations and hence should be regarded with appropriate caution. The errors associated α_{ro} and α_{ox} are rather difficult to determine without estimates of the typical amplitude of variability (on timescales of

⁵formerly known as the *ABC Guide to ASCA Data Analysis* and available via <http://heasarc.gsfc.nasa.gov/>

months–years) in each band. Unfortunately, such amplitudes are not well determined for most of the objects considered here. However even assuming a factor 5 variability in each of the three bands (which is likely to be an overestimate in the radio and optical bands), for the typical values of $\alpha_{ro} \sim 0.1$ and $\alpha_{ox} \sim 1.1$ derived for these objects, one obtains relatively small errors of $\sim \pm 0.1$ and $\sim \pm 0.2$ respectively. Finally, Table 1 gives the derived luminosities⁶ of the underlying continuum (i.e. correcting for all line-of-sight absorption) in the (rest-frame) 0.1–10 keV (L_X) and 2–10 keV (L_{2-10}) bands. As in the case of $f_{2\text{keV}}$, these are calculated from the best-fitting model presented in §5, and are exposure-weighted means in the case of objects with multiple datasets. All fluxes and luminosities quoted for the sources will be derived using the SIS0 detector.

2.2. Data Selection

The selection criteria and data analysis methods are presented in Paper I. In summary, we have used data from the US public archive at NASA/GSFC. Standard criteria were applied to reject poor quality data and source spectra extracted using the FTOOLS/XSELECT package for each instrument. Background spectra were extracted from source-free regions of the instrument.

In brief, we consider only the gain-corrected (Pulse Invariant or PI) channels for each instrument⁷. Furthermore, here we consider only the time-averaged spectrum for each instrument during each observation in order to maximize the signal-to-noise ratio. The raw spectra were grouped such that each resultant channel had at least 20 counts per bin, permitting us to use χ^2 minimization in the spectral analysis. All such fits were undertaken using the XSPEC (v9.01) spectral analysis package (Arnaud 1996). Appropriate data redistribution matrices were used (those released 1994 Nov 09 for the SIS, and those released on 1995 Mar 06 for the GIS). The effective area appropriate for each dataset was calculated using `ascaarf`⁸ (v2.5). This does not include a parameterization of the azimuthal dependence of the point spread function which can cause inaccuracies in the normalization, particularly in the case where the source region is not circular. Uncertainties in determining the source centroid can also result in normalization errors, and discrepancies remain between the absolute flux-calibration of the four instruments. These factors lead to cross-calibration uncertainties between the four instruments, but as the point-spread

⁶ $H_0 = 50 \text{ km s}^{-1} \text{ Mpc}^{-1}$ and $q_0 = 0.5$ are used throughout

⁷using `sispi`(v1.0) and the gain-history file released on 1994 Jul 28 in the case of the SIS data

⁸where, in the case of the SIS we used the Gaussian 'fudge', but not the filter 'fudge'

function of the XRT is not strongly dependent on energy, we do not expect them to introduce distortions into the individual spectra. We therefore chose to fit the spectra from all four instruments simultaneously, but allowed the normalization of that model to be free for each detector. For the datasets considered here, the two SIS detectors typically agree in flux to within $\sim 1\text{--}3\%$. The normalization of the GIS detectors are currently forced to agree with the average of the SIS detectors for the Crab.

The observing log is presented in Table 2, where the UTC calendar date is for the start of the observation. As in Papers I & II, we refer to each observation using the name of the source and, in cases where there are multiple observations, the observation number in brackets (using the same numbering scheme⁹ as in Papers I & II). Table 2 contains the exposure time (t_{exp}), the count rate ($Rate$) in the 0.6–10 keV band, and the total number of photons in the 0.6–5.0 keV and 7.0–10 keV bands, for SIS0 (only) after all screening criteria have been applied (N_{phot}). Also listed in Table 2 are the the total number of spectral bins (N_{pts} ; for all instruments) used in the analysis, and the additional number of good-quality spectral bins in SIS0 and SIS1 below 0.6 keV ($\Delta N_{0.6}$). The latter two quantities enable the reader to judge the goodness-of-fit for the results of the spectral analysis presented below. Finally in Table 2 we also provide references to work published previously on each observation.

2.3. Calibration Uncertainties

We wish to fit several spectral features observed in the 0.4–10 keV range. However, there is known to be some uncertainty in the low energy calibration of *ASCA* that must be addressed first. While the origin of this problem is currently unclear (Gendreau, p.comm), the manifestation of the problem is in the lowest channels of the SIS data. Specifically, the *ASCA* Guest Observer Facility at NASA/GSFC reports that SIS spectra from a variety of objects of different astronomical classes consistently indicate uncertainties in the XRT/SIS effective area at energies < 0.6 keV, and especially around 0.5 keV. This has been mainly due to the inability to interpret soft X-ray features in the spectra from 3C 273 (the SIS/GIS cross-calibration target). However, recent simultaneous observations of 3C 273 with *ASCA* and *BeppoSAX* may improve this situation, and already indicate that the systematic error of the SIS relative to the low-energy concentrator system (LECS) on *BeppoSAX* may be no more than $\sim 2 \times 10^{20} \text{ cm}^{-2}$ (Parmar et al 1997). Further details on the low-energy

⁹note that observations which failed to meet our selection criteria are still assigned a number, but not included here – see Paper I for details

calibration of the SIS are given in Dotani et al. (1996) and from the *ASCA* GOF at NASA/GSFC¹⁰

Thus, here we have chosen to ignore all data below 0.6 keV during the spectral analysis, although we do compare the extrapolation of the various best-fitting models below 0.6 keV as a diagnostic of the quality of the fit (see §4.1). For the purpose of this paper, we do not use the 5.0–7.0 keV band data in the fitting process, the consistency of those data with the fits is discussed later. This approach avoids any requirement to include a complex parameterization of the iron K-shell line profile in our consideration of the fits to the broad-band continuum shape. Thus the spectral analysis was performed on simultaneous fits to the 0.6–5.0, 7.0–10.0 keV data. This provides the best method of determining the broad-band X-ray continua. (Note that in all figures presented below which display data/model ratios, the corresponding ratios are included for the 0.4–0.6 keV and 5.0–7.0 keV ranges to illustrate where these data lie with respect to the corresponding model).

3. THE PHOTOIONIZATION MODELS

The ionized absorber/emitter models used in this paper were generated using the photoionization code *ION* (Netzer 1993, 1996, version *ION95*) to calculate the physical state of a slab of gas when illuminated by an ionizing continuum. The code includes all important excitation and ionization processes, full temperature and radiative transfer solutions, and emission, absorption and reflection by the gas are calculated self-consistently assuming thermal and ionization equilibrium. Since the gas temperature is well below the equilibrium plasma temperature, only a few transitions affect the cooling, all of which are included. We assume an ionizing continuum typical of an AGN with a blue bump. Specifically we assume the ‘weak IR’ case of Netzer (1996), with a *photon* index $\Gamma_o = 1.5$ in the optical/UV band from 1.6–40.8 eV, and photon indices in the range $1.5 \leq \Gamma \leq 2.5$ in the X-ray band from 0.2–50 keV. The continuum in the XUV band is also assumed to be a powerlaw connecting the fluxes at 40.8 eV and 0.2 keV, such that the ratio of the fluxes at 250 nm and 2 keV is always $f_{250}/f_{2\text{keV}} = 8.1 \times 10^3$ (corresponding to an optical-to-X-ray *energy* index $\alpha_{ox} = 1.5$ – but see below). Following Netzer (1996), we assume undepleted ‘cosmic abundances’ (with (He, C, N, O, Ne, Mg, Si, S, Fe)/H = (10³, 3.7, 1.1, 8, 1.1, 0.37, 0.35, 0.16, 0.4)/10⁻⁴) and a constant density of $n_H = 10^{10} \text{ cm}^{-3}$ throughout the slab. However it should be noted that as discussed in Netzer (1996), for the same illuminating continuum, a wide range of

¹⁰ for up-to-date information see
<http://heasarc.gsfc.nasa.gov/docs/asca/ascagof.html>

densities ($10^4 \lesssim n_H \lesssim 10^{10} \text{ cm}^{-3}$) give rise to similar equilibrium solutions (and hence similarly shaped absorption/emission models). Thus under steady-state conditions our models are insensitive to the precise value of n_H assumed. The ionization state of the gas is parameterized by the ionization parameter, U_X , defined as

$$U_X = \int_{0.1 \text{ keV}}^{10 \text{ keV}} \frac{Q(E)}{4\pi r^2 n_H c} dE \quad (1)$$

where $Q(E)$ is the rate of photon emission at energy E , r the distance from the source to the illuminated gas. In the past, ionization parameters (defined in various ways) involving an integration of the entire UV–X-ray continuum above 13.6 eV (with an upper limit often set to 13.6 keV) have been commonly used in the literature. As pointed out in Netzer (1996), the use of U_X is preferable in the study of the effects of ionized gas in the X-ray regime as the level of ionization of the dominant species is then directly proportional to U_X . Of course the use of U_X has the additional advantage that it is independent of the form of the continuum assumed in the 13.6–100 eV band which is unobservable due to absorption in our own galaxy for low redshift objects. For convenience, the relationships between U_X and such ionization parameters are shown for a number of spectral forms in Fig. 1. It should be stressed whilst the conversions between U_X and these more traditional ionization parameters are obviously a strong function of the assumed continuum $< 0.2 \text{ keV}$, the values derived for U_X here are almost completely insensitive to such assumptions.

A series of such models were run for various U_X and thicknesses through an illuminated slab, the latter parameterized by the column density of the gas, $N_{H,z}$. Two grids were produced for a number of values of Γ in the above range, and converted to a form able to be used within XSPEC. The first grid consisted of only the absorption (with values between zero and unity) of the incident continuum taking place within the illuminated slab. The assumed ionizing continuum was multiplied by this grid during the spectral analysis, and is referred to as the ionized-absorber below. The axes of this grid are spaced logarithmically over the ranges $3 \times 10^{20} \leq N_{H,z} \leq 6.3 \times 10^{23} \text{ cm}^{-2}$ and $-3 \leq \log U_X \leq 1.0$. Such a model would be applicable if the gas only covers the small fraction of the solid angle surrounding the central source along the line-of-sight (the small clouds case of Netzer 1993).

The second grid of spectra consisted of the continua Compton-scattered by the slab (but including the effects of absorption during its passage through the slab), along with the emission lines and recombination continua produced within the gas. The normalizations, A_{sh} , of the spectra in this grid are calculated by integrating the total emission emerging from the shell. Since to first order this emission is isotropic for the values of $N_{H,z}$ and U_X considered here, A_{sh} can be compared to A_{pl} to give an estimate of the fraction of the hemisphere required to be present in order to produce the observed emission, and hence

the solid angle subtended by the emitting gas at the ionizing source Ω (assuming spherical symmetry). Thus combining these spectra from the 'ionized-emitter' with the effects of the ionized-absorber on the underlying continuum enables us to investigate a range of physically plausible conditions within, and location and geometry of, the photoionized gas.

4. MODEL FITTING

The models considered in the spectral analysis include an underlying continuum which we assume to be a powerlaw of photon index Γ and normalization A_{pl} at 1 keV. In all cases the spectrum emerging from the source passes through a full screen of neutral material at zero redshift. This screen is parameterized by an effective column density $N_{H,0}$ of hydrogen, which is constrained to be $\geq N_{H,0}^{gal}$, the Galactic HI column density along that line-of-sight (Table 1).

We have performed the analysis assuming a variety of spectral models of varying levels of complexity. For the purposes of clarity, we present the results in the following order:

- A The power-law continuum is absorbed by an additional screen of neutral material along the line-of-sight at the redshift of the source (parameterized by an effective column density $N_{H,z}$ of hydrogen). This model therefore has 3 interesting parameters: Γ , $N_{H,z}$ and $N_{H,0}$.
- B As for model A, but where the absorbing material at the redshift of the source is ionized and parameterized by $N_{H,z}$ and ionization parameter U_X (see §3). This model has 4 interesting parameters: Γ , $N_{H,z}$, U_X and $N_{H,0}$.
- C As for model B, but the emission features expected from the ionized gas (with $N_{H,z}$ and U_X) are included, parameterized by Ω , the solid angle subtended by the emitting gas as seen at the central continuum source (see §3). This model has 5 interesting parameters: Γ , $N_{H,z}$, U_X , Ω and $N_{H,0}$.

For each model, the spectral analysis is performed under two assumptions:

- (i) that the absorbing material at the redshift of the source completely covers the source, and that no continuum photons are able to reach the observer via any other light paths. These models are labelled $A(i)$, $B(i)$ and $C(i)$ throughout.
- (ii) that a fraction D_f of the power-law continuum is observed without attenuation at the redshift of the source, whilst $(1 - D_f)$ of the continuum is attenuated by

material along the line-of-sight at the redshift of the source. Of course this is mathematically equivalent to either an absorber within the ‘cylinder-of-sight’ which does not completely cover the central source and/or to a geometry where the central source is completely covered by the absorber but in which some fraction of the radiation emitted by the central source in other directions is scattered back into the line-of-sight without any spectral change. These models are labelled $A(ii)$, $B(ii)$ and $C(ii)$ throughout, and have D_f as an additional interesting parameter.

We have applied all the models to all the datasets, and tabulate all the results even though the additional parameters in the more complex models may not be required by some datasets. This enables us to present the limits on all the parameters with a view to unification schemes. The results assuming models $A(i)$ – $C(ii)$ are presented in §5. A number of additional models are discussed in §6, and notes on individual sources are given in the Appendix. The ultimate goal is to classify objects according to the categories defined above and try to establish the fraction of spectra that require the ionized gas component.

4.1. Model Acceptability

We use a number of criteria to establish whether we consider a model to be consistent with a given dataset. During the spectral analysis we use the χ^2 -statistic to determine the best-fitting model parameters. Thus this statistic is used in conjunction with the number of degrees-of-freedom (dof) to determine the goodness-of-fit over the energy range used during the analysis (*ie* 0.6–5, 7–10 keV). To this end, we use the probability, $P(\chi^2 \mid dof)$, that the statistic should be less than the observed value of χ^2 under the assumption that the model is indeed the true representation of the data. Thus $P(\chi^2 \mid dof) = 0.5$ corresponds to a reduced- χ^2 value of unity, values of $P(\chi^2 \mid dof) \sim 1$ indicate that the data are poorly represented by the model, and values of $P(\chi^2 \mid dof) \sim 0$ indicate that the model is most likely an over-parameterization of the data. For the purposes of this paper, we consider the model to be an adequate description of the data (in the 0.6–5, 7–10 keV band) if $P(\chi^2 \mid dof) \leq 0.95$ (but flag occasions when $P(\chi^2 \mid dof) < 0.05$).

In addition, however, we also require that the best-fitting model extrapolates into the bands excluded from the fit (*i.e.* < 0.6 keV and in the 5–7 keV band). In the light of the uncertainties in the calibration of the instrument at energies < 0.6 keV (§2.3), we quote the ratio of the increase in the χ^2 -statistic to the increase in the number of data points ($\frac{\Delta\chi^2_{0.6}}{\Delta N_{0.6}}$), and the weighted mean of the data/model residuals ($\overline{R_{0.6}}$), when the best-fitting model is extrapolated below 0.6 keV. The rationale behind these two parameters is that

whilst the calibration is suspect at these energies, it is considered unlikely to be in error by $\gtrsim 20\%$. The use of $\frac{\Delta\chi_{0.6}^2}{\Delta N_{0.6}}$ and $\overline{R_{0.6}}$ therefore allows us to identify models, which are deemed acceptable > 0.6 keV, but in which the extrapolation to energies < 0.6 keV is inconsistent with the suspected size of the calibrations uncertainties. For the purposes of this paper, we consider the model to extrapolate to energies < 0.6 keV in an acceptable manner if *either* $\frac{\Delta\chi_{0.6}^2}{\Delta N_{0.6}} \leq 2.0$ *or* $\overline{R_{0.6}}$ lies in the range $0.8 \leq \overline{R_{0.6}} \leq 1.2$. A number of the models include line emission, and clearly we also require that the model does not predict more Fe *K*-shell emission than observed in the 5–7 keV band. The few occasions where this is the case are flagged in the text and tables. We use the *F*-statistic to determine whether the inclusion of an additional free parameter significantly improves the fit. For the number of *dof* typically in these datasets $F \gtrsim 3.8$ and $\gtrsim 6.6$ correspond to improvements at $> 95\%$ and $> 99\%$ confidence respectively.

To summarize, the formal criteria for acceptability used throughout are that $P(\chi^2 \mid dof) \leq 0.95$ *and* either $\frac{\Delta\chi_{0.6}^2}{\Delta N_{0.6}} \leq 2.0$ *or* $\overline{R_{0.6}}$ lies in the range $0.8 \leq \overline{R_{0.6}} \leq 1.2$. However, with the menagerie of objects under investigation, these formal criteria for acceptability were found to be potentially misleading in a number of cases. In such cases somewhat more subjective criteria were used to determine whether the model provided an acceptable representation of the data, but all such cases are noted in the text. For convenience, a summary detailing which models are deemed acceptable for each dataset along with various other notes is provided in Table 12.

5. BASIC MODELS

5.1. Model $A(i)$: Single power law and neutral absorption

The results of the analysis assuming a single underlying powerlaw absorbed by a neutral gas at the redshift of the source, and a neutral gas at zero redshift are listed in Table 3. As well as the best-fitting parameters, Table 3 also lists the total χ^2 -statistic for each fit (χ_{Ai}^2), and the parameters described in §4.1 used to determine the acceptability of the fits. Only 4 datasets fulfill all the formal criteria for acceptability: 3C 120, NGC 6814(1), Mrk 509 and NGC 7469. However inspection of the data/model ratios reveals 4 additional datasets (Fairall 9, NGC 4593, Mrk 841(2) and MCG-2-58-22) which appear to be well represented by the simple powerlaw model. In the case of NGC 4593 and Mrk 841(2), model $A(i)$ provides an adequate description of the data over the 0.6–5, 7–10 keV band, but the best-fitting solution predicts a slight excess of counts ($\overline{R_{0.6}} \sim 1.3$) when the best-fitting model is extrapolated < 0.6 keV. In the case of Fairall 9 and MCG-2-58-22 the data/model residuals indicate that the best-fitting models fail our criteria for acceptability primarily due

to residuals in the 2–4 keV band beyond that expected from statistical considerations alone. This region of the *ASCA* bandpass contains a number of instrumental features, primarily the Au *M*-edge complex due to the coating on the XRTs, suggesting these residuals may arise as a result of slight miscalibration of the Au *M*-edges and/or gain of the detectors at time of these observations (see also Fig. 13). However, since the residuals appear to have little effect on the best-fitting parameters, we consider model $A(i)$ most likely does indeed provide an adequate description of these datasets. A similar problem occurs when a number of the other models are compared to these and other datasets, and all such occurrences are also indicated in Table 12.

It can be seen that the low signal-to-noise ratio of the NGC 6814(1) dataset results in an extremely low value of $\chi^2_{Ai} = 160$ corresponding to reduced χ^2 value of $\chi^2_{\nu} = 0.78$ for 205 *dof*. As reflected in the low value of $P_{Ai} = 0.01$ listed in Table 3, this indicates that for the observation of NGC 6814(1) even this simple model can be considered an over-parameterization of the available data. A similar problem occurs when a number of the other models are compared to other datasets, and all such occurrences are indicated in Table 12. However, it should be noted that the fact that a number of the datasets are adequately described by a simple powerlaw model in the 0.6–6.0 keV band is not purely an artifact of a low signal-to-noise ratio of the observations. Whilst a low signal-to-noise ratio may provide an explanation in the cases of NGC 6814(1) & Mrk 841(2), it certainly does not provide an explanation in the case of the 3C 120 & Mrk 509 datasets which have the *highest* signal-to-noise ratios in our sample (as illustrated by these sources having the highest values of $N_{phot}(SIS0)$ in Table 2). Thus, it is already apparent that some Seyfert 1 galaxies are indeed adequately described by a simple powerlaw, even though the majority are not. (We note, however, that there is evidence for spectral curvature in 3C 120 at energies $\gtrsim 6$ keV – see §6.4.)

Histograms showing the distributions of the photon index (Γ) and intrinsic column density ($N_{H,z}$) for these datasets are shown in Fig 2a and Fig 3a respectively. For these and all the others presented here, the histograms are generated by assigning a rectangle of equal area to each dataset (*not* each object). The width of the rectangle is determined from the 68% confidence range for that parameter as listed in the relevant table (and hence its height derived). We chose such a method as datasets for which the parameter is ill-determined then make wide, flat contributions to the total, whilst datasets for which the parameter is determined very accurately make thin, high contributions (which can visually dominate the total). We feel the resultant plot is a better representation of the results. In all cases the hatched region shows the histogram for the datasets which satisfy all the criteria for acceptability (§4.1). The open histogram shows the effect of also including the datasets which just fail to meet our formal criteria but for which the model is considered likely to be

applicable (as described in the text and summarized in Table 12). As can be seen from Fig 2a, all the datasets for which a simple powerlaw provides an adequate fit have photon indices in the range $1.5 \lesssim \Gamma \lesssim 2$. Furthermore all of these datasets have intrinsic column densities $N_{H,z} \lesssim \text{few} \times 10^{20} \text{ cm}^{-2}$ (Fig 3a) and Galactic column densities ($N_{H,0}$) consistent with those derived from 21 cm measurements (Table 3), although we cannot distinguish between $N_{H,z}$ and $N_{H,0}$ in low-redshift, low- $N_{H,z}$ sources in this sample.

5.2. Model $A(ii)$: Partial-absorption by neutral material

The results of the analysis assuming model $A(ii)$ are listed in Table 4. This model assumes a fraction D_f of the observed continuum is a bare powerlaw whilst a fraction $(1 - D_f)$ is a powerlaw attenuated by neutral gas at the redshift of the source. As stated in §4, such a model is applicable for geometries either where there is an absorber along the line-of-sight which does not completely cover the central source or where the central source is completely covered by the absorber but in which some fraction of the radiation emitted by the central source in other directions is scattered back into the line-of-sight. As can be seen such a model provides a vast improvement in the fits as measured by the reduction in the χ^2 -statistic for the majority of the datasets. Indeed, from the F -statistic (listed as $F(\frac{A(ii)}{A(i)})$ in Table 4) it can be seen that the addition of D_f as a free parameter leads to an improvement over the results obtained assuming model $A(i)$ significant at $>95\%$ confidence for all but 1 dataset (NGC 6814(1)), and at $>99\%$ confidence for all but that dataset and Mrk 841(1,2).

A total of 10 datasets satisfy all our formal criteria for acceptability assuming model $A(ii)$. These include the 4 datasets for which our criteria for acceptability were also satisfied by model $A(i)$, along with the datasets of Mrk 335, NGC 3227, Mrk 766, NGC 4593, Mrk 841(2) and MCG-2-58-22. The histogram of the best-fitting photon indices from the datasets for which model $A(ii)$ provides an adequate description is shown in Fig 2b. It can be seen that the distribution is extended over the range $1.5 \lesssim \Gamma \lesssim 2.5$, but as for model $A(i)$ contains clear evidence for a peak at $\Gamma \sim 2$. The best-fitting solutions to all the datasets have Galactic column densities ($N_{H,0}$) consistent with that derived from 21 cm measurements (Table 3) with the exception of 3C 120 ($\Delta N_{H,0} \simeq 6 \times 10^{20} \text{ cm}^{-2}$) and NGC 7469(2) ($\Delta N_{H,0} \simeq 3 \times 10^{20} \text{ cm}^{-2}$).

The derived model spectra and data/model ratios for the 8 datasets for which model $A(ii)$ is acceptable and offers an improvement at $>99\%$ confidence over model $A(i)$ are shown in Fig 4. For 2 of the remaining datasets (Fairall 9 and IC 4329A) we find model $A(ii)$ to offer a significant improvement over model $A(i)$, yet no significant further improvement

in the goodness-of-fit is obtained assuming subsequent models presented in §5. These two datasets are also shown in Fig 4, despite our formal criteria for acceptability not being satisfied. As can be seen from Table 4, for many of the datasets (Fairall 9, 3C 120, Mrk 841(2), NGC 6814(2), NGC 7469(2) & MCG-2-58-22) the best fitting solution occupies the region of high- $N_{H,z}$, high- D_f parameter-space. This is also clearly apparent from the histograms of $N_{H,z}$ and D_f for these datasets are shown in Figs 3b and 5a (respectively), and gives rise to a relatively subtle upturn in the observed spectrum $\gtrsim 7$ keV in these sources (Fig 4).

It is important to appreciate that given the *ASCA* bandpass (and typical signal-to-noise ratios) we are only sensitive to and/or can constrain $N_{H,z}$ and D_f over a limited range of parameter space. Clearly the model is insensitive to $N_{H,z}$ in all models where $D_f \simeq 1$ (models with $D_f = 1$ being identical to a powerlaw). The lower limit on the SIS bandpass (along with calibration uncertainties) leads to us being insensitive to $N_{H,z} \lesssim 2 \times 10^{20} \text{ cm}^{-2}$, and the upper limit on the *ASCA* bandpass leads to us being insensitive to $N_{H,z} \gtrsim 10^{24} \text{ cm}^{-2}$. Two datasets are consistent with $D_f = 1$ at 68% confidence: Mrk 841(2) & NGC 6814(1). These sources are consistent with a single powerlaw, and thus $N_{H,z}$ is effectively undefined (as illustrated by the errors ‘pegging’ at the limits in Table 4). In addition it should be noted that Fairall 9 is consistent with $D_f = 1$ at 90% confidence and statistically acceptable solutions to the Mrk 509 dataset obtained at 90% confidence at both high and low values of $N_{H,z}$. Thus model *A(ii)* does not provide a unique explanation to the datasets which exhibit a subtle upturn at the highest energies (i.e. those with a high- $N_{H,z}$, high- D_f solution). Indeed, this might be an indication of a real curvature in the underlying continuum (see §6.4), although it might also arise as a result of spectral variability during the observation or (less likely) the result of incomplete background-subtraction. However, it is worth noting that the best-fitting models for 4 datasets (Mrk 335, NGC 3227, Mrk 766 & NGC 4593) are in regions of parameter-space where the *ASCA* data are sensitive to the model. These sources have $10^{21} \lesssim N_{H,z} \lesssim \text{few} \times 10^{22} \text{ cm}^{-2}$ and $0.3 \lesssim D_f \lesssim 0.7$. Nevertheless yet superior fits are obtained with subsequent models in all 4 cases (Mrk 335 – §6.4.2; NGC 3227, Mrk 766 & NGC 4593 – §5.3).

5.3. Model *B(i)*: Complete covering by ionized material

The results of the analysis assuming the powerlaw continuum passes through ionized material, completely covering the source are listed in Table 5. It can be seen that for the majority of the datasets such a model provides a vast improvement over model *A(i)* in which the material responsible for the absorption was assumed to be neutral. Indeed, from

the F -statistic ($F(\frac{Bi}{Ai})$ in Table 5) it can be seen that the addition of U_X as a free parameter leads to an improvement over the results obtained assuming model $A(i)$ (§5.1) significant at $>95\%$ confidence for all but Fairall 9 and NGC 6814(1), and at $>99\%$ confidence for all but Fairall 9, 3C 120, NGC 6814(1) and Mrk 841(2). A direct comparison of χ_{Bi}^2 in Table 5 with χ_{Aii}^2 in Table 4 (both models having the same number of *dof*) indicates model $B(i)$ also offers a superior description of the data than model $A(ii)$ for the majority of the datasets. The notable exceptions to this are the observations of 3C 120, IC 4329A and (especially) all 3 observations of NGC 4151. It should also be noted that $\frac{\Delta\chi_{0.6}^2}{\Delta N_{0.6}}$ and $\overline{R_{0.6}}$ (Table 5) are both greatly improved compared to those derived assuming model $A(ii)$ (Table 4) for a number of datasets, indicating model $B(i)$ provides a far superior description of the data <0.6 keV. This is true even for a number of datasets that do not satisfy our criteria for acceptability, and in most cases the result of a ‘recovery’ of the absorbed spectrum at low energies (below the oxygen K -shell edge) due to carbon and nitrogen being fully ionized and hence the gas pseudo-transparent at these energies.

A total of 14 datasets satisfy all our criteria for acceptability assuming model $B(i)$. These include the 10 datasets for which our criteria were also satisfied by model $A(ii)$, along with NGC 3783(1,2), NGC 5548 and Mrk 841(1). The derived model spectra and data/model ratios for the 8 datasets for which model $B(i)$ is acceptable and offers an improvement at $>99\%$ confidence over both models $A(i)$ and $A(ii)$ are shown in Fig 6. We note that $P_{Bi} = 0.03$ in the case of Mrk 766, indicating this model (and all subsequent models) could be considered an over-parameterization of the data. For 2 of the remaining datasets (NGC 3516 and MCG-6-30-15(1)) we find model $B(i)$ to offer a significant improvement over both models $A(i)$ and $A(ii)$, yet no significant further improvement in the goodness-of-fit obtained assuming subsequent models presented in §5. These two datasets are also shown in Fig 6, despite our formal criteria for acceptability not being satisfied.

The superior description of the data at low energies afforded by model $B(i)$ compared to that of model $A(ii)$ is illustrated by comparison of panels for NGC 3227, Mrk 766, NGC 4593 and Mrk 509 in Figs 4 and 6, and attributable to the reduction in opacity of the ionized gas at low energies. Inspection of the data/model residuals of the remaining datasets reveal that both observations of MCG-6-30-15 fail to satisfy our criteria for acceptability primarily due to a deficit of counts around ~ 1 keV. As noted in Table 12, such a deficit is also evident in the data/model residuals for NCG 3516 (along with an apparent excess scatter across the entire energy range), and in NGC 3783(1,2). The feature may be the result of ‘excess’ absorption by OVIII, and is further discussed in §6.2.

The distribution of the photon index from these fits, shown in Fig 2c, covers a similar range and remains peaked at $\Gamma \sim 2$ as for models $A(i)$ and $A(ii)$. The distribution of the

column density of the ionized material shows no clear preference, with a broad variety of values over the range $10^{21} \lesssim N_{H,z} \lesssim 10^{23} \text{ cm}^{-2}$. The distribution for the ionization parameter (U_X), plotted in Fig 7a, is extended over the range $10^{-2} \lesssim U_X \lesssim 10$, but exhibits a clear peak at $U_X \sim 0.1$. It is worth noting that the datasets with ionization parameters in the range $1 \lesssim U_X \lesssim 10$ lie in regions of $N_{H,z}$ - U_X parameter-space where the ionized gas is largely transparent in the *ASCA* band. Thus the best-fitting spectra for these datasets (e.g. Fairall 9, 3C 120, NGC 7469(2), MCG-2-58-22) are essentially powerlaws, consistent with the findings above. In Fig 8a we plot the derived values for $N_{H,z}$ and U_X for the 11 datasets for which model $B(i)$ offers an adequate description of the data *and* leads to an improvement at $> 99\%$ over model $A(i)$. The corresponding values for NGC 3516 and both datasets of MCG-6-30-15 are also shown in Fig 8a for comparison.

Finally we note that all the datasets for which model $B(i)$ provides an acceptable solution have best-fitting $N_{H,0}$ consistent with that derived from 21 cm measurements (Table 3) with the exception of 3783(1) ($\Delta N_{H,0} \simeq 2 \times 10^{20} \text{ cm}^{-2}$) along with 3C 120 and NGC 7469(2), both of which have excess column densities similar to those found in §5.2.

5.4. Model $B(ii)$: Partial-covering by an ionized absorber

The results of the analysis assuming model $B(ii)$ are listed in Table 6. The relationship of this model to model $B(i)$ is the same as the relationship between models $A(i)$ and $A(ii)$: identical except that now a fraction D_f of the observed continuum is a bare powerlaw whilst a fraction $(1 - D_f)$ is attenuated by line-of-sight material at the redshift of the source. (see §4). It can be seen that model $B(ii)$ provides a further substantial reduction in the χ^2 -statistic for many of the datasets. From the F -statistic ($F(\frac{Bii}{Aii})$ in Table 6) we find that the addition of U_x as a free parameter leads to a improvement over the results obtained assuming model $A(ii)$ for 17 (16) datasets at $>95\%$ ($>99\%$) confidence¹¹.

A total of 15 datasets satisfy all our criteria for acceptability assuming model $B(ii)$. These include 13 out of the 14 datasets for which model $B(i)$ was found formally acceptable¹², along with NGC 4151(2,4). As was the case for model $B(i)$, inspection of the data/model residuals reveals that a deficit of counts at $\sim 1\text{keV}$ is the primary reason why several of the remaining datasets fail to satisfy our criteria for acceptability (namely NGC 3516, NGC 4151(5) and MCG-6-30-15(1,2)).

¹¹See the note to Table 6 for an explanation of the apparent increase in χ^2 for the observations of Fairall 9, 3C 120 & IC 4392A.

¹²The exception being Mrk 841(1), which falls outside our formal limit of $P_{Bii} \leq 0.95$ by just $\Delta P_{Bii} = 0.001$

Interestingly, we find that the inclusion of the additional free parameter D_f compared to model $B(i)$ improves the fit at $>99\%$ confidence for 10 of the 23 datasets (as shown by the values of the F -statistic $F(\frac{B(ii)}{B(i)})$ listed in Table 6). Furthermore, 8 of these datasets satisfy our criteria for acceptability, indicating the spectrum observed from a significant fraction of the datasets may indeed contain a component of the underlying continuum which does not experience attenuation by the ionized gas. The best-fitting solutions for all 5 datasets for which model $B(ii)$ is acceptable and offers an improvement at $>99\%$ confidence over both models $A(ii)$ and $B(i)$ have $D_f > 0$, as illustrated by the derived model spectra and data/model ratios shown in Fig 9. For one of the remaining datasets (NGC 4151(5)) we find model $B(ii)$ to offer a significant improvement over previous models, yet no significant further improvement in the goodness-of-fit obtained assuming subsequent models presented in §5. This dataset is also shown in Fig 6, despite our formal criteria for acceptability not being satisfied.

In Fig 8b we plot the derived values for $N_{H,z}$ and U_X for the 10 datasets for which model $B(ii)$ offers an adequate description of the data *and* leads to an improvement at $> 99\%$ over model $A(ii)$. The corresponding values for NGC 3516, NGC 4151(5), MCG-6-30-15(1,2) and Mrk 841(1) are also shown in Fig 8b for comparison.

Again the limitations imposed on parameter-space by the *ASCA* bandpass and the signal-to-noise ratios are reflected in a number of the fits. Obviously, the comments made in §5.2 regarding solutions with $D_f \simeq 1$, and in §5.3 regarding the transparency of the ionized gas in the low- $N_{H,z}$, high- U_X region of parameter space are also applicable to model $B(ii)$. These effects prevent useful constraints being placed on $N_{H,z}$ in a number of cases. Furthermore, the gas for models in the high- $N_{H,z}$, low- U_X region of parameter space is close to neutral, giving rise to spectra identical to those in model $A(ii)$. As for model $A(ii)$, the best-fitting models for a number of datasets exhibit a subtle upturn at the highest energies.

As might be expected, the distribution of the photon index (Fig 2d) covers a similar (but slightly broader) range as that derived from previous models, and is still peaked at $\Gamma \sim 2$. As for model $B(i)$, there appears to be no preferred value of the intrinsic column density (Fig 3d), with the derived values (if errors are also considered) covering over three decades in $N_{H,z}$. The datasets for which $D_f > 0$ are gathered in the range $0.3 \lesssim D_f \lesssim 1.0$, with the exception of the 3 observations of NGC 4151 which have $0.03 \lesssim D_f \lesssim 0.1$ (Fig 5b). The distribution in ionization parameter is extended over the range $10^{-2} \lesssim U_X \lesssim 1.0$, but as for model $B(i)$, there is a clear concentration around $U_X \sim 0.1$ (Fig 7b).

Finally, we note that the best-fitting solutions to 13 of the 15 datasets considered acceptable have Galactic column densities ($N_{H,0}$) consistent with that derived from 21 cm measurements (Table 3). Again the exceptions are 3C 120 and NGC 7469(2), both of which

have excess column densities similar to those found in §5.2.

5.5. Model $C(i)$: Complete covering by an ionized absorber plus an ionized emitter

The results of assuming model $C(i)$ are listed in Table 7. This model assumes the powerlaw continuum passes through ionized material, completely covering the source (i.e. as for model $B(i)$), but in addition contains the emission and scattered spectrum expected from the ionized gas assuming it subtends a solid angle Ω at the central source (see §4). We see that the such a model provides further improvement for many of the datasets. Using the F -statistic ($F(\frac{C_i}{B_i})$ in Table 7) it can be seen that the addition of Ω as a free parameter leads to an improvement over the results obtained assuming model $B(i)$ for 15 (11) datasets at $>95\%$ ($>99\%$) confidence. A direct comparison of $\chi^2_{C_i}$ in Table 7 with $\chi^2_{B_{ii}}$ in Table 6 (both models having the same number of dof) indicates model $C(i)$ also offers a significant improvement over the results obtained assuming model $B(ii)$ for NGC 3783(1,2), NGC 4051 and MCG-6-30-15(2). We note, however, that model $C(i)$ provides an inferior fits compared to model $B(ii)$ for the observation of 3C 120 and all 3 observations of NGC 4151. This indicates that consideration of the covering fraction of the ionized absorber is more important than its emission in these cases. Model $C(i)$ offers only a modest improvement or slightly inferior fit to the remaining datasets.

A total of 15 datasets satisfy all our criteria for acceptability assuming model $C(i)$. As summarized in Table 12, this includes all 14 datasets for which our criteria for acceptability were also satisfied by model $B(i)$, along with MCG-6-30-15(2). As was the case for models $B(i)$ & $B(ii)$, inspection of the data/model residuals reveals that a deficit of counts at $\sim 1\text{keV}$ is the primary reason why the datasets of NGC 3516, MCG-6-30-15(1) fail to satisfy our criteria for acceptability. The spectrum emitted by the ionized gas includes Fe lines in the 6.4–7.1 keV band (rest-frame). Since the bulk of this region is excluded from our spectral analysis, it is possible that the best-fitting model will be inconsistent with the observations within this band. However for all 15 datasets which satisfying our criteria for acceptability, we find the best-fitting solutions lie in a region of $N_{H,z}$ – U_X – Ω parameter-space such that the predicted line-strength is less than that observed. The derived model spectra and data/model ratios for the 4 datasets for which model $C(i)$ is acceptable and offers an improvement at $>99\%$ confidence over both models $B(i)$ and $B(ii)$ are shown in Fig 10.

In Fig 8c we plot the derived values for $N_{H,z}$ and U_X for the 13 datasets for which model $C(i)$ offers an adequate description of the data *and* leads to an improvement at $> 99\%$ over model $A(i)$. The corresponding values for NGC 3516 and MCG-6-30-15(1) are

also shown in Fig 8c for comparison.

The inclusion of the emission spectrum does not globally change the distributions of the Γ , $N_{H,z}$ and U_X for these datasets as shown Figs 2e, 3e, and 7c (respectively). In general the parameters cover similar ranges as for models $B(i)$ & $B(ii)$, with the datasets exhibiting a range of photon indices (but peaked at $\Gamma \sim 2$), column densities and ionization parameter (again peaking at $U_X \sim 0.1$). As can be seen from Fig 11a, the solid angle of the ionized emitter is poorly constrained in most cases, but there is a clear peak at $\Omega \sim 4\pi$ (i.e. consistent with emission from a complete shell).

Again, the best-fitting solutions to all the datasets considered acceptable have Galactic column densities ($N_{H,0}$) consistent with that derived from 21 cm measurements (Table 3), with the exceptions of 3C 120 and NGC 7469(2), both of which have excess column densities similar to those found in §5.2.

5.6. Model $C(ii)$: Partial-covering by an ionized absorber plus an ionized emitter

The results of the analysis assuming model $C(ii)$ are listed in Table 8. As described in §4, this model is the same as model $C(i)$ except that only a fraction $(1 - D_f)$ of the observed continuum is attenuated by the ionized gas. (The spectral component due to the emission and scattered spectrum expected from the ionized gas is unaffected and parameterized by Ω , just as in model $C(i)$.) It can be seen that model $C(ii)$ provides a significant reduction in the χ^2 -statistic for several datasets. From the F -statistic ($F(\frac{Cii}{Bii})$ in Table 6) we find that the addition of Ω as a free parameter leads to an improvement over the results obtained assuming model $B(ii)$ for 14 (8) datasets at $>95\%$ ($>99\%$) confidence. Alternatively, we find that the addition of D_f as a free parameter leads to model $C(ii)$ being preferred over model $C(i)$ for 9 (8) datasets at $>95\%$ ($>99\%$) confidence. However, we note that model $C(ii)$ offers an improvement at $>99\%$ confidence over both models $B(ii)$ and $C(i)$ for only 4 datasets (NGC 4051, NGC 4151(4), NGC 5548 and Mrk 509). The derived model spectra and data/model ratios of these are shown Fig 12. It should be noted, however, that in the case of NGC 4051, the best-fitting solution assuming model $C(ii)$ fails to meet our formal criteria for acceptability. This is mostly likely due to (at least in part) spectral variability within the observation giving rise to spectral curvature (see §6.4). In addition, the best-fitting solution to NGC 5548 over-predicts the number of counts < 0.6 keV ($\overline{R}_{0.6} \sim 1.3$). Finally it should be noted that the best-fitting solutions for NGC 5548 and Mrk 509 lie in the high- $N_{H,z}$, high- U_X , high- D_f region of parameter space. The resultant spectra are therefore essentially powerlaws with subtle upturns at both the

very lowest and very highest energies (Fig 12). The meaningfulness of such solutions is therefore questionable, as it may simply be indicative of spectral curvature (see §6.4).

A total of 16 datasets satisfy all our criteria for acceptability assuming model $C(ii)$. These include 14 out of the 15 datasets for which model $C(i)$ was found formally acceptable (the exception being NGC 5548, which just fails our criteria for extrapolation <0.6 keV as noted above), along with 2 of the 3 observations of NGC 4151. As was the case for previous models, inspection of the data/model residuals reveals that a deficit of counts at ~ 1 keV is the primary reason why the datasets from NGC 3516, NGC 4151(5) and MCG-6-30-15(1) fail to satisfy our criteria for acceptability. We also note that for 5 of the 16 datasets satisfying our criteria for acceptability for this model (Mrk 335, 3C 120, NGC 5548, NGC 7469(2) and MCG-2-58-22), the best-fitting solutions over-predict the strength of the Fe K -shell lines in the 6.4–7.1 keV band. In a number of cases the 90% confidence region in $N_{H,z}$ – U_X – Ω parameter-space does include solutions consistent with observed line strengths. However, as will be shown in §6.4, in all cases the solution obtained assuming model $C(ii)$ is most likely an artifact of spectral curvature in the underlying continuum.

In Fig 8d we plot the derived values for $N_{H,z}$ and U_X for the 11 datasets for which model $C(ii)$ offers an adequate description of the data *and* leads to an improvement at $> 99\%$ over model $A(ii)$. The corresponding values for NGC 3516, NGC 4151(5), MCG-6-30-15(1) and NGC 5548 are also shown in Fig 8e for comparison.

As for model $C(i)$, we find the inclusion of the emission spectrum does not globally change the distributions of the Γ , $N_{H,z}$, D_f and U_X for these datasets as shown in Figs 2d, 3d, 5c and 7b (respectively). In general the parameters cover similar ranges as for previous models. In most cases, the emission from the ionized gas forms a significant fraction of the observed spectrum only at low energies, and is dominated by emission lines due to K -shell processes of C, N & O. However, it should be noted that in a number of cases (e.g. NGC 4151(4) & Mrk 509) the Fe K -shell emission line and scattered continuum do contribute to the spectrum observed above ~ 3 keV.

Again we find the best-fitting solutions to all the datasets considered acceptable have Galactic column densities ($N_{H,0}$) consistent with that derived from 21 cm measurements (Table 3), with the exceptions of Mrk 509 (with $\Delta N_{H,0} \simeq 5 \times 10^{20} \text{ cm}^{-2}$), and 3C 120, NGC 3783(1) and NGC 7469(2), all of which have excess column densities similar to those found previously.

Finally, in Fig. 13 we show the mean data/model ratios (in the *observer's* frame) in the SIS and GIS for the 16 datasets satisfying our criteria for acceptability assuming model $C(ii)$. This plot was constructed by taking the error-weighted average of the individual

data/model ratios for each detector from each of the appropriate observations. These averages were then rebinned for display purposes. Caution is urged when interpreting such plots. They potentially contain artificial features introduced by time-dependent errors in the calibration of the instruments (such as slight offsets in the gain of the detectors at the time of each observation), along with real features due to errors in the calibration of the instrument, as well as real features of astrophysical origin. Furthermore such plots are dominated by the datasets with the highest signal-to-noise ratio. Nevertheless, we have found Fig. 13 helpful in judging the reality of features/noise in individual datasets.

6. ADDITIONAL MODELS

In the previous section we made the premise that the ‘primary’ X-ray continuum was a powerlaw. We then compared the observed spectrum with that expected assuming a number of (probably simplistic) assumptions regarding the geometry and physical conditions within the circumnuclear material. We found that one or more of this family of models to be consistent with 17 of the 23 datasets considered within our formal criteria of acceptability (§4.1). Of the 6 remaining datasets, the primary reason why the criteria of acceptability are not achieved is due to excess scatter in the residuals within the 2–4 keV band for Fairall 9 (see Fig. 4, the observed spectrum otherwise being consistent with model $A(ii)$), a deficit of counts at ~ 1 keV in the case of NGC 3516, NGC 4151(5) and MCG-6-30-15(1) (see Figs 6 & 9), and a more complex spectral form in the case of NGC 4051 and IC 4329A (Figs 12 & 4 respectively). In this section we extend our spectral analysis to address a number of issues raised in the previous section.

6.1. The redshift of the ionized gas

In §5 it was assumed that the ionized gas along the line-of-sight was situated close to (and not in motion relative to) the active nucleus (i.e. at the redshift of the host galaxy, z_{gal}). The sharp features imprinted by the ionized material (primarily OVII and/or OVIII absorption edges for most datasets, with rest-frame energies of 740 and 871 eV) facilitate testing such an hypothesis. The spectral resolution of the SIS is a complex function of energy, time and various other instrument effects. However at the epoch of the observations, $\Delta E/E \simeq 0.07$ – 0.09 in the 0.6–1.0 keV band (e.g. Dotani et al 1996). Useful constraints on the redshift of the ionized gas z_{ion} are only likely to be obtained for those datasets with the strongest absorption and/or emission features. Nevertheless, we have repeated the spectral analysis for models $B(i)$ – $C(ii)$ allowing the redshift of the ionized gas (z_{ion}) to be a free

parameter. However, in the vast majority of cases we found the 90% confidence range for z_{ion} to encompass both $z_{ion} = 0$ and $z_{ion} = z_{gal}$. We find the most stringent constraints on z_{ion} to be provided by model $C(i)$ applied to 3783(1), where $z_{ion} = z_{gal} - 0.002_{-0.012}^{+0.015}$ (where $z_{gal} = 0.009$). The formal limits exclude $z_{ion} = 0$ and/or $z_{ion} = z_{gal}$ for a few dataset/model combinations, but further investigation reveals that in each case the result is due to fitting small statistic fluctuations in the data. Given the recent detection of ionized gas at the redshift of the host galaxy in another AGN (the high-redshift quasar PG 1114+445; George et al. 1997a) and lack of evidence to the contrary here, we conclude our assumption to be valid.

6.2. Evidence for a second, ionized absorber

During the analysis presented in §5, a number of datasets were observed to consistently exhibit a deficit in their data/model ratio at ~ 1 keV. This feature was most evident in both datasets of NGC 3783 (e.g. Figs 6, 9 & 10) and MCG-6-30-15 (Figs 9 & 10), and in the single dataset from NGC 3516 (Fig 6). As noted in the introduction, the ~ 1 keV deficit has also been seen by a number of other workers, and since it appears close to the K -shell edges of O and Ne, it has been suggested that it is the result of absorption by a second cloud/screen of ionized gas along the line-of-sight (e.g. Kriss et al. 1996a; Otani et al. 1996).

As will be discussed in §8.8 there are a number of explanations for such a feature, and a detailed investigation of these are beyond the scope of the current paper. However, in Table 9 we list the results obtained when an absorption edge of optical depth τ_{ONe} is added to model $B(i)$. The (rest-frame) energy of the edge, E_{ONe} , was allowed to vary over the range 0.568–1.362 keV, thus covering the edges due to OVI–Nex. As can be seen from the values of the F -statistic $F_{ONe/Bi}$, the addition of this component improved the goodness-of-fit at $> 99\%$ confidence for all 5 datasets. A comparison with Table 5 shows that the effect of including such an additional edge is to reduce the best-fitting values of U_X and $N_{H,z}$. Furthermore, in all but one case (NGC 3783(1)) we find the best-fitting energy for the edge to be consistent with that due to OVIII. We also tested the addition of such an edge to model $C(i)$ and obtained similar results, except that the edge in NGC 3783(1) is now also consistent with that due to OVIII.

Finally, it should be stressed that such a deficit is *not* seen in several of the other datasets presented here, and hence unlikely to be the result of a calibration error. For example, in the case of the high signal-to-noise, powerlaw dataset 3C 120, we find the additional of an OVIII edge to model $B(i)$ makes an insignificant improvement in the

goodness-of-fit ($\Delta\chi^2 < 1$), with $\tau_{ONe} \lesssim 0.02$ at 90% confidence (for one interesting parameter).

We consider these results to be indicative of a second absorbing system in some objects. This possibility, along with the fact that the 1 keV deficit is present in the datasets with the strongest absorption features, is discussed in §8.8.

6.3. Implications for Fe K -shell band

6.3.1. Fe K -shell emission

In Paper II we presented an analysis of the spectra of all 23 datasets in the 3–10 keV band. The approach used was to approximate the underlying continuum with a powerlaw in order to perform a detailed investigation the profile of the Fe $K\alpha$ line. In the present work, we have ignored the 5–7 keV band, which contains the bulk of the Fe $K\alpha$ line emission. Clearly it is inappropriate to repeat here the full analysis presented in Paper II. However there are two consistency checks which should be performed.

First, in §5 we have shown that the 0.6–10 keV continuum in these sources can be well represented by a powerlaw imprinted with (primarily absorption) features due to ionized gas along the line-of-sight. Comparison of Tables 3–6 with the corresponding results from Paper II reveal consistent values of Γ . Thus the approximation of the local continuum used in Paper II is indeed valid, and hence the intensity and profile of the line emission presented in Paper II is also valid. This is illustrated in Fig 14 in which we show the mean profiles obtained for models $B(ii)$, $C(i)$ and $C(ii)$ compared to that presented in Paper II.

Second, models $C(i)$ and $C(ii)$ contain the emission spectrum for the ionized gas, which includes significant Fe K -shell features in certain regions of $N_{H,z}$ – U_X parameter-space. We have therefore repeated the analysis for these models, but including the 5–7 keV band and an emission line as an additional spectral component. The profile of the emission line assumed is that expected from the innermost regions of an accretion disk under the influence of the strong gravitation effects of the central black hole. For convenience, we have followed Paper II and adopted the parameterization of Fabian et al (1989), fixing the inner and outer radii of the disk at $R_i = 6R_g$ and $R_o = 10^3R_g$ (respectively, where R_g is the gravitational radius), the axis of rotation with respect to the line-of-sight of $i = 30^\circ$, and the (rest-frame) energy of the line to be $E_{K\alpha} = 6.4$ keV. The emissivity of the line is parameterized as a powerlaw as a function of radius ($\propto R^{-2.5}$), leaving only the equivalent width of the line, $W_{K\alpha}$, as a free parameter. As may be expected from Fig 14, for both models $C(i)$ and $C(ii)$, we find results consistent with those presented in Paper II, with mean equivalent widths of

the diskline $\overline{W}_{K\alpha} \simeq 290 \pm 30$ eV, compared with $\overline{W}_{K\alpha} \simeq 270 \pm 14$ eV derived from Table 5 of Paper II.

6.3.2. Fe K-shell absorption

Ginga observations indicated a large fraction ($\gtrsim 40\%$) of type-1 AGN might possess a significant Fe absorption edge in the 7.1–8.9 keV band (Nandra & Pounds 1994). However given the spectral resolution of the LAC and the presence of the strong Fe *K*-shell emission in the 6–7 keV band, the parameters of such a feature could not be unambiguously determined by *Ginga*. Nevertheless, Nandra & Pounds did find a preferred energy of ~ 7.9 keV (equivalent to FeXVIII) and effective hydrogen column densities $N_{H,z} \sim \text{few} \times 10^{23} \text{ cm}^{-2}$.

Unfortunately the end of the effective bandpass of the SIS and GIS at ~ 10 keV and the low signal-to-noise ratio of most datasets in the 7–10 keV band makes the study of such a feature extremely difficult with *ASCA*. We have not attempted such a study here, especially since we employed an analysis technique whereby we explicitly excluded the Fe *K*-shell emission (in the 5–7 keV band) from the majority of the fits. However as can be seen in Figs 6, 9, 10 & 12, our models for the photoionized gas do *not* predict significant Fe *K*-shell absorption edges for the values of U_X and $N_{H,z}$ typically derived in §5 (the *ASCA* results being primarily based on O *K*-shell, Ne *K*-shell and Fe *L*-shell absorption features). If confirmed, the absorption features seen by *Ginga* imply an additional, large column density of highly-ionized gas along the cylinder-of-sight, possibly related to that suggested as responsible for the ‘ ~ 1 keV deficit’ described in §6.2. However we note that there is no obvious evidence for such features in Fig 14.

6.4. Constraints on a more complex continuum form

Given the diversity in the observed spectra presented here, the assumption that the continuum is well represented by a single powerlaw over the entire 0.4–10 keV band can be questioned. Indeed, based on both observational and theoretical arguments, in the past a number of more complex spectral forms have been suggested for the underlying X-ray continuum in Seyfert 1 galaxies. These can be divided into those in which the underlying emission mechanism gives rise to a continuum with a more complex form (a simple case case a continuum represented by the sum of two powerlaws), and those in which a ‘primary’ powerlaw continuum is augmented by other sources of emission (both thermal

and non-thermal, inside and outside the active nucleus).

In §5 we found a number of datasets consistently satisfied by best-fitting parameters which could imply a gradual flattening of the observed spectrum to higher energies (e.g. Mrk 335, NGC 4051, IC 4329A). The data/model residuals of a number of other datasets also imply a ‘soft excess’ of counts at the lowest energies and/or a ‘hard tail’ at the highest energies (e.g. NGC 3516, 3C 120). In the light of this, we have investigated two forms of the continuum commonly assumed for Seyfert 1 galaxies: the addition of a ‘Compton Reflection’ component, and an underlying continuum represented by the sum of two powerlaws. We have also investigated the inclusion of a thermal emission component at the softest energies.

It should be remembered, however, that spectral curvature can of course also arise as the result of spectral variability within an observation. Throughout this paper we consider only the mean spectra. However in Paper I we presented evidence for variability in many of the datasets. In most datasets any *spectral* variability was of relatively low amplitude, but a number of cases (primarily the low luminosity sources, and especially NGC 4051), the amplitude could be at a level to start affecting our analysis of the mean spectra.

6.4.1. *The effects of including ‘Compton Reflection’*

‘Compton-reflection’ of the ‘primary’ continuum by optically-thick, neutral material out of the line-of-sight is often invoked as an explanation of the high equivalent width of the Fe $K\alpha$ line emission and flattening of the spectrum $\gtrsim 10$ keV in many AGN (e.g. Nandra & Pounds 1994). The presence of an unresolved reflection component can flatten the observed continuum, so the underlying continuum could be slightly steeper than observed, which could have implications on the best-fitting values of the parameters associated with the ionized gas. We have therefore repeated the analysis for model $C(ii)$ including the effects of the ‘Compton-reflection, which we parameterize by the addition of the enhancement factor, \mathcal{F} , of the reflected continuum (only) compared to that expected from a semi-infinite plane illuminated by a point source viewed face-on.

We find fixing $\mathcal{F} = 1$ does not improve the goodness-of-fit at $\geq 99\%$ confidence for any of the datasets. As expected, in most cases the derived spectral index is slightly steepened by $\Delta\Gamma \lesssim 0.15$, and in all cases best-fitting values of $N_{H,z}$ and U_X are consistent with those quoted in Table 8.

Interestingly, allowing \mathcal{F} to be a free parameter in the analysis, we do find a significant improvement in the goodness-of-fit for 9 datasets (Mrk 335, NGC 3783(2), NGC 4051, NGC 4593, MCG-6-30-15(1,2), IC 4329A, NGC 5548, Mrk 509), with $\mathcal{F} \sim 3$ –5. Such

values have been suggested for some of these objects by previous studies using different instrumentation (e.g. Nandra & Pounds 1994; Molendi et al, 1997). However, since the *ASCA* bandpass effectively ends at 10 keV, such a component is difficult to constrain and weaker Compton-reflection components would be undetectable. For $\mathcal{F} \lesssim 10$, the predicted equivalent width of the Fe $K\alpha$ from the reflecting material can be approximated by $W_{K\alpha} \sim 150\mathcal{F}(\frac{A_{\text{Fe}}}{3.3 \times 10^{-5}})$ eV, where A_{Fe} is the abundance of Fe relative to hydrogen (e.g. George & Fabian 1991). The most recent estimations of the Fe abundance are $A_{\text{Fe}} \sim 4.7 \times 10^{-5}$ (Anders & Grevesse 1989) and $\sim 3.2 \times 10^{-5}$ (Feldman 1992), and from observations we find $\overline{W_{K\alpha}} \simeq 290 \pm 30$ eV (§6.3.1) for these 9 datasets. Thus these best-fitting solutions imply a moderate under-abundance of Fe in these Seyferts compared to solar values. We do not consider this unreasonable *per se*, but note these solutions may also be indicative of curvature in the underlying continuum shape, rather than the presence of a strong reflection component. Indeed alternative explanations are available in the case of Mrk 335, NGC 4051, IC 4329A (see §6.4.2). In any event, we find the inclusion of the reflection component typically only steepens the underlying spectral index by $\Delta\Gamma \lesssim 0.2$ in these 9 datasets, and in all cases again find the best-fitting values of $N_{H,z}$ and U_X are within the error ranges quoted in Table 8.

6.4.2. Double powerlaw continua

The form of the continuum considered in this section is represented by the sum of two powerlaws¹³, with photon indices Γ_s and Γ_h (where $\Gamma_s > \Gamma_h$). The ratio of the normalization of the soft powerlaw divided by that of the hard powerlaw at 1 keV (in the rest-frame of the source) is denoted by $R_{s/h}$. For computational expediency we restrict parameter space such that $1.5 \geq \Gamma_s \geq 5.0$ and $0.0 \geq \Gamma_h \geq 2.5$. Such a model has been applied to all the datasets considered here. Here we concentrate on the results when this additional powerlaw component is added to model $C(i)$ as they are representative of the rest. Clearly such a model has the same number of interesting parameters as the model discussed in §6.4.1.

We find this model leads to an improvement over the results obtained assuming model $C(ii)$ for 10 of the 23 datasets at >99% confidence. The best-fitting solutions for 4 of these datasets have $R_{s/h} \sim 1$ with both powerlaws of similar importance over a sizable fraction of the *ASCA* bandpass. In the case of the remaining 6 datasets, the bulk of the *ASCA*

¹³i.e. not the somewhat artificial 'broken-powerlaw' model (which has also been applied in the past to AGN spectra by some workers) in which the continuum is assumed to be a steep powerlaw below some energy at which it sharply breaks to a flatter powerlaw

bandpass is dominated by a single powerlaw, with the second powerlaw component making a significant contribution only at either the very lowest energies (the ‘ultra-soft excess’ datasets) or highest energies (the ‘hard tail’ datasets).

We consider first the 3 datasets (3C 120, NGC 4593, Mrk 509) for which this model implies a ‘hard tail’. Naturally we find the powerlaw which dominates the observed spectrum at the highest energies to be relatively weak ($R_{s/h} \gg 1$) and flat (although its photon index is poorly constrained within the range $0.2 \lesssim \Gamma_h \lesssim 1.8$). In each case the steeper powerlaw, dominating the observed spectrum over most of the *ASCA* bandpass, has a photon index steeper by $\Delta\Gamma \sim 0.2$ than that found assuming model *C(ii)* (in fact all 3 datasets have $\Gamma_s \simeq 2.2$). However, it should be noted that the underlying continua derived for these 3 datasets assuming this model exhibit only a relatively subtle curvature across the *ASCA* bandpass. It is therefore not that surprising that in all cases the best-fitting values of the parameters associated with the ionized gas (U_X and $N_{H,z}$) are similar to those found when the underlying continuum is approximated by a single powerlaw.

Turning now to the 3 datasets for which this model implies an ‘ultra-soft excess’ (NGC 3516, MCG-6-30-15 (1,2)), in all cases we find the powerlaw which dominates the observed spectrum over most of the *ASCA* bandpass has a photon index flatter by $\Delta\Gamma \sim 0.1$ than that found for model *C(ii)*. The best-fitting solutions imply a very steep second powerlaw component (pegging at our upper limit of $\Gamma_s = 5$ for all 3 datasets) dominating the observed spectrum only at the very lowest energies (with $R_{s/h} \sim 0.3$ – 0.5). However, none of the best-fitting models extrapolate <0.6 keV in a satisfactory manner (even given best-fitting values of $N_{H,0}$ significantly in excess of $N_{H,0}^{gal}$), and all imply an α_{ox} far steeper than that observed. Further investigation of such a component is extremely difficult with *ASCA* data. However, again, the best-fitting values of the parameters associated with the ionized gas (U_X and $N_{H,z}$) are similar to those found when the underlying continuum is approximated by a single powerlaw.

Finally, we consider the remaining 4 datasets for which this analysis indicates both powerlaws are of similar importance over a sizeable fraction of the *ASCA* bandpass (Mrk 335, NGC 4051, IC 4329A, NGC 5548). The best-fitting parameters of for these datasets are listed in Table 11, and the derived model spectra and data/model ratios shown in Fig 15. As further discussed in the Appendix, the form of the continuum implied for Mrk 335 is in good agreement with previous observations. However any imprints due to ionized gas are weak in Mrk 335, allowing no useful constraints to be placed on $N_{H,z}$, U_X or Ω . The best-fitting solution for the other 3 datasets are somewhat similar, with a relatively steep ($\Gamma_s \gtrsim 3$) powerlaw dominating the spectrum $\lesssim 1$ keV along with evidence for absorption and emission from ionized gas. However, in all 3 cases the reality of such a

continuum can be questioned. Significant spectral and flux variability occur on timescales much shorter than the observation period in the case of NGC 4051 (Paper I). Thus we consider short-timescale spectral variability may be partly responsible for the apparent curvature of the underlying continuum in NGC 4051. As is apparent from Table 11, this model fails to satisfy our criteria for acceptability in the case of IC 4329A. As further discussed in the Appendix, this source appears to have a particularly complex spectral form, and hence it is difficult to judge the robustness of the values derived for $N_{H,z}$, U_X or Ω . In the case of NGC 5548, an acceptable fit is achieved assuming this model. However it should be noted that the steep ($\Gamma_s \sim 3.2$), soft component derived does appear to be a relatively poor representation of the data < 0.6 keV, implying a neutral column density far in excess of $\geq N_{H,0}^{gal}$ ($\Delta N_{H,0} \sim 1.5 \times 10^{21}$ cm $^{-2}$) and giving $\frac{\Delta \chi_{0.6}^2}{\Delta N_{0.6}} \sim 14$ (though $\overline{R_{0.6}} \sim 1$). Finally, as shown in §6.4.1, a single powerlaw with a strong Compton-reflection component can provide a comparable fit for all 3 datasets.

6.4.3. *The effects of including a low-temperature, thermal component*

It has long been suggested that Seyfert galaxies are likely to contain several sites which give rise to thermal emission at temperatures consistent with soft X-rays. These sites occur on different size-scales and arise as a result of processes both directly related to and independent of the AGN phenomenon. Examples include regions of active star formation, the hot-phase of the narrow emission-line region (NELR), the halo of the galaxy and the shock- or X-ray heated ambient interstellar medium (ISM). Thermal emission closely associated with the active nucleus is also expected as a result of the accretion process itself and as a result of the absorption (followed by thermalization) of the continuum. The relative importance of such components probably differs from object to object. In the case of NGC 4151, *Einstein* HRI and *ROSAT* HRI observations have revealed spatially resolved soft X-ray emission (Elvis, Briel & Henry 1983; Morse et al 1995). *ASCA* observations of normal galaxies have also revealed soft X-ray emission with temperatures in the range $kT \sim 0.3$ – 0.6 keV, and luminosities $L_{kT} \sim 10^{38}$ – 10^{40} erg s $^{-1}$ (e.g. Makishima 1994; Serlemitsos, Ptak & Yaqoob 1996). Thus one could question whether the existence of such a component might effect our conclusions regarding the photoionized gas – particularly since the thermal emission offers an alternative to the decreased opacity and emission features at the lowest energies implied in previous models.

We have investigated this by including a component due to an optically-thin plasma (with cosmic abundances, parameterized by a temperature kT and unabsorbed luminosity L_{kT} in the 0.1–3.0 keV band) to model $C(ii)$ (but located *outside* the photoionized

absorber). We find that the goodness-of-fit is indeed improved ($\Delta\chi^2 \sim 9$) in the case of all 3 datasets of NGC 4151, with $kT \sim 0.66$ keV and $L_{kT} \sim 2_{-2}^{+3} \times 10^{41}$ erg s $^{-1}$, consistent with the luminosity of the extended gas measured by the *ROSAT* HRI observation (see §7.2 and Appendix). However, it should be noted that in the *ASCA* bandpass, the dominant features from such gas are Fe *L*-shell lines in the 0.7–1.5 keV regime. Thus whilst L_{kT} is a function of A_{Fe} , the addition of this optically-thin component does not significantly affect the derived values for all other of the parameters (although the size of the allowed parameter space is obviously increased – e.g. see Fig 16).

We find no other dataset is significantly improved by the inclusion of emission from thermal gas at such a temperature. This is hardly surprising since only NGC 4151 occupied a region of the $N_{H,z}$ – U_X plane in which emission of similar strength would not be swamped by the underlying continuum. Thus we consider the the omission of such a component is generally not important in our results.

6.4.4. Summary

In summary, we find evidence for significant curvature in the *observed* continuum in approximately half of the datasets considered. We have shown that for the majority of the datasets, such curvature can be accounted for by the inclusion of a Compton-Reflection and/or a second powerlaw component. However, in the majority of cases, the ionizing continuum can be well represented by a single powerlaw (with $\Gamma \sim 2$) close to the OVII and OVIII absorption edges. These edges provide the main diagnostics for our photoionization models. Thus we consider that the best-fitting parameters associated with the ionized gas derived in models *B* and *C* are generally reliable. Allowing the presence of a low-temperature, thermal component improved the fit only in the case of NGC 4151. However, again we found it to have no significant effect on the best-fitting parameters associated with the ionized gas.

7. OBJECTS WITH MULTIPLE OBSERVATIONS

Our sample contains more than one observation of NGC 3783, NGC 4151, MCG-6-30-15 and Mrk 841. We have found evidence for absorption by ionized material in all four sources, enabling us to compare and contrast the behaviour of the ionized gas.

7.1. NGC 3783

Two datasets of NGC 3783, separated by 4 days, are contained within our sample from observations carried out in 1993 December. As shown in §5.3–5.6, there is clear evidence for ionized gas in this source, with models $B(i)$ – $C(ii)$ providing acceptable fits to both datasets. The observed count rate was $\sim 25\%$ higher for the second observation (e.g. Table 2), which is reflected in an increase in the derived luminosity of the ionizing continuum (for model $C(i)$, after correcting for absorption) from $L_X \simeq 4.6 \times 10^{43}$ erg s $^{-1}$ to $\simeq 5.5 \times 10^{43}$ erg s $^{-1}$. Both observations are consistent with $\Gamma \sim 1.8$, $D_f = 0$, $U_X \sim 0.1$ – 0.15 and $N_{H,z} \sim 2 \times 10^{22}$ cm $^{-2}$ (Table 8). However, as shown in Fig 16, the two datasets actually occupy slightly different regions of the $N_{H,z}$ – U_X plane, consistent with an increase in U_X by $\lesssim 40\%$ and/or a decrease in $N_{H,z}$ (by $\lesssim 5 \times 10^{21}$ cm $^{-2}$) between the 2 epochs. The former offers the simplest interpretation of these data: a screen of ionized gas completely covers the cylinder-of-sight in NGC 3783, becoming more highly ionized as the photoionizing flux increases. Both observations are consistent with the presence of emission from the ionized material, with $L_e \sim 2$ – 6×10^{42} erg s $^{-1}$ in the 0.1–10 keV band (after correcting for absorption). Unfortunately however, the signal-to-noise ratio of these datasets is too low to unambiguously determine whether the intensity of this emission responded to the increase in the ionizing continuum.

Interestingly, a ‘1 keV deficit’ was also evident for both datasets in the data/model residuals of all the models considered in §5. This can be modeled by an additional absorption edge ($\tau_{ONe} \sim 0.5$) at an energy close to that of OVIII (§6.2) and most likely due to an additional screen of more-highly ionized gas covering part, or all, the cylinder-of-sight.

7.2. NGC 4151

Three datasets of NGC 4151 fulfilled the criteria defining this ‘sample’ (Paper I). These were an observation performed 1993 Nov 05 (NGC 4151(2)), an observation performed exactly 30 days later (NGC 4151(4)), and an observation performed 2 days thereafter (NGC 4151(5)). The observed count rate for NGC 4151(4) was only $\sim 2\%$ higher than that for NGC 4151(2), but that for NGC 4151(5) was $\sim 15\%$ higher. As shown in Table 12, we find a fit satisfying our criteria for acceptability is achieved for the first two observations (NGC 4151(2,4)) only when the absorbing material is allowed to be ionized *and* a fraction of the underlying continuum is allowed to escape without suffering any attenuation (i.e. models $B(ii)$ & $C(ii)$). Such an hypothesis is strongly supported by the third observation (NGC 4151(5)), even though none of the models in §5 provide a solution which formally satisfies our criteria for acceptability (see Fig. 9).

As can be seen from Tables 6 and 8, all 3 datasets are consistent with $D_f \sim 3\text{--}4\%$ and $\Gamma \sim 1.5$. However the parameters associated with the ionized gas vary in an interesting manner (see also Fig 16). In the month between the NGC 4151(2) and NGC 4151(4) observations, there is an increase in the absorbing column density ($\Delta N_{H,z} \sim 2 \times 10^{22} \text{ cm}^{-2}$) and increase in ionization parameter ($\Delta U_X \sim 30\%$), whilst the derived luminosity of the ionizing continuum (in the 0.1–10 keV for model $C(ii)$, after correcting for absorption) increases by $\lesssim 10\%$ (from $L_X \simeq 1.3$ to $1.4 \times 10^{43} \text{ erg s}^{-1}$). Two days later, at the time of the NGC 4151(5) observation, $N_{H,z}$ is similar to NGC 4151(4). However the ionization parameter has decreased ($\Delta U_X \lesssim 15\%$) despite an increase in the luminosity of the ionizing continuum (to $L_X \sim 1.8 \times 10^{43} \text{ erg s}^{-1}$). Such behaviour is difficult to understand in terms of a simple model, unless the $N_{H,z}$ and/or the number density of the gas n_H , (but not D_f) are allowed to vary on timescales $\lesssim 2$ days, or unless the photoionized gas is out of equilibrium. A simple explanation of such behaviour is that the absorbing gas completely covers the cylinder-of-sight but is inhomogeneous (with differing $N_{H,z}$ and/or n_H) on a scale comparable or greater in size to that of the central source, whilst a constant fraction D_f of the underlying continuum follows an alternate path. If the transverse velocity of the absorbing material is sufficiently high, then the movement of such clumps across the cylinder-of-sight would then give rise to variations in U_X , $N_{H,z}$ seemingly decoupled from variations in the intensity of the underlying source. Assuming only Keplerian motion, the length-scale l passing through a given line-of-sight in a time t is $l \simeq 2 \times 10^8 (f_{bolX}/f_{Edd})^{0.5} L_{X44}^{0.5} r_{ld}^{-0.5} t \text{ cm}$ at a distance r_{ld} light-days from a central object with a bolometric luminosity $L_{bol} = f_{bolX} L_{X44}$ emitting at a fraction f_{Edd} of its Eddington luminosity, where t is in seconds, $L_{X44} = 10^{44} L_X \text{ erg s}^{-1}$ and L_X defined over the 0.1–10 keV band. Equating t with the timescale t_{abs} on which significant variations in $N_{H,z}$ are seen, and putting $l \geq ct_{var}$, the size of the central source, we obtain

$$r_{ld} \lesssim 4.5 \times 10^{-5} (f_{bolX}/f_{Edd}) L_{X44} (t_{abs}/t_{var})^2 \text{ light - days} \quad (2)$$

The ratio f_{bolX}/f_{Edd} is generally considered to be $\sim \text{few}$, and from our analysis we find $L_{X44} \simeq 0.15$ for NGC 4151. Considering the variability between the 4151(2) and 4151(4) datasets and thus setting $t_{abs} \sim 30$ days, we obtain the limit $r_{ld} \lesssim 45 (f_{bolX}/f_{Edd})$ light-days assuming $t_{var} \sim 10^3$ s. The limit if the same explanation is proposed to explain the variations between the 4151(4) and 4151(5) datasets ($t_{abs} \sim 2$ days) is a factor ~ 200 smaller. We stress that these limits are based only upon the Keplerian motion, which may not be the major component governing the dynamics of the photoionized clouds.

In §6.4.3 we found that there was evidence for an additional spectral component, which we tentatively identified with the extended soft X-ray emission seen in this source and modeled as an optically-thin plasma. We found that all 3 datasets are consistent with such gas with $kT \sim 0.7 \text{ keV}$ and $L_{kT} \sim 2_{-2}^{+3} \times 10^{41} \text{ erg s}^{-1}$. Such a component alone (but

absorbed by $N_{H,0}^{gal}$) would give rise to a count rate in the range 10^{-3} – 0.07 count s^{-1} for the *ROSAT* HRI, and hence is consistent with that reported for the extended emission in this source (0.06 count s^{-1} , Morse et al 1995). However, the inclusion of this component did not significantly affect the values derived for the ionized gas (dashed contours in Fig 16), and hence the behavior of the source between the 3 observations still suggests clumps of gas of differing $N_{H,z}$ traversing the cylinder-of-sight. These results are further discussed in relation to previous studies in the Appendix.

7.3. MCG-6-30-15

Two datasets of MCG-6-30-15 are contained within our sample from observations carried out in 1993 July, separated by ~ 3 weeks, with the observed count rate $\sim 52\%$ higher for MCG-6-30-15(1) (Table 2). As shown in §5.3–5.6, there is clear evidence for ionized gas in this source, with models $B(i)$ – $C(ii)$ providing acceptable fits. In all cases a ‘1 keV deficit’ was also evident, which can be modeled by an additional absorption edge (§6.2). The best-fitting continuum for MCG-6-30-15(1) has $\Gamma \sim 2.1$, whilst that for MCG-6-30-15(2) is slightly flatter ($\Delta\Gamma \sim 0.1$). Both observations are consistent with $D_f = 0$. As shown in Fig 16, there is clear evidence for an increase in $N_{H,z}$ (by ~ 1 – 6×10^{21} cm^{-2}) over the 3 weeks between the observations. However, the ionization parameter remains constant, or perhaps even increases (but with $\Delta U_X \lesssim 50\%$), between the 2 observation despite a decrease in the luminosity derived for the ionizing continuum from $L_X \simeq 4.5 \times 10^{43}$ erg s^{-1} to $\simeq 3.0 \times 10^{43}$ erg s^{-1} (for model $C(ii)$, after correcting for absorption). Such behaviour has been reported previously for these datasets by Fabian et al (1994), and as in the case NGC 4151, is difficult to reconcile with that expected in the simplest picture whereby a uniform shell of gas reacts to changes in the intensity of the photoionizing continuum. Again appealing to only Keplerian motion to move inhomogeneities through the cylinder-of-sight between the 2 observations (i.e. setting $t_{abs} \lesssim 3$ weeks), and again setting the variability $t_{var} \sim 10^3$ s, from Eqn 2 one obtains the rather weak constraint $r_{ld} \lesssim 5 \times 10^2 (f_{bolX}/f_{Edd})$ light-days. Again we note that these limits are based upon only the Keplerian motion, which may not be the major component of the dynamics of the ionized gas.

However, there is evidence in a subsequent *ASCA* observation that whilst the depth of the OVII edge appears to be constant on long timescales in this source, the depth of the OVIII edge varies on a timescale $\sim 10^4$ s (Otani et al 1996). Such behaviour has been recently confirmed in *BeppoSAX* LECS observations (Orr et al 1997). Setting $t_{abs} \sim 10^4$ s in Eqn 2 one obtains $r_{ld} \lesssim 4 (f_{bolX}/f_{Edd})$ light-hours. However, since the photoionization and

recombination timescales for these ions are similar, such behaviour is incompatible with the observed OVII and OVIII edges being produced in the same region of ionized gas. Otani et al suggested the most natural solution was a two-zone model in which the gas giving rise predominately to the OVII edge is stable, whilst that responsible for the OVIII edge undergoes rapid variations. Such an hypothesis is of course supported by our observations of a (relatively small) '1 keV deficit' in the data/model residual of all the models considered in §5. In §6.2 we showed that this can be modeled by an additional absorption edge ($\tau_{ONe} \sim 0.14$) at an energy close to that of OVIII (see §8.8).

Both observations of MCG-6-30-15 are consistent with the presence of emission from the ionized material, with $L_e \lesssim 10^{42}$ erg s⁻¹ in the 0.1–10 keV band (after correcting for absorption). However, the signal-to-noise ratio of these datasets is too low to determine unambiguously whether the intensity of this emission responded to the decrease in the ionizing continuum.

7.4. Mrk 841

Two datasets of Mrk 841 are contained within our sample from observations carried out in 1993 August and 1994 February. The observed count rate was ($\sim 33\%$) higher for Mrk 841(1) (e.g. Table 2). In §5 we found evidence for ionized gas in this source. For models $B(i)$ – $C(ii)$, the underlying continuum for Mrk 841(1) has $\Gamma \sim 1.9$, but the values derived for U_X and $N_{H,z}$ are rather model dependent and often poorly constrained. In contrast, the data from Mrk 841(2) are consistent with a simple powerlaw, preventing any strong constraints being placed on U_X and $N_{H,z}$. In all cases, the region of the U_X – $N_{H,z}$ plane occupied by Mrk 841(1) for a given model is consistent with the limits from Mrk 841(2) assuming that model. However the underlying continuum for Mrk 841(2) does appear to be significantly flatter ($\Gamma \sim 1.7$). Dramatic spectral variability has been observed previously in this source (see Appendix and references therein). The luminosities derived for the ionizing continuum are $L_X \simeq 1.6 \times 10^{44}$ erg s⁻¹ and $\simeq 1.1 \times 10^{44}$ erg s⁻¹ for Mrk 841(1) and Mrk 841(2) respectively (for model $C(ii)$, after correcting for absorption). In view of the poor constraints which can be placed on the ionized gas from these data, few further comments can be made.

8. DISCUSSION & CONCLUSIONS

As discussed in the introduction, it is becoming increasingly clear that the spectra of a number of individual AGN contain features indicative of absorption by ionized gas within the cylinder-of-sight. It seems highly likely that this gas is photoionized by the intense radiation field produced by the central object. The aim of the work presented here was to determine the frequency and characteristics of such gas based upon new, self-consistent modelling using the ION photoionization code.

In the preceding sections we have presented the results from 23 *ASCA* observations of 18 objects. When considered together these objects certainly do not constitute a complete sample. Nevertheless, in at least some aspects, we do believe our results to be representative of the variety of properties exhibited by the type-1 AGN as a whole.

In §5 we considered models assuming the underlying continuum in the 0.6–10 keV band of our sources is well-represented by a single powerlaw. A number of models were considered, starting with the case in which the spectrum emerging from the source passes through two screens of neutral material fully covering the source: one at the redshift of the source and a second at zero redshift (with column densities $N_{H,z}$ and $N_{H,0}$ respectively). Models of increasing complexity were then considered by allowing a fraction (D_f) of the underlying continuum to be observed *without* attenuation by $N_{H,z}$, allowing the gas represented by $N_{H,z}$ to be photoionized (with an ionization parameter U_X), and finally by also including the emission spectrum expected from the ionized gas (assuming it subtends a solid angle Ω at the central source).

In §6 the results of further spectral analysis were presented, including models with additional spectral components, with the primary goal of testing the robustness of the derived characteristics of the ionized gas.

8.1. General Considerations

All models considered in this work are single-zone models, and given the assumed gas density $n_H = 10^{10} \text{ cm}^{-3}$, the gas reacts instantaneously to continuum variations. However, the models are intended to represent a wide range of conditions including cases with much lower values of n_H . In such cases, the level of ionization represents the response of the gas to the long-term, average flux of the illuminating source. We have not considered all such cases here since we do not consider the data yet warrant this level of discussion.

In §5 we found that one or more of the models considered offer an explanation of

17/23 datasets within the formal criteria outlined in §4.1. The criteria used to determine the acceptability of model as a description of the data is of course a somewhat subjective decision. The primary criterion used here that $P(\chi^2 | dof) \leq 0.95$ (i.e. that the model is a true representation of the data with a probability of better than only 1 chance in 20) might be considered relatively lax by some readers. Furthermore, as can be seen from Tables 3–8, a ‘perfect’ parameterisation of the data ($P(\chi^2 | dof) \simeq 0.5$ corresponding to a reduced- χ^2 value of unity) is only obtained in a small number of cases. Relatively high values of $P(\chi^2 | dof)$ imply that there are residuals in the data not modelled adequately. However, whilst some of these residuals might be carrying physical information associated with the source, others might be the result of inaccuracies in the calibration of the instruments (see also Fig. 13). The latter is currently under intense study by the instrument teams in anticipation of being able to assign unmodelled residuals to the former explanation with a higher degree of confidence.

However our intention in this paper is to explore just how well the data from the sample can be described by our relatively simple models for the ionized gas. We believe this approach compliments that taken by some previous workers where the absorption features introduced by the ionized material are modelled as a series of absorption edges. Throughout the analysis we have not assumed any systematic errors, and have implicitly assigned the relatively poor values of $P(\chi^2 | dof)$ to be the result of problems with the calibration in the case of 4 additional datasets in §5 (Table 12). Furthermore, beyond the limited number considered in §6, we have not explored more complex models in detail. For instance we have not considered models in which the ionized material has a significant ($\gtrsim 10^4 \text{ km s}^{-1}$) velocity dispersion along the line-of-sight. Given the spectral resolution of the SIS detectors, dispersions smaller than this value are impossible to constrain with the signal-to-noise ratio of the data presented here (see also §6.1). We have not explored different abundance ratios, or multi-component models in those cases where we have indications for their existence (see §8.8). Our intention in the present work is merely point the reader to the need of such analysis and defer it for future discussion.

8.2. The form of the underlying continuum

It is well established that many Seyfert 1 galaxies exhibit so-called ‘soft-excesses’ and ‘Compton-reflection’ tails (e.g. Turner & Pounds 1989; Nandra & Pounds 1994). After accounting for these effects, and those of the ionized-absorber, *Ginga* observations showed that the underlying X-ray continua can be generally well represented by a powerlaw of photon index $\Gamma \sim 1.9\text{--}2.0$ (e.g. Nandra & Pounds 1994). In §5 we obtained acceptable fits

for most of the datasets by one or more of the models considered, with the distribution of the photon index peaked at $\Gamma \sim 2$ (Fig. 2). In §6.4 we found significant improvements in the goodness-of-fit were obtained for many of the datasets by the inclusion of additional spectral components. However, in the majority of cases, we again found the bulk of 0.6–10 keV bandpass to be consistent by an underlying powerlaw with $\Gamma \sim 2$. It should be noted that in a number of cases the best-fitting models imply that very little of the underlying continuum is observed directly (e.g. see NGC 3783(1,2) in Fig 6; NGC 4151(2,4,5) in Fig 9). In passing we note that in such cases, Γ can still be well constrained by the data presented here as the shape of the ‘recovery’ in the absorption features in the 1–5 keV band is well defined in the models and well constrained by *ASCA* data. For comparison with other work, we have calculated the expectation value and dispersion of the distribution of spectral indices, employing the method of Maccacaro et al. (1988). Considering those datasets for which we obtained acceptable fits, we find $\langle \Gamma \rangle = 1.94 \pm 0.08$, with a significant, intrinsic dispersion of 0.18 ± 0.07 . These values are in excellent agreement with those found by *Ginga* and in Paper II, when the effects of Compton reflection are taken into consideration.

In a number of cases, complex continua do seem to be present in the *ASCA* bandpass. Mrk 335 does indeed appear to possess real curvature in the underlying continuum (Fig 15). Evidence was also found for curvature in the observed continuum in NGC 4051, IC 4392A & NGC 5548. However in at least NGC 5548 we consider the evidence for curvature in the *underlying* continuum to be questionable and/or alternative explanations are available (see §6.4.2). The observed spectrum of NGC 4151 has long been considered somewhat idiosyncratic amongst Seyfert 1 galaxies. However we do find acceptable solutions and consider the underlying continuum to indeed be a powerlaw, albeit flatter ($\Gamma \sim 1.5$) than that observed for the majority of sources (see §7 and §8.7).

8.3. The frequency of neutral absorbers

Unlike Seyfert 2 galaxies, Seyfert 1 galaxies are generally not believed to contain significant column densities of neutral gas detectable in the 0.6–10 keV band (ie. within the range $10^{20} \lesssim N_{H,z} \lesssim 10^{25} \text{ cm}^{-2}$). In the case of models $A(i)$ and $A(ii)$, the absorption at the redshift of the source (with column density $N_{H,z}$) is assumed to be due to neutral material. As described in §5.1, significant absorption is not detected in any of the datasets for which model $A(i)$ offers an acceptable solution (with $N_{H,z} \lesssim \text{few} \times 10^{20} \text{ cm}^{-2}$; see Fig 3a). Model $A(ii)$, in which a fraction D_f of the underlying continuum is able to escape without passing through $N_{H,z}$, does offer an improvement in the goodness-of-fit for many datasets, and a range of derived column densities for those in which an acceptable solution was obtained

(Fig 3b). However, as discussed in §5.2, these solutions are most likely due to a residual problem in the instrument calibration (e.g. 3C 120), lie in a region of the $N_{H,z}, D_f$ indicative of (relatively-subtle) spectral curvature (e.g. NGC 7469), and/or superior solutions are obtained assuming subsequent models (e.g. Mrk 335). We note that it has long been suggested that NGC 4151 might contain a significant column density attenuating $\sim 95\%$ of the continuum. However as shown in §5, we find acceptable solutions only for models in which the gas is ionized (see also §7 and §8.7).

We have not explicitly tested for *additional* intrinsic column densities of neutral material in any of our models which contain ionized gas (i.e. in models $B(i)$ – $C(ii)$). Such a situation might arise for example in the case where the primary continuum passes through a region of ionized gas, and then a further screen of neutral gas during its passage through the host galaxy. Nevertheless, all our models do contain a neutral column at zero redshift, $N_{H,0}$, to account for the Galactic absorption (and hence expected to be $\simeq N_{H,0}^{gal}$). At the redshift of most of the sources in our sample, any absorption by neutral material intrinsic to the source would be indistinguishable from absorption at zero redshift. Thus any such absorption would result in a derived value of $N_{H,0} \gg N_{H,0}^{gal}$. Generally we find no such evidence in our sample, with the only reliable detection in the case of IC 4329A (with a neutral column density $\sim 4 \times 10^{21} \text{ cm}^{-2}$). The host galaxy is this AGN is observed edge-on so this result is not surprizing (see Appendix).

8.4. The frequency of ionized absorbers

In §5 we found 16/23 datasets (11/18 objects) are improved at $> 99\%$ confidence over models $A(i)$ & $A(ii)$ if the absorbing material is assumed to be photoionized. Of these, 12/16 datasets (9/11 objects) can be adequately described by one or more of models including ionized gas presented in §5 (i.e. models $B(i)$ – $C(ii)$), under the assumption of a single power-law continuum. Of the remaining 4/16 datasets, 3 datasets (only one of which being from an additional object: NGC 3516) show strong evidence for ionized gas (with the statistical poverty of the fit due to further spectral complexity). Thus we find clear evidence for absorption by ionized gas in 15/23 datasets (10/18 objects). However the presence of ionized gas is also strongly suspected in 3 additional datasets (3 additional objects: NGC 4051, IC 4329A, NGC 7469) from the analysis presented in §6.

- *Thus we conclude there is evidence for ionized gas in 18/23 datasets (13/18 objects) in our sample.*

Reynolds (1997) has also presented results from a sample of 24 type-1 AGN using *ASCA* data, using the same datasets as presented here for 15 sources (Table 2). Based on a search for OVII and OVIII edges, Reynolds found strong evidence for ionized gas in 12/24 objects. These 12 include 9 sources also in our sample (Table 12), along with Mrk 290, 3C 382 and MR 2251-178. Reynolds also fitted these data with a single-zone photoionization model (based on the photoionization code *CLOUDY* which is similar in approach and scope to *ION* used here), assuming a photoionizing continuum consisting of a single powerlaw over the entire 0.0136–13.6 keV band. Converting their quoted ionization parameters (ξ) to U_X using Fig.1b, gives $1.5 \lesssim \Gamma \lesssim 2.0$, $10^{21} \lesssim N_{H,z} \lesssim 2 \times 10^{23} \text{ cm}^{-2}$ and $0.02 \lesssim U_X \lesssim 0.09$, broadly in agreement with the distributions found here (Figs 2, 3 and 7 respectively). A detailed source-by-source comparison between our results and those of Reynolds (1997) and other workers is provided in the Appendix.

8.5. Column density and ionization parameter of the ionized gas

We find no preferred value of $N_{H,z}$ under any of the models tested, with clear differences from object-to-object (e.g. Fig. 3). However, in each of the models including photoionized gas, we find the distribution in the ionization parameter strongly peaked at $U_X \sim 0.1$ (Fig. 7). Considering those datasets for which we obtained acceptable fits (and again employing the method of Maccacaro et al. 1988), we find $\langle \log U_X \rangle = -0.92 \pm 0.21$. While the values cluster around this value, there is a highly significant intrinsic dispersion in $\log U_X$ of $0.21_{-0.09}^{+0.32}$. Nevertheless this relatively narrow range in U_X is our most interesting and unexpected result. As such it deserves some further discussion as to whether it is purely the result of selection effects, or has physical significance.

We consider first values of $U_X \gg 0.1$. With the signal-to-noise ratio typically afforded by *ASCA* data, the presence of ionized gas is most readily inferred by deep ($\tau \gtrsim 0.2$) absorption edges which it introduces into the observed X-ray spectrum. For a given value of $N_{H,z}$, there is a maximum value of U_X above which the gas is unstable and goes to the high electron temperature ($T_e \sim 10^6 \text{ K}$) branch of the two-phase curve (e.g. see Fig. 2 in Netzer 1996). The value of U_X at which this thermal instability occurs is a function of the gas density and composition, along with the form of the ionizing continuum. Under the assumptions made here, the instability occurs for $U_X > 10^{-22} N_{H,z}$. Such gas is completely transparent, and the observed spectrum will be identical to the underlying (powerlaw) continuum, consistent with the data from a minority of objects in our sample. Therefore the presence of such material along the cylinder-of-sight is impossible to prove (or disprove) using the current *ASCA* data alone, offering a potential explanation of the

apparent lack of objects with $U_X \gg 0.1$ in Fig. 7.

For $U_X \ll 0.1$, different ions contribute different continuum opacity, depending on the gas composition and level of ionization. For $10^{21} < N_{H,z} < 10^{24} \text{ cm}^{-2}$ and $0.03 < U_X < 0.3$, most of the opacity is due to OVII and OVIII (Fig 8). For lower values of U_X , carbon, nitrogen and lower ionization states of oxygen are more important. However, we note that none of the objects presented here lay in the region of U_X – $N_{H,z}$ parameter-space where $U_X < 0.03$, $N_{H,z} > 10^{22} \text{ cm}^{-2}$. There is no reason *a priori* why there should not be objects with ionized material in this region. However, there is a potential selection-effect here whereby if such material lays along the cylinder-of-sight to the broad emission line region (BELR) and contains embedded dust, the broad emission lines will be absorbed by this material. This may lead to such objects being classified as something other than Seyfert 1 galaxies, and hence being excluded from the sample of sources presented here. Alternatively, should this explanation not be the case, then there must be some yet unknown mechanism that determines these unique conditions by either fixing the pressure or perhaps the dynamical state of the absorbing material. Future studies of a larger sample of objects are required to investigate these possibilities.

We have compared the parameters of the ionized gas with the derived continuum luminosity, L_X , in the 0.1–10 keV band (after correcting for absorption). We find no clear relation between $N_{H,z}$ and L_X , but some indication that $U_X \propto L_X$ (Fig. 17). If true, from the definition of U_X (Eqn. 1), this implies the ionized gas has similar densities, n_H , and is at similar radii, r in all sources. However, the majority of the sources considered here for which U_X is well constrained lie within a restricted range of L_X (10^{43} – $10^{44} \text{ erg s}^{-1}$). A recent observation of the quasar PG 1114+445 ($L_X \sim 6 \times 10^{44} \text{ erg s}^{-1}$) also exhibits strong absorption features due to ionized gas with $N_{H,z} \simeq 2 \times 10^{22} \text{ cm}^{-2}$ and $U_X \simeq 0.1$ (George et al. 1997b). Furthermore, Nandra et al (1997e) have recently reported the results from *ASCA* observations of the RQQ MR 2251-178 ($z = 0.068$, $L_X \simeq 2 \times 10^{45} \text{ erg s}^{-1}$), finding $N_{H,z} \sim 2 \times 10^{21} \text{ cm}^{-2}$ and $U_X \sim 0.07$. Inclusion of these objects on Fig. 17 argues against any obvious relation between U_X and L_X .

We found no evidence for any relationship between any other pairs of parameters derived from the X-ray results (e.g. L_X vs Γ ; Γ vs U_X ; Γ vs $N_{H,z}$). In most cases this is again primarily due to the limited range of L_X and/or Γ exhibited by most the objects in the sample. Thus, further progress requires high signal-to-noise observations of similar sources covering the high and low L_X regimes.

8.6. Constraints on ionized emitters

The dominant effects of the ionized gas on the observed spectrum from these sources is absorption by the material along the line-of-sight. However, ionized material out of the line-of-sight will give rise to emission lines and recombination continua, along with the (absorbed) continuum Compton-scattered back into the line-of-sight. The inclusion of such an emission component leads to an improvement at $>99\%$ confidence in 11 datasets (9 objects) in the full covering case (model $C(i)$), and 8 datasets (7 objects) in the partial covering case (model $C(ii)$). However there is no case for which this component is *required* (i.e. a satisfactory fit only obtained for model C). It should also be noted that the inclusion of the emission component generally does not have a significant effect on the values derived for U_X and $N_{H,z}$. For the value of U_X and $N_{H,z}$ derived for the majority of sources, the emitted spectrum contains significant line emission in the 0.6–2.0 keV band, but constitutes only a relatively small fraction ($\lesssim 10\%$) of the total flux observed in this band, even when the ionized gas subtends a large solid angle at the central source. The best-fitting values of Ω are ill-constrained, but in most cases consistent with $\Omega = 4\pi$, and there is no case where $\Omega > 4\pi$ at $> 95\%$ confidence. Formally we find $\langle \log \Omega/4\pi \rangle = 0.23_{-0.23}^{+0.24}$ for the datasets for which we obtained acceptable fits,

In cases where the ionizing continuum source is constant, then the normalization of the emission spectrum is a direct measure of the geometry of the emitting gas. However in cases where the ionizing continuum varies, then the normalization of the emission spectrum will follow the luminosity history of the continuum source, with a lag due to light travel-time effects. In the latter case we are therefore offered the opportunity to determine the location of the ionized gas via the delay in the intensity of the emission features following variations in the ionizing continuum. Unfortunately however, the signal-to-noise ratio is too low for the few objects presented here for which there are multiple observations (§7) to place even crude constraints on whether the intensity of the emission changed in an appropriate manner.

8.7. Evidence for an unattenuated component

In §5 & §6, we find that allowing a fraction D_f of the powerlaw continuum to be observed without suffering attenuation by the column density $N_{H,z}$ significantly improves the fit (compared to the corresponding model with $D_f = 0$) for a large number of dataset/model combinations. Indeed, inspection of $F(\frac{Aii}{Ai})$ (Table 4) reveals all but 3 datasets are improved in the case of model $A(ii)$, and inspection of $F(\frac{Bii}{Bi})$ and $F(\frac{Cii}{Ci})$ (Tables 6 and 8) reveals that 8 datasets are improved in the case of models $B(ii)$ and $C(ii)$.

However, in many of these cases the best-fitting solutions have $D_f \sim 1$ (Fig. 5) and as described in §6.4 are an artifact of spectral curvature. Indeed, as shown in Table 12, only in the case of 2 datasets (1 object: NGC 4151) are solutions which satisfy our criteria for acceptability obtained **only** if $D_f > 0$. Thus we conclude most of the sample show solutions close to the full-covering case and allowing D_f as a free parameter does not significantly change the properties of the sample.

As noted earlier, this model is appropriate to a partial covering of the cylinder-of-sight and to a geometry in which some fraction of the underlying continuum, initially emitted in other directions, is scattered back into the line-of-sight. As discussed in §7, a possible explanation for the spectral variability observed in NGC 4151 consists of clumps of photoionized gas (of differing column density) moving through the cylinder-of-sight on timescales $\lesssim 1$ day. Under such an hypothesis, the fact that D_f is similar for all the observations (at $\sim 5\%$) suggests scattering as the most likely explanation. Circumstantial support is provided by the observation of a similar component in many type-2 AGN, with implications for unification schemes (e.g. Turner et al 1997a,b). Indeed the optical spectrum of NGC 4151 has been observed to exhibit both type-1 and type-2 characteristics at various times. It should be noted that the parameterization used here approximates the scattered continuum as a simple powerlaw as would be appropriate in the case of pure electron scattering in a very highly-ionized medium. In a more realistic treatment, the ionization state of the scattering gas would be taken into account, which under a wide range of parameter space would lead to emission and absorption features further complicating the spectrum $\lesssim 2$ keV. It should be noted that the fact that such a component is unambiguously observed only in NGC 4151 amongst our sample is simply due to the suppression of the transmitted continuum by the high column density of gas within the cylinder-of-sight of this source (with the gas having U_X such that there’s still significant opacity)

8.8. Implications of the ‘1 keV deficit’

A number of sources have evidence for a deficit of counts at ~ 1 keV compared to the predictions of our photoionization models. As noted above, such a deficit occurs in those sources exhibiting the strongest absorption features. In §6.2 we showed that this could be modeled with an additional edge (consistent with OVIII) in the rest frame of the source.

There are several possible explanations of such a feature. First, it could be indicative that the cylinder-of-sight contains at least two absorption systems, each of different density, n_H , and column density, $N_{H,z}$. Such an hypothesis is supported in the case of MCG-6-30-15 by the short-timescale variability observed in the depth of the OVIII edge whilst the depth

of the OVII edge remains constant (§7). Circumstantial evidence for such a possibility also comes from the *Ginga* observations that a large fraction of Seyfert 1 galaxies (including some of those considered here) contain an Fe *K*-shell absorption edge, far deeper than that predicted by the models considered here (Nandra & Pounds 1994; §6.3.2). Unfortunately the geometry of the absorption systems cannot be constrained by the current data. One possible geometry is that both absorbing systems consist of complete screens, but at different radii from the central source. A full and correct treatment of such a scenario requires the ionization-equilibrium of the second screen of gas to be calculated in the same way as the first screen, but with the photoionizing continuum appropriate for that which has already passed through the first screen. Such a treatment is beyond the scope of the current paper. An alternative geometry is that the absorbing screen is clumpy on scale-sizes smaller than the emission region, resulting in the observed spectrum being the sum of the spectra transmitted by regions of different density and $N_{H,z}$. Yet another possibility is that there is indeed only a single absorbing cloud along the line-of-sight at any instant, but that different clouds (of different densities & $N_{H,z}$) move across the line-of-sight on timescales much shorter than the typical *ASCA* observation. In this case our analysis reveals time-averaged parameters of the absorber. Finally, we note that some of our detailed assumptions regarding atomic processes may be inapplicable to AGN, such as other processes important in determining the ionization equilibrium for OVII/OVIII.

Given the uncertainty in the form of the 'primary' continuum, the spectral resolution and typical signal-to-noise ratios typically achieved, it appears to be extremely difficult to distinguish between these possibilities using *ASCA* data.

8.9. The location of the ionized gas

The location and geometry of this ionized gas is currently unclear, although there are prospects for future progress. Of course if one knows the density, n_H , of the ionized gas, U_X and the intensity of the photoionizing source, one can use eqn. 1 to derive its radius as

$$r_{ld} \simeq 3 \times 10^5 \left(\frac{L_{X44}}{U_X n_H} \right)^{0.5} \text{ light - days} \quad (3)$$

Assuming $n_H = 10^{10} \text{ cm}^{-3}$ (as used for the model calculations), $U_X \simeq 0.1$ and $L_{X44} \sim 0.1-1$ (as appropriate for the majority of the objects presented here), one obtains $r_{ld} \sim \text{few}$ light-days. Such a location is comparable to that of the BELR in these objects. However as noted in §3, our models are insensitive to densities in the range $10^4 \lesssim n_H \lesssim 10^{10} \text{ cm}^{-3}$, thus values of $r_{ld} \lesssim \text{few}$ light-years cannot be excluded on this basis.

As described in §7, the apparent variations in the column density of the ionized gas

seen in the X-ray band can be used to place upper limits on the radius of the gas if one assumes these variations are due to inhomogeneities in the matter passing through the cylinder-of-sight due to *only* Keplerian motion. For the few cases observed to-date, such an assumption also implies a location close to the BELR and hence is consistent with all/part of the same gas being responsible for the absorption features seen in the optical/UV. However such estimates are currently extremely crude, and it should be stressed that the bulk motion of the ionized gas is highly uncertain and could easily be dominated by other kinematics components. Constraints on the location could be placed by applying (under certain assumptions) photoionization models to both the UV/optical and X-ray absorption features. As will be described in §8.9.2, the results from current studies are mixed and future progress requires simultaneous, high-resolution observations in all three wavebands. Reverberation mapping using the emission features produced within the ionized gas is another means whereby the location of the material could be determined. However as described in §8.6, current results are inconclusive.

However we believe that in all likelihood there is ionized gas throughout the nuclear region in AGN. Multiple components, separated in at least velocity-space are seen explicitly in the optical/UV absorption features of some objects. At least two components are implied spectroscopically and/or from temporal variations in the X-ray absorption features of some objects. In addition, highly ionized gas (occupying a different region of U_X , $N_{H,z}$ parameter-space than that responsible for the absorption on Seyfert 1 galaxies) is commonly invoked to explain the 'scattered' radiation in Seyfert 2 galaxies (e.g. see Turner et al 1997b,c).

8.9.1. *The possible effect on UV-IR observations*

Should the volume of ionized gas contain embedded dust, and is located outside the appropriate emission regions, then one might expect a correlation between the column density $N_{H,z}$ derived from X-ray observations and the various reddening indicators at longer wavebands. Such studies therefore have the potential for further constraining the location of absorbing material and/or geometry of the nuclear regions. Brandt, Fabian & Pounds (1996) have recently suggested that the infrared-bright quasar IRAS 13349+2438, which exhibits a large degree of reddening in the optical, might contain photoionized gas with internal dust. Reynolds (1997) noted that MCG-6-30-15, whose X-ray spectrum is clearly attenuated by ionized gas, also exhibits a large degree of reddening at longer wavelengths. The study of the creation, survival and implications of dust within the nuclear regions of AGN has received much attention for several decades (e.g. see Laor & Draine 1993 and

references therein).

Unfortunately the use of the various reddening indicators in order to determine the column density of dust along the line-of-sight (and which can then be compared to that observed in the X-ray regime) rely upon making one or more assumptions. The primary assumption is of course that one knows the intrinsic value of the quantity from which the observed reddening is determined. If one knew the form of underlying continuum, multiwaveband continuum measurements could be applied in the optical–UV . However such a technique often suffers from a lack simultaneous observations (as well as observational ‘contamination’ of other spectral components). Broad emission line ratios, in particular broad hydrogen lines, are poor reddening indicators since the lines are significantly affected by optical depth effects and there is no satisfactory theory to predict their intrinsic ratios (Netzer 1990). Clearly all techniques also require assumptions concerning the composition (chemical and grain-size distribution) of the dust itself, and well as the dust/gas mass ratio. With these points in mind, we consider only a single reddening indicator here (resonance-absorption line studies in the UV/optical are also considered in §8.9.2, but there do not provide a direct diagnostic of the dust-phase material).

Fig. 18 shows $(f_{125}/f_{220})_{obs}$ (defined as the mean ratio of the observed flux at 125 nm to that at 220 nm, determined as described in §2.1 and listed in Table 1) is shown against $N_{H,z}$ for the datasets for which model $C(ii)$ was considered acceptable (§5.6). It can be seen that the majority of sources are consistent with $2 \lesssim (f_{125}/f_{220})_{obs} \lesssim 5$, but that 3 datasets (NGC 3227, MCG-6-30-15(1,2)) have values a factor ~ 10 lower. Thus it is tempting to make the assumption that the intrinsic flux ratio¹⁴ is in the range $2 \lesssim (f_{125}/f_{220})_{int} \lesssim 5$, with the $(f_{125}/f_{220})_{obs}$ lower in the case of NGC 3227 & MCG-6-30-15 due to reddening. Also shown in Fig. 18 is the predicted $(f_{125}/f_{220})_{obs}$ assuming $(f_{125}/f_{220})_{int} = 3.1$ for various values of the *difference* between the optical depths at 125 nm and 220 nm (where $\Delta\tau = \tau_{125} - \tau_{220}$). It can be seen that NGC 3227 and MCG-6-30-15(1,2) are consistent with $(f_{125}/f_{220})_{int}$ similar to the other objects if their fluxes at 125 nm and 220 nm are absorbed by a column density similar to that observed in the X-ray band *and* $\Delta\tau = 0.5N_{H,z}/10^{21}$ (dashed line). Interestingly, the ‘standard Galactic’ extinction curve (for a 1:1.12 silicate:graphite mixture of dust grains with sizes $5 \leq a \leq 250$ nm, number density $\propto a^{-3.5}$ and total dust/gas mass ratio of 10^{-2} — see Laor & Draine 1993 and references therein) gives $\Delta\tau$ close to this value ($\Delta\tau = 0.42N_{H,z}/10^{21}$). Thus in the case of NGC 3227 and MCG-6-30-15(1,2), and

¹⁴It should be stressed that line emission may contribute to f_{125} and (to a lesser extent) f_{220} , and thus $(f_{125}/f_{220})_{int}$ is not necessarily a good indication of the underlying UV continuum. However, the use of the color here is only based on noting $(f_{125}/f_{220})_{obs}$ appears to be crudely constant (within a factor ~ 2) for the majority of the objects considered.

assuming a Galactic dust/gas mass ratio, this UV color is consistent with reddening by a column density of dusty material similar to that inferred by the X-ray observations. There are several implications of these results.

First, we consider the implications on the location of the dust and gas in the case of NGC 3227 and MCG-6-30-15. The consistency between the $N_{H,z}$ derived from the X-ray absorption studies and the UV-reddening in the case of these two sources, assuming a ‘reasonable’ dust/gas mass ratio, implies that the dust- and gas-phase material might occupy the same volume. If true, this allows us to place constraints on the location of this material based upon the survival of the dust. For a typical AGN continuum of bolometric luminosity $L_{bol} = f_{bolX}L_{X44}$ (as defined in §7.2), and assuming maximum equilibrium temperature of ~ 1750 K, Laor & Draine find sublimation radii of $r_{sub} \simeq 20(f_{bolX}L_{X44})^{1/2}$ light-days and $\simeq 150(f_{bolX}L_{X44})^{1/2}$ light-days for graphite grains with $a = 10^{-3}$ cm and 5×10^{-7} cm respectively. (Silicate grains, with a slightly lower maximum equilibrium temperature (~ 1400 K), have slightly larger values of r_{sub} .) Assuming $f_{bolX} \simeq 4$, $r_{sub} \sim 10$ light-days and ~ 5 light-days for large graphite grains in MCG-6-30-15 ($L_{X44} \simeq 0.3$) and NGC 3227 ($L_{X44} \simeq 2 \times 10^{-2}$) respectively. The corresponding value in the case of NGC 5548 ($L_{X44} \simeq 1$) is $r_{sub} \sim 40$ light-days for large graphite grains. The latest results from the intensive reverberation mapping of the broad emission line region (BELR) in NGC 5548 have suggested lags of $\lesssim 2 \sim 14$ days, with the lowest lags seen in the highest ionization lines (e.g. Korista et al 1995 and references therein). As first pointed out by Netzer & Laor (1993), since both the radius of the BELR and r_{sub} scale as $L_{bol}^{1/2}$ we conclude dust can only survive (i.e. in *equilibrium*) at radii just beyond the BELR in these objects. If the dust covers a substantial fraction of the BELR, then it will attenuate the broad emission lines in these objects. For instance, assuming the same ‘standard Galactic’ extinction curve used above, $\tau(\text{CIV}) = 9N_{H,z}/10^{22}$ at the energy of CIV emission. Thus from the values of $N_{H,z}$ found in MCG-6-30-15 and NGC 3227, a broad CIV emission line is predicted to be totally absent in both sources, consistent with observations (see e.g. Courvoisier & Paltani 1992). The extinction in the optical is lower (e.g. $\tau(\text{H}\beta) = 3N_{H,z}/10^{22}$, $\tau(\text{H}\alpha) = 2N_{H,z}/10^{22}$) but sufficient to attenuate $\sim 80\%$ and $\sim 95\%$ of the broad $\text{H}\beta$ line, and $\sim 65\%$ and $\sim 85\%$ of the broad $\text{H}\alpha$ line in NGC 3227 and MCG-6-30-15 respectively (again assuming the dusty absorber completely covers the entire BELR). However it is clear from the value of r_{sub} above and the discussion in §7.3 that dusty clouds cannot survive at a sufficiently small radius that Keplerian motion alone can offer an explanation of the short-timescale variability ($\sim 10^4$ s) in the OVIII edge observed in MCG-6-30-15. Thus either the dusty absorber is extremely non-uniform and/or its kinematics are extremely non-Keplerian, or (far more likely) the gas giving rise to the bulk of the OVIII edge is at much smaller radii than that with embedded dust. Interestingly NGC 3227 and MCG-6-30-15 have the lowest

axial ratios (a/b , Table 1) in our sample, with the exception of the well-known, edge-on galaxy IC 4329A.

We now consider the majority of the objects on our sample, for which $(f_{125}/f_{220})_{obs}$ provides no evidence for reddening. There are two obvious explanations. First, the column density of ionized gas within the cylinder-of-sight may simply not contain any embedded dust in these objects. This might arise from differences in the origin of the material, or as a result of the material in these objects being within r_{sub} . Alternatively the dust may be present yet unobservable. This will true if the dust is of a different composition in which $\Delta\tau \sim 0$ (such as is the case if the grains are large), or if the dust clouds cover only a fraction of the UV emission region.

8.9.2. Relationship to ‘associated absorbers’ in the UV/optical

The presence of highly-ionized gas, intrinsic to the Seyfert 1 nuclei is also obtained from observations carried out in the UV. *IUE* observations revealed only a small fraction ($\sim 3\%$) of sources to exhibit narrow absorption lines close to the systemic velocity (e.g. Ulrich 1988). However, recent results taking advantage of the higher spectral resolution and signal-to-noise ratio available with the FOS and GHRS instruments onboard *HST* have revealed that up to 50% of Seyfert 1 galaxies may in fact contain such absorption features (e.g. Crenshaw 1997). Such features have also been reported in *HUT* observations of NGC 4151 (Kriss et al. 1992) and NGC 3516 (Kriss et al. 1996b). Furthermore variability in the UV absorption features have been observed on timescales of weeks–years in NGC 4151 (Bromage et al. 1985), NGC 3783 (Maran et al 1996), and NGC 3516 (Koratkar et al. 1996), and multiple radial velocity components have been reported in Mrk 509 (Crenshaw, Boggess & Wu 1995) and NGC 3516 (Crenshaw, Maran & Mushotzky 1997).

As noted by Crenshaw (1997), there is a reassuring trend whereby Seyfert 1 galaxies which have evidence for strong absorption features due to ionized gas in the X-ray band also tend to have strong absorption lines in the UV/optical. This raises the question as to whether the associated absorbers seen the UV/optical are caused by (part or all of) the same ionized material which gives rise to the absorption features observed in the X-ray band. The UV absorption components are often blueshifted with respect to the emission lines, but with velocity shifts (typically $\sim \text{few} \times 10^2 \text{ km s}^{-1}$) too small to be detectable with current X-ray observations. Thus direct tests for kinematic consistency are not yet possible. However various attempts have been made to relate the UV/optical and X-ray absorption features using photoionization calculations (e.g. Mathur 1994; Mathur et al. 1994; Mathur, Wilkes & Elvis 1995; Shields & Hamann 1996; Kriss et al 1996a,b). These have met

with varying degrees of success, which is hardly surprising given the uncertainties in the location and kinematics of the gas and the spectral form of the photoionizing continuum. Nevertheless there have been a number of impressive successes linking the UV/optical and X-ray absorbers (e.g. see Mathur 1997). The observed UV/optical absorption features are often superimposed on the wings of broad emission lines. This clearly places the gas responsible for these 'associated absorbers' at radii greater than that where the bulk (of the blue-wing) of that emission line originates ($\lesssim 2 \sim 14$ light-days in the case of NGC 5548). However ionized gas could exist at a wide range of radii, with only part of the gas responsible for the X-ray absorption within the cylinder-of-sight to the UV/optical emission line region(s). Indeed the presence of multiple components to the UV/optical absorption features (and the indication of additional absorption zones in the X-ray — e.g. §8.8) clearly indicates a single screen of gas to be an over-simplification. Thus the column densities implied by the UV/optical absorption features may be small (and dominated by different ionization states) compared to those implied from the X-ray features. Furthermore, the emission and absorption features predicted in the UV/optical from the ionized gas are somewhat dependent on the form of the photoionizing continuum in the UV–X-ray band. This is poorly determined for all objects, leading to further ambiguities. In addition, in at least some objects the absorption features in both the UV and X-ray are known to vary with time. To date, most comparisons between the absorption features have been performed using non-simultaneous data, leading to obvious risk of deception. Finally, there is the usual irritation of uncertainties in the abundances within the absorbing material. The best hope for progress is provided by intense, simultaneous monitoring of the UV/optical and X-ray absorption features.

9. SUMMARY & OPEN ISSUES

We have presented the systematic analysis of the 0.6-10 keV *ASCA* spectra of 18 Seyfert 1 galaxies in order to examine the characteristics of X-ray absorption by ionized gas.

9.1. Summary of Results

In summary, we find:

- For the majority of sources, an underlying powerlaw with $\Gamma \sim 2$ dominates the emission within the *ASCA* bandpass (§8.2 and Fig. 2).
- Absorption by neutral material does not provide a satisfactory model for the X-ray

attenuation for most objects (§8.3). However, there is evidence for a significant column density of ionized gas in the line-of-sight to 13/18 objects (§8.4).

- The X-ray ionization parameter for the ionized material is strongly peaked at $U_X \sim 0.1$ (Fig. 7), which may in part be the result of selection effects. The column densities of ionized material are typically in the range $N_{H,z} \sim 10^{21}\text{--}10^{23}\text{cm}^{-2}$ (Fig. 3), although highly ionized (and hence psuedo-transparent) column densities up to 10^{24}cm^{-2} cannot be excluded in some cases (see also §8.5)
- Allowing a fraction of the continuum to be observed without attenuation significantly improves the fit to many sources (§8.7 and Fig. 5). Such a component is required only in the case of NGC 4151.
- Inclusion of the emission from the ionized material significantly improves the fit to many sources, at an intensity consistent with the material subtending $\sim 4\pi$ sr at the central source. However such a component is not required in any individual source (§8.6 and Fig. 11).
- A deficit of counts is observed at ~ 1 keV in the sources exhibiting the strongest absorption features (§8.8). This is consistent with the presence of a second zone of (more highly) ionized gas, which might have been seen previously in the deep Fe K -shell edges observed in some *Ginga* observations.
- There is evidence that the ionized material in NGC 3227 and MCG-6-30-15 contains embedded dust, whilst no such evidence in the other sources (§8.9.1 and Fig. 18).

9.2. Open issues

While X-ray absorption by ionized gas appears to play a very important role in shaping the observed X-ray spectra of AGN, there remain a large number of important questions which cannot be answered with the available data, including:

- What is the frequency of occurrence of warm absorbers at higher luminosities. Is there a simple relationship between U_X and L_X ?
- Are there several distinct warm absorber components attenuating the X-ray bandpass ?

- What is the location, density and distribution of the material comprising the X-ray warm absorber ? Sensitive measurements of the emission spectrum from the gas will help to constrain the gas distribution.
- Is the warm absorber flowing into or out from the active nucleus ? Do the UV associated-absorbers arise from the same X-ray absorbing gas ?
- Does the gas to dust ratio differ significantly between objects, and how does this affect the observed properties of the source ? How important is this component in the unification of AGN ?
- Is the absorption variability due to bulk motion of material across the line-of-sight, variable ionization or a combination of both effects ?
- How stable is the warm absorbing gas ?

We thank the *ASCA* team for their operation of the satellite, and Keith Gendreau, Mike Crenshaw and the members of the *ASCA* GOF at NASA/GSFC for helpful discussions. We would also like to thank an anonymous referee whose carefully reading of the manuscript and thoughtful comments led to a great improvement in the final version. We acknowledge the financial support of the Universities Space Research Association (IMG, TJT), National Research Council (KN) and a special grant from the Israel Science Foundation (HN). This research has made use of the Simbad database, operated by CDS, Strasbourg, France; of the NASA/IPAC Extragalactic database, which is operated by the Jet Propulsion Laboratory, Caltech, under contract with NASA; and of data obtained through the HEASARC on-line service, provided by NASA/GSFC.

APPENDIX: NOTES ON INDIVIDUAL OBJECTS

The sources presented here are all well-known, bright Seyfert 1 galaxies, detected early in the history of X-ray astronomy. Thus, most have been observed by all the major X-ray astronomy satellites. The results from, and references to, almost all X-ray observations published prior to the end of 1992 are included in the compilation of Malaguti, Bassini & Caroli (1994). The following abbreviations are used for papers cited numerous times in this section: NP94 – Nandra & Pounds (1994); R97 – Reynolds (1997); TP89 – Turner & Pounds (1989); T91 – Turner et al (1991); W95 – Weaver, Arnaud & Mushotzky (1995). As stated in §8.4, R97 also fitted a single-zone photoionization model to a number of sources, and quotes the ionization parameter ξ ($= L/n_H R^2$, where n_H and R are as defined in eqn.1, but where L is the integrated luminosity) calculated over the 0.0136–13.6 keV band assuming a single powerlaw. For convenience, below we give the corresponding U_X^{R97} (defined as in eqn.1 for such a continuum over the 0.1–10.0 keV band) using the conversion factors shown in Fig. 1b. *Ginga* observations have shown evidence for a significant Fe absorption edge in the 7.1–8.9 keV band for a number of sources (NP94), in some cases confirming suggestions in earlier observations. These sources are noted, but as described in §6.3.2 a detailed analysis of such features has not been attempted here. Unless otherwise stated, the Seyfert classification is from Whittle (1992) and all limits on a parameter are quoted at 90% confidence for 1 interesting parameter.

As a reminder, models $A(i)$ – $C(ii)$ all assume a single powerlaw continuum absorbed by a neutral column density at $z = 0$ (constrained to be $\geq N_{H,0}^{gal}$, the Galactic HI column density along that line-of-sight) and an additional column density, $N_{H,z}$, at the redshift of the source. In models A (§5.1–5.2) $N_{H,z}$ is assumed to be neutral, whilst in models B (§5.3–5.4) & C (§5.5–5.6) $N_{H,z}$ is assumed to be photoionized, with a corresponding ionization parameter U_X . Models C also include the emission features expected from the ionized gas (assuming it subtends a solid angle Ω at the central source). In the models denoted (i) , the absorbing gas covers the entire cylinder-of-sight to the source, whilst in models (ii) a fraction D_f of the underlying continuum are observed without attenuation. See §4 for further details.

Mrk 335:

This Seyfert 1.0 galaxy was first detected in X-rays by *UHURU* (Tananbaum et al 1978). From our analysis of the data from *ASCA* observation performed in 1993 December, we find model $A(i)$ to provide an unsatisfactory description of the spectra (Table 3). Fits satisfying our criteria for acceptability are obtained if $\sim 60\%$ of the continuum escapes without suffering attenuation by neutral material (model $A(ii)$) and for all the models in which the absorbing gas is assumed to be ionized (models $B(i)$ – $C(ii)$). However, in §6.4.2 we obtained

a superior fit if the continuum is assumed to be the sum of a steep powerlaw ($\Gamma_s = 3.3_{-0.7}^{+2.0}$) dominating at energies $\lesssim 1$ keV and a flatter powerlaw ($\Gamma_h \sim 1.8_{-0.5}^{+0.2}$) dominating at energies $\gtrsim 3$ keV. This model gave $\chi^2/dof = 621/642$, had $R_{s/h} \sim 1.6$ and required no absorption in addition to $N_{H,0}^{gal}$. Such a double-powerlaw continuum is in good agreement with previous observations (Turner et al 1993b and references therein). The flux in the 2–10 keV band during the *ASCA* observation was $F_{2-10} = 9.5 \times 10^{-12}$ erg cm $^{-2}$ s $^{-1}$, similar to that during the *BBXRT* era, and indeed the X-ray spectrum of Mrk 335 appears relatively stable on long timescales, though the source exhibits variability on short timescales (Pounds et al 1987; Lee et al 1988; Paper I). In an independent analysis of the same *ASCA* dataset, R97 modeled the continuum in terms of single powerlaw and a blackbody (with $kT \sim 0.14$ keV and luminosity $L_{bb} \sim 10^{43}$ erg s $^{-1}$) to account for the steepening to low energies. We confirm these results, but find such a model provides an inferior description of the data ($\chi^2/dof = 629/641$) compared to the double-powerlaw model. Explanations for the X-ray continuum in Mrk 335 have been presented which involve e^\pm -pair cascades (Turner et al 1993b) and the Comptonization of the spectrum emitted by an accretion disk (Zheng et al 1995a).

We find any features imprinted by any ionized gas to be relatively weak during the epoch of the *ASCA* observation, resulting in poor constraints on $N_{H,z}$ and U_X in models *B(i)–C(ii)*. Turner, George & Mushotzky (1993) found evidence for an absorption edge ($\tau \sim 0.3 \pm 0.1$) in the 0.7–0.9 keV band during a *ROSAT* PSPC observation of Mrk 335. Furthermore, R97 found the addition of an OVII edge (of optical depth $\tau_{O7} \sim 0.3$) significantly improved the fit to a single powerlaw model ($\Gamma \sim 2.1$) to these *ASCA* data. However, we find only a marginal improvement ($\Delta\chi^2 = 4$) when such an edge ($\tau_{O7} = 0.2 \pm 0.2$) is added to our double-powerlaw model, and no improvement when an OVIII edge is also included ($\tau_{O8} \lesssim 0.1$). Some evidence exists for a Fe *K*-shell edge in the 7.1–8.9 keV band in two *Ginga* observations (NP94), and possibly in an *EXOSAT* observation (Turner et al 1993b). The energy of the features could not be constrained in any of the datasets, but NP94 inferred $N_{H,z} \sim 2 \times 10^{23}$ cm $^{-2}$.

There is no evidence for any UV absorption features due to ionized gas at the redshift of Mrk 335 (Zheng et al 1995a; Crenshaw 1997).

Fairall 9:

This Seyfert 1.0 galaxy was suggested to be an X-ray source based upon its location in *UHURU* and *Ariel-V* error boxes (Ricker 1978). From our analysis of the data from *ASCA* observation performed in 1993 November, we find no model in §5 which satisfies our formal criteria for acceptability. However, this is primarily due to scatter in 2–4 keV band, most likely due to an underestimation of systematic errors for this dataset. In view of this,

we consider model $A(i)$ to provide an adequate description of the data. However model $A(ii)$ provides a significant improvement in the goodness-of-fit if $\sim 80\%$ of the continuum escapes without attenuation by a large column density ($N_{H,z} \sim 3 \times 10^{23} \text{ cm}^{-2}$) of neutral material which gives rise to a relatively subtle upturn in the spectrum $\gtrsim 5 \text{ keV}$ (Fig 4). No significant improvement in the goodness-of-fit was obtained assuming the more complex models described in §5 or §6. For all models we find no evidence for absorption in addition to $N_{H,0}^{gal}$ and a derived slope ($\Gamma \simeq 2.0$) consistent with the *Einstein* (T91) and *EXOSAT* (TP89) observations of the source, slightly steeper than that observed by *Ginga* ($\Gamma = 1.84$, NP94) and only marginally consistent with the *ROSAT* PSPC observations ($\Gamma = 2.2 \pm 0.2$, Walter & Fink 1993). X-ray variability has been reported on both short and long timescales (Morini et al 1986; Paper II). Unfortunately these *ASCA* do not offer any insight into the possible spectral variability suggested by the *EXOSAT* observations (Morini et al 1986). However, we note that the flux in the 2–10 keV band observed during both the *Ginga* (NP94) and this *ASCA* observation ($F_{2-10} = 2 \times 10^{-11} \text{ erg cm}^{-2} \text{ s}^{-1}$) indicates that the historical decline in the brightness of Fairall 9 in the X-ray band (Morini et al 1986) has ceased.

We find any features imprinted by any ionized gas to be weak during the epoch of the *ASCA* observation, resulting in poor constraints on $N_{H,z}$ and U_X in models $B(i)$ – $C(ii)$. R97 also found a lack of evidence for OVII and OVIII absorption edges in their analysis of the *ASCA* data from Fairall 9. They find a best-fitting photon index consistent with our value, although unlike our findings, require a small column density ($N_{H,z} \sim 10^{20} \text{ cm}^{-2}$) of intrinsic absorption.

There is no evidence for any UV absorption features due to ionized gas at the redshift of Fairall 9 (Zheng et al 1995b; Crenshaw 1997).

3C 120:

This bright, flat-spectrum radio source, has Seyfert 1 properties in the optical regime. The source was first detected in X-rays by *SAS-3* (Schnopper et al 1977), and has since been observed by all the major X-ray astronomy satellites except *Ginga*. From our analysis of the data from the *ASCA* observation performed in 1994 February, we find model $A(i)$ to provide an adequate description of the spectra, with some evidence for intrinsic absorption ($N_{H,z} \sim 5 \times 10^{20} \text{ cm}^{-2}$). However, we find some evidence for a 'hard tail' in this source, with significantly superior fits obtained if $\sim 30\%$ of the continuum is attenuated by $N_{H,z} \sim 5 \times 10^{23} \text{ cm}^{-2}$ (model $A(ii)$; Fig. 4), or by a flattening of the underlying continuum $\gtrsim 6 \text{ keV}$ (§6.4.2). We find no compelling evidence for ionized gas in 3C 120 (intense emission from ionized gas is implied by the best-fitting solution assuming model $C(ii)$, but at a level incompatible with strength of the observed Fe K -shell line – see Fig 12). This

confirms the finding of R97 who also found a lack of evidence for OVII and OVIII absorption edges in their analysis of these *ASCA* data. They find a best-fitting photon index consistent with our value, but a slightly larger absorbing column density intrinsic to the source ($N_{H,z} \sim 8 \times 10^{20} \text{ cm}^{-2}$) then we found for model $A(i)$.

In all cases, the derived slope is $\Gamma \simeq 2.0$, and is consistent with a poorly constrained *ROSAT* PSPC spectrum ($\Gamma \sim 1.5_{-1.8}^{+1.2}$, Boller et al 1992), and slightly steeper than those derived from *HEAO-1*, *Einstein* and *EXOSAT* ($\Gamma \sim 1.5\text{--}1.9$, W95; T91; TP89). Spectral variability was apparent in the *Einstein* observations (T91). Unfortunately the *ASCA* data are unable to constrain the Compton-Reflection component seen in *HEAO-1* observations (W95), although such a component clearly offers an alternative explanation of the hard tail. We also note that many of the fits to the 3C 120 dataset imply a local column density $> N_{H,0}^{gal}$ ($\Delta N_{H,0} \simeq 5 \times 10^{20} \text{ cm}^{-2}$). Furthermore this dataset seems particularly badly affected by a trough-like deficit of counts at energies $< 0.6 \text{ keV}$ compared to the extrapolated model. It is unclear how these facts may be related to the well-known, but poorly-understood calibration problems of the XRT/SIS at these energies (see also §2.3).

NGC 3227:

This Seyfert 1.2 galaxy was first detected in X-rays by *Ariel-V* (Elvis et al 1978). In our analysis of the data from *ASCA* observation performed in 1993 May, we find model $A(i)$ to provide an unsatisfactory description of the spectra (Table 3). Fits satisfying our criteria for acceptability are obtained if $\sim 35\%$ of the continuum escapes without suffering attenuation by neutral material (model $A(ii)$; Fig. 4). However yet superior fits are obtained if the absorbing gas is assumed to be ionized (model $B(i)$; Fig. 6). The parameters of the ionized gas are fairly well constrained, with $U_X \simeq 10^{-2}$ and $N_{H,z} \sim 4 \times 10^{21} \text{ cm}^{-2}$ consistent with the findings of Ptak et al (1994) and R97 ($U_X^{R97} \simeq 0.02$, $N_{H,z} \sim 4 \times 10^{21} \text{ cm}^{-2}$) in their independent analysis of this *ASCA* observation.

We find that statistically there is no requirement for any of the underlying continuum to escape without suffering attenuation by the ionized material, or for any significant emission from the ionized gas, (models $B(ii)$ – $C(ii)$). In all cases there is no requirement for additional absorption by neutral gas in excess of $N_{H,0}^{gal}$. The derived photon index ($\Gamma \sim 1.6$) found for NGC 3227, is flatter than for the majority of the sources (Fig. 2), consistent with previous measurements by *HEAO-1* (W95), *Einstein* (T91), *EXOSAT* (TP89), *Ginga* (NP94) and *ROSAT* (Rush et al 1996). However, it is important to note that *EXOSAT* observations of NGC 3227 revealed significant spectral variability on timescale as short as 10^4 s , most likely as a result of changes in absorption (TP89). Furthermore, such variability was also present during the *ASCA* observation presented here (Ptak et al 1994; Paper I).

Thus it should be remembered that our results most likely represent the time-averaged values. We note evidence was found for a Fe *K*-shell edge in the 7.1–8.9 keV in two *Ginga* observations of the source. NP94 found evidence for absorption by ionized gas with $N_{H,z} \sim 3 \times 10^{22} \text{ cm}^{-2}$, higher than that observed here.

NGC 3516:

This source, one of the original galaxies classified by Seyfert (1943) as a type 1.0 galaxy, was first detected in X-rays by *Einstein* (Maccacaro, Garilli & Mereghetti 1987). In our analysis of the data from an *ASCA* observation performed in 1994 April, we find no model in §5 which satisfies our formal criteria for acceptability. Nevertheless, we find model *B(i)* to provide a significant improvement over models *A(i)* & *A(ii)*, offering clear evidence for ionized gas and confirming the results of R97 and those from a second *ASCA* observation carried out in 1995 March (Kriss et al 1996a). However, whilst a single-zone photoionization model clearly reveals a strong ‘ $\sim 1 \text{ keV}$ ’ deficit in this source, we find that despite providing a vast improvement, a satisfactory fit is still not obtained with the inclusion of an additional absorption edge (§6.2). Interestingly, we note that neither R97 nor Kriss et al (1996a) were able to find a solution which satisfy our criteria for acceptability. We find a derived index ($\Gamma \sim 1.9$), steeper than that which has been claimed from previous *Einstein* (Krupe, Canizares & Urry 1990), *EXOSAT* (Ghosh & Soundararajaperumal 1991) and *Ginga* (Kolman et al 1993) observations in the 2–10 keV band. However all these observations required a neutral $N_{H,0} \gg N_{H,0}^{gal}$, undoubtedly due to the incorrect modelling of the deep OVII and OVIII edges in this source with neutral gas. A steeper index ($\Gamma \gtrsim 2.4$) is implied when a single powerlaw model is applied to the *ROSAT* PSPC data (Boller et al 1992), again probably the result of the deep OVII and OVIII edges. For models *B(i)*–*C(ii)*, we find a neutral $N_{H,0} \sim 5 \times 10^{20} \text{ cm}^{-2}$ and an ionized $N_{H,z} \sim 9 \times 10^{21} \text{ cm}^{-2}$, with $U_X \sim 0.1$. For comparison, R97 find $N_{H,z} \sim 10^{22} \text{ cm}^{-2}$, $\Gamma \sim 1.7$ and $U_X^{R97} \sim 0.06$ from an independent analysis of the *ASCA* dataset obtained in 1994 April, and assuming a single-zone model. Kriss et al (1996b) have performed a detailed analysis of the 1995 March observation (using XSTAR), and for a single-zone model find $U_X \sim 0.03$ (assuming their quoted spectrum), $N_{H,z} \sim 10^{22} \text{ cm}^{-2}$ and $\Gamma \sim 2.0$. These workers also find adding a second zone of ionized gas significantly improves the fit, obtaining a best-fitting solution with $U_X \sim 0.1$, $N_{H,z} \sim 1.4 \times 10^{22} \text{ cm}^{-2}$ and $U_X \sim 0.02$, $N_{H,z} \sim 7 \times 10^{21} \text{ cm}^{-2}$ for the two zones. Nandra et al (1997c) have recently shown the Fe emission line varied significantly between the two *ASCA* observations. Evidence for absorption by ionized gas was found in 3 *Ginga* observations of NGC 3516, with $N_{H,z} \sim 2\text{--}3 \times 10^{23} \text{ cm}^{-2}$ (Kolman et al 1993). We also note that *ROSAT* HRI observations show possible evidence for elongation of some fraction of the soft X-ray emission in NGC 3516 in a direction consistent with the extended narrow-line region (Morse et al 1995).

NGC 3516 has long been known to exhibit deep, variable absorption lines in the UV (Koratkar et al. 1996; Kriss et al 1996a and references therein) with at least 4 distinct radial components visible in C IV (Crenshaw, Maran & Mushotzky 1997). From the combined analysis of the simultaneous *ASCA* and *HUT*, Kriss et al (1996b) conclude that a range of column densities and ionization parameters are required to explain the depths of all the X-ray and UV absorption features seen in NGC 3516.

NGC 3783:

This Seyfert 1.2 galaxy was first detected in X-rays by *Ariel-V* (Cooke et al 1976). Absorption due to ionized gas in NGC 3783 was first suggested by *ROSAT* PSPC observations (Turner et al 1993). In our analysis of the data from 2 *ASCA* observations separated by 4 days in 1993 December, we find models involving absorption by neutral material (model $A(i)$ & $A(ii)$) to provide unsatisfactory descriptions of the spectra. However fits satisfying our criteria for acceptability are obtained if the absorbing gas is assumed to be ionized (models $B(i)$ & $B(ii)$), with a significant improvement in the goodness-of-fit with the inclusion of the ionized emitter (models $C(i)$ & $C(ii)$). In all cases, the parameters of the ionized gas are fairly well constrained, with $U_X \sim 0.1$ – 0.15 and $N_{H,z} \sim 2 \times 10^{22} \text{ cm}^{-2}$ (e.g. Fig.16). This confirms the findings of George, Turner & Netzer (1995), and R97 who found the addition of OVII and OVIII edges (of optical depths $\tau_{O7} \sim 1.2$ & $\tau_{O8} \sim 1.4$) significantly improved the fit to a single powerlaw model ($\Gamma \sim 1.4$) to these *ASCA* data. R97 also fitted a single-zone photoionization model and found $U_X^{R97} \sim 0.08$, $N_{H,z} \sim 2 \times 10^{22} \text{ cm}^{-2}$, $\Gamma \sim 1.7$. The index derived for these *ASCA* observations (~ 1.8) is somewhat steeper than that found by George et al (1995), primarily due to these workers not adequately modeling the Fe *K*-band. A flatter spectral index has also been suggested by some (but not all) previous observations in the 2–10 keV band (e.g. Ghosh et al 1992). This may indicate spectral variability or (more likely) be an artifact of incorrectly modeling the deep absorption troughs due to the ionized gas in this source. As described in §7.1, the behaviour of the ionized gas in response to the change in flux seen between the two *ASCA* observations is consistent with expectations. NP94 found evidence for absorption by ionized gas with $N_{H,z} \sim 10^{23} \text{ cm}^{-2}$, higher than that observed here.

UV observations of NGC 3783 have revealed absorption due to Ly α , Nv and C IV, with the latter exhibiting variability on a timescale of $\lesssim 6$ months (Reichert et al 1994; Lu et al 1994; Maran et al 1996). Shields & Hamann (1997) have compared the implied column densities with the photoionization modeling of the X-ray absorption presented in George et al (1995). Whilst alternative scenarios could not be excluded, they found the UV and X-ray results to be consistent with a single-phase, photoionized plasma. By comparing the observed variability timescale in C IV with the radiative recombination, they derived a density $n \gtrsim 50 \text{ cm}^{-3}$ for the ionized gas and hence, from the ionization parameter, a

location $r \lesssim 30$ pc from the ionizing source. Since the parameters associated with the X-ray absorption are generally consistent with those in George et al (1995), we agree with the conclusions of Shields & Hamann (1997).

NGC 4051:

This Seyfert 1.5 galaxy was first detected in X-rays by *Einstein* (Marshall et al 1983) and has been seen to exhibit rapid variable on timescales as short as $\text{few} \times 10^2$ s (e.g. Lawrence et al 1987). Indeed, in Paper I we showed NGC 4051 the source to exhibit the most pronounced variability of any of the sources considered. Absorption due to ionized gas in this object was first suggested by *ROSAT* PSPC observations (Pounds et al 1994). In our analysis of the data from the *ASCA* observation performed in 1993 April, we find no model in §5 which satisfies our formal criteria for acceptability. A satisfactory fit is found however, if a strong ($\mathcal{F} \sim 4$) Compton-reflection component is included in the model (§6.4.1).

However, such a curvature in the observed spectrum may be due in part to the spectral variability observed during the observation (Paper I). Nevertheless, we do find a significant improvement in the fits for models including ionized gas, with $U_X \sim 0.7$, $N_{H,z} \sim 2\text{--}10 \times 10^{22} \text{ cm}^{-2}$, $\Gamma \sim 2.3$ for all models *B(i)–C(ii)*, and $U_X \sim 0.4$, $N_{H,z} \sim 10^{22} \text{ cm}^{-2}$, $\Gamma \sim 2.4$ for the model including Compton-reflection (Table 10). Mihara et al (1994) and R97 have both performed independent analyses of this *ASCA* dataset. Both find the addition of two edges to a single powerlaw model significantly improved the goodness-of-fit over the 0.6–1.0 keV band, confirming the results from the *ROSAT* PSPC and from a later *ASCA* observation carried out in 1994 July (Guainazzi et al 1996). R97 fixed the edge energies to those appropriate for OVII and OVIII and found $\tau_{O7} \sim \tau_{O8} \sim 0.2$.

Photoionization models were also applied to these *ASCA* data by Mihara et al and R97, as well as to the earlier *ROSAT* PSPC data (Pounds et al 1994; McHardy et al 1995) and data from the later *ASCA* observation (Guainazzi et al 1996). Unfortunately detailed comparisons are difficult due to differing assumptions regarding the form of the observed and photoionized spectra. Mihara et al find $\xi \sim 50$ (but for an unspecified XUV continuum) and $N_{H,z} \sim 2 \times 10^{21} \text{ cm}^{-2}$ when the observed continuum is modeled by a (relately) flat powerlaw ($\Gamma \sim 1.9$) plus a low temperature blackbody ($kT \sim 0.1$ keV and luminosity $L_{bb} \sim 3 \times 10^{41} \text{ erg s}^{-1}$). R97 find $U_X^{R97} \sim 0.02$, $N_{H,z} \sim 10^{21} \text{ cm}^{-2}$ and $\Gamma \sim 1.9$, but also find evidence for a similar blackbody component. From the analysis of combined *ROSAT–Ginga* data Pounds et al (1994) also prefer the inclusion of a blackbody ($kT \sim 0.2$ keV and $L_{bb} \sim 5 \times 10^{41} \text{ erg s}^{-1}$) and powerlaw ($\Gamma \sim 2.1$) finding $N_{H,z} \sim 7 \times 10^{22} \text{ cm}^{-2}$ and $U \sim 0.8$ (but for an unspecified XUV continuum). From subsequent *ROSAT* data McHardy et al (1995) find $U_X \sim 0.5$ (given their continuum), $N_{H,z} \sim 8 \times 10^{22} \text{ cm}^{-2}$ and $\Gamma \sim 2.2$, with no requirement for a cool thermal component. Finally, Guainazzi et

al find $N_{H,z} \sim 2 \times 10^{22} \text{ cm}^{-2}$, $\Gamma \sim 2.1$ and $U_X \sim 0.2$ (given their continuum). These workers found evidence for additional emission $\lesssim 1 \text{ keV}$, which could be modeled by either a blackbody or a series of emission lines. However given the differential variability between the depths of the OVII and OVIII edges seen on a timescale $\sim 10^4 \text{ s}$ during the 1994 observation, Guainazzi et al considered neither explanation to be satisfactory. We find no strong requirement for a low temperature blackbody component in our analysis of NGC 4051 (with our models for having $1.0 \lesssim \overline{R}_{0.6} \lesssim 1.2$). For our model including Compton-reflection we find $L_{bb} \lesssim 3 \times 10^{41} \text{ erg s}^{-1}$ for $kT = 0.1 \text{ keV}$. Instead our findings do imply significant emission from the photoionized gas in NGC 4051 at energies $\lesssim 1 \text{ keV}$ (with a luminosity of $\sim 10^{41} \text{ erg s}^{-1}$ in the 0.1-1 keV band), emission which was ascribed to the blackbody component by previous workers. However we do note that the derived intensity of this emission is up to a factor 3 times that expected given the intensity of the continuum during the observations. It is currently unclear whether these results indicate that the source was brighter in the past, that there is indeed an additional component at the softest energies, or the physical conditions with NGC 4051 are much more complex. We consider it unlikely that significant progress in decoupling the complex spectral variability exhibited by NGC 4051 $\lesssim 1 \text{ keV}$ will not be made until high signal-to-noise observations are performed with high spectral and temporal resolution. Nevertheless, the time-averaged results presented here are useful for comparison with those from those sources which appear to exhibit less dramatic variability.

NP94 found evidence for absorption by ionized gas in *Ginga* observations, with $N_{H,z} \sim 6 \times 10^{22} \text{ cm}^{-2}$.

NGC 4151:

This Seyfert 1.5 galaxy was first detected in X-rays by *UHURU* (Giacconi et al 1974), and has been extensively studied ever since at all wavebands. Interestingly, despite being one of the brightest Seyfert 1 galaxies in the X-ray band, the source appears to be somewhat atypical (e.g see Warwick et al 1996 and references therein). Specifically, it has long been known that NGC 4151 appears to have a flat powerlaw ($\Gamma \sim 1.3\text{--}1.7$), a substantial column density of absorbing gas intrinsic to the source ($N_{H,z} \sim 10^{22}\text{--}10^{23} \text{ cm}^{-2}$) and a strong 'soft-excess' at energies $\lesssim 2 \text{ keV}$. At present, the consensus is that the usually hard underlying continuum is the result of different physical conditions associated with the emission mechanism compared to most other objects in its class (but see Zdziarski, Johnson & Magdziarz 1996). The soft-excess has been interpreted as either due to separate emission component (e.g. Warwick, Done & Smith 1995) and/or the result of the absorbing gas only partially covering the source (e.g. Holt et al 1980). The suggestion that the absorbing gas in NGC 4151 might be photoionized was first made by Yaqoob, Warwick & Pounds (1989). However subsequent observations, in particular the different variability characteristics

observed below and above ~ 1 keV, have suggested the situation may be more complex (e.g. Weaver et al 1994a,b; Warwick et al 1996). *Einstein* HRI (Elvis, Briel & Henry 1983) and *ROSAT* HRI (Morse et al 1995) observations have shown spatially resolved X-ray emission, probably associated with the extended narrow-line region, at an intensity likely to also contribute to the observed spectrum $\lesssim 1$ keV.

In our analysis of the data from 6 *ASCA* observations carried out prior to 1994 May, we found 3 datasets fulfilling the criteria defining this 'sample' (see also Paper I). As summarized in Table 12, we find that a fit satisfying our criteria for acceptability is achieved for the first two observations (NGC 4151(2,4)) only when the absorbing material is allowed to be ionized *and* $\sim 5\%$ of the underlying continuum is allowed to escape without suffering any attenuation (i.e. models *B(ii)* & *C(ii)*). Such an hypothesis is strongly supported by the third observation (NGC 4151(5)), even though none of the models in §5 provide a solution which formally satisfies our criteria for acceptability (see Fig. 9). In §6.4.3 we found evidence in all 3 datasets for additional emission due to an optically-thin plasma at a temperature and intensity consistent with the extended emission. In all cases we find best-fitting values of $\Gamma \sim 1.5$, $U_X \sim 0.07$, $N_{H,z} \sim 4\text{--}7 \times 10^{22} \text{ cm}^{-2}$, and $L_X \sim 1.4\text{--}2.0 \times 10^{43} \text{ erg s}^{-1}$. However, as described in §7.2, the ionized gas appears to respond in an interesting way in response to changes in the intensity of the illuminating continuum between observations. A possible explanation of such behaviour was proposed in which the gas responsible for the absorption is clumped into regions of differing $N_{H,z}$ with a characteristic scale-size greater than that for the central source. It was shown that Keplerian motion would allow such $N_{H,z}$ perturbations to traverse the cylinder-of-sight on a timescale consistent with observations for reasonable range of radii, giving rise to an apparent decoupling between variations in U_X , $N_{H,z}$ and the intensity of the underlying source.

These NGC 4151 datasets have been independently analysed by other workers. Weaver et al (1994b) considered the 4151(2) dataset and found a satisfactory fits with $\Gamma \sim 1.6$, $U \sim 0.3$ (for an unspecified XUV spectrum), $N_{H,z} \sim 5 \times 10^{22} \text{ cm}^{-2}$, $D_f \sim 0.03$. However when a similar model was applied to the 4151(1) dataset, these workers found U (and $N_{H,z}$) to be *higher* when the source was fainter. (We confirm this general behaviour, finding $\Gamma \sim 1.4$, $U_X \sim 0.13$, $N_{H,z} \sim 10^{23} \text{ cm}^{-2}$, $D_f \sim 0.09$, $\Omega/4\pi \sim 4$ and $L_X \sim 0.9 \times 10^{43} \text{ erg s}^{-1}$ when model *C(ii)* is applied to the 4151(1) dataset.) Weaver et al also suggested an explanation is terms of inhomogeneities in the ionized material trasversing the cylinder-of-sight.

Zdziarski, Johnson & Magdziarz (1996) have considered the 4151(1) *ASCA* dataset along with contemporaneous *CGRO* OSSE data. They find the spectra $\gtrsim 3$ keV to be

better described by thermal Comptonization, and dual, cold absorber (with twice cosmic abundance of Fe), rather than by an ionized absorber. Furthermore, they show that if a Compton-reflection component is added, the underlying spectral index of this source is steepened to $\Gamma \sim 1.8$ and hence similar to that observed in other Seyfert 1 galaxies. However, since we have not included 4151(1) in our general analysis we feel unable to comment further on this result here (although see above, and also note that in §6.4.1 we did not find a significant improvement when Compton-reflection was included in our analysis of the NGC 4151(2,4,5) datasets). Nevertheless, we note Zdziarski, Johnson & Magdziarz also consider several archival X- and γ -ray datasets, and make a number of points concerning the emission mechanism in this source.

Warwick et al (1996) considered the 4151(4,5) datasets (as well as 4151(3,6), and psuedo-simultaneous *ROSAT* PSPC and *CGRO* OSSE observations). They confirmed previous findings that the time-variability patterns differ in the soft and hard X-ray bands, with the *ROSAT* PSPC count rate in the 0.1–1 keV band remaining constant at ~ 0.46 count s^{-1} whilst the 1–2 keV count rate increased a factor ~ 2 (to ~ 0.32 count s^{-1}) on a timescale ~ 2 days (around the time of the NGC 4151(3) *ASCA* observation). Unfortunately the *ROSAT* observations ended ~ 2 days later (and at the time of the 4151(4) *ASCA* observation), but the subsequent *ASCA* observations showed that 1–10 keV count rate remained relatively constant ($\lesssim 30\%$ variability) for a period of ~ 6 days thereafter. We do not attempt a detailed comparison of our results with these findings here. However we note that our best-fitting model to the 4151(4) dataset does predict a count rate in the 1.0–2.0 keV band of the *ROSAT* PSPC of 0.30 count s^{-1} , consistent with that observed. The corresponding count rate prediction for the 0.1–1.0 keV is clearly a strong function of the spectrum assumed < 0.6 keV especially the value assumed for $N_{H,0}$. This band is clearly poorly constrained with *ASCA* which results in a range of predicted PSPC count rates ~ 0.2 – 0.8 count s^{-1} at this epoch, but which encompasses that observed.

In §6.4.3 we suggested that the spectrum in $\lesssim 1$ keV was composed of a fraction $D_f \sim 5\%$ of the underlying continuum which is allowed to escape without suffering any attenuation, the emission spectrum of the photoionized ionized gas and thermal emission from an optically-thin plasma. At energies $\gtrsim 1.5$ keV, the observed spectrum becomes increasingly dominated by the underlying continuum transmitted by the ionized absorber (e.g. Fig. 9). The emission from the optically-thin plasma, identified with the extended emission observed in the source, is assumed to be constant with time and under the above assumptions is of relatively minor importance to the observed flux (corresponding to a count rate in the 0.1–1 keV band of the *ROSAT* PSPC of 10^{-3} – 0.15 count s^{-1}). The variability timescales for remaining spectral components differ, with that for the transmitted continuum determined by the variability timescale of the central source and/or the

timescale over which significant changes in the absorbing column density occur within the cylinder-of-sight (above). The timescales on which variations in the intensity of the scattered continuum and emission from the photoionized gas occur are determined by the light travel-times to the corresponding regions. If we assume that the rise in the 1–2 keV count rate observed by *ROSAT* is due to a brightening in the central source, then the lack of a corresponding increase < 1 keV seen in NGC 4151(4,5) implies these regions lie $\gtrsim 4$ light-days. However if the rise seen by *ROSAT* is simply the result of a change in the absorbing column, then no such constraints can be placed on the location of these regions.

We note that Weaver et al (1994a) presented the results of a *BBXRT* observation of NGC 4151, and considered a model similar to our model $C(ii)$ (but with $\Omega = 4\pi$). They found (see Weaver et al §4.3) $\Gamma \sim 1.5$, $N_{H,z} \sim 10^{23} \text{ cm}^{-2}$, $D_f \sim 0.04$ (from their Fig.14), and $U_X \sim 10^{-2}$ for their 'high-state' dataset, decreasing by a factor ~ 2 during the 'low-state' 1 day later.

NGC 4151 has long been known to exhibit variable absorption features in UV (e.g. Penston et al 1981). However the wide range of ionization states observed, including both low (Lyman series, CIII) and high (NV, OVI) ionization UV lines, exclude a single-zone photoionization model accounting for the absorption in both the UV and X-ray bands (Kriss et al 1995).

Mrk 766:

This Seyfert 1.5 galaxy was first detected in X-rays by *Einstein* (Kriss, Canizares & Ricker 1980) and has since been revealed to be one of the most highly variable AGN (e.g. Ghosh & Soundararajaperumal 1992b). In our analysis of the data from *ASCA* observation performed in 1993 December, we found Mrk 766 to be second most variable source in our sample, with evidence that the amplitude was larger at $\lesssim 2$ keV (Paper I). Leighly et al (1996b) have presented a more detailed analysis of this dataset and came to the same conclusion, finding the amplitude of the variability to be highest at ~ 1 keV. They suggest this is due to the intensity of a soft component decreasing slightly whilst the intensity and steepness of the underlying continuum $\gtrsim 1$ keV intensity increased (from $\Gamma \sim 1.6$ to $\Gamma \sim 2.0$). A similar change in the form of the continuum with flux state was previously suggested on the basis of *ROSAT* PSPC results for this source (Molendi & Maccacaro 1994; Netzer, Turner & George 1994).

From the analysis of the mean spectrum presented here, we find model $A(i)$ to provide an unsatisfactory description of the spectra. Fits satisfying our criteria for acceptability are obtained if $\sim 50\%$ of the continuum escapes without suffering attenuation by neutral material (model $A(ii)$). However yet superior fits are obtained if the absorbing gas is assumed to be ionized (model $B(ii)$) giving $\Gamma \sim 2$, $U_X \simeq 0.1$, $N_{H,z} \sim 1.6 \times 10^{22} \text{ cm}^{-2}$ and

$D_f \sim 0.5$. We note that such a model requires no additional soft component (eg. Fig 9). Indeed, we find models $C(i)$ & $C(ii)$ to offer only small improvements in the goodness-of-fit and thus find no compelling evidence for significant emission from the ionized gas. In no case is there a requirement for any additional absorption by neutral gas in excess of $N_{H,0}^{gal}$. It should be noted however, that that models $B(i)$ – $C(ii)$ all have $P(\chi^2 | dof) < 0.05$.

Leighly et al also report the presence of an absorption feature, identified with OVII, and presented the results of photoionization calculations assuming a model similar to our model $B(i)$. They find a best-fitting column density $N_{H,z} \sim 6 \times 10^{21} \text{ cm}^{-2}$, in agreement with our findings (Table 5). Unfortunately Leighly et al do not specify the limits on their assumed continuum, thus we are unable to compare their values to U_X directly, however they do find an increase in ionization parameter with intensity.

NGC 4593:

This Seyfert 1.0 galaxy was first detected in X-rays by *UHURU* (Forman et al 1978). In our analysis of the data from *ASCA* observation performed in 1994 January, we find model $A(i)$ provides a satisfactory description of the data analysed, but fails our criteria for extrapolation $< 0.6 \text{ keV}$. Fits satisfying our criteria for acceptability are obtained if $\sim 70\%$ of the continuum escapes without suffering attenuation by neutral material (model $A(ii)$). However yet superior fits are obtained if the absorbing gas is assumed to cover the entire source and is ionized (model $B(i)$), giving $\Gamma \sim 2$, $U_X \simeq 0.1$, $N_{H,z} \sim 2 \times 10^{21} \text{ cm}^{-2}$. This confirms the findings of R97 who found the addition of OVII and OVIII edges ($\tau_{O7} \sim 0.3$ & $\tau_{O8} \sim 0.1$) significantly improved the fit to a single powerlaw model ($\Gamma \sim 2$) to these *ASCA* data. R97 also fitted a single-zone photoionization model and found $U_X^{R97} \sim 0.05$, $N_{H,z} \sim 3 \times 10^{21} \text{ cm}^{-2}$, $\Gamma \sim 1.9$.

We find that statistically there is no strong requirement for any of the underlying continuum to escape without suffering attenuation by the ionized material, or for any significant emission from the ionized gas, (models $B(ii)$ – $C(ii)$). In all cases there is no required for any additional absorption by neutral gas in excess of $N_{H,0}^{gal}$. We note that a substantially flatter spectral index has been suggested in the past (eg. $\Gamma \sim 1.1$, T91).

MCG-6-30-15:

This Seyfert 1.0 galaxy was first detected in X-rays by *HEAO-1* A-2 (Marshall et al. 1979). Absorption due to ionized gas first suggested by *Ginga* observations, with $N_{H,z} \sim 10^{23} \text{ cm}^{-2}$ (Nandra, Pounds & Stewart 1990). Our analysis of the data from two *ASCA* observations separated by ~ 3 weeks in 1993 July, we confirm the presence of ionized gas. However whilst none of the models presented in §5 provide a fit which formally satisfies our criteria for MCG-6-30-15(1), this is primarily due to the presence of a deficit at $\sim 1 \text{ keV}$ (Fig.6). An acceptable solution is obtained for MCG-6-30-15(2) for model $C(i)$, but again some

evidence for a relatively small deficit at ~ 1 keV (Fig.10).

However, as further discussed in §7.3 there is a significant increase in column density (from $N_{H,z} \sim 6 \times 10^{21} \text{ cm}^{-2}$ to $\sim 9 \times 10^{21} \text{ cm}^{-2}$), along with a slight *increase* in ionization parameter (from $U_X \sim 0.11$ to ~ 0.15) despite a factor ~ 2 *decrease* in the intensity of the illuminating continuum between the 2 observations (e.g. Fig 16). This, the presence of the ~ 1 keV deficit, and a decrease in the depth of the OVIII edge on a timescale $\sim 10^4$ s (but not in the depth of the OVII edge) observed in an *ASCA* observation performed in 1994 July (Otani et al 1996) are impossible to reconcile with that expected from a uniform shell of gas reacting to changes in the intensity of the photoionizing continuum.

A single-zone photoionization models have also been applied to these data by Fabian et al (1994) and Reynolds et al (1995), assuming an ionizing continuum consisting of a single powerlaw of $\Gamma = 2$. Using Fig 1b to convert from their quoted values of ξ we obtain results in good agreement with those found here ($N_{H,z} \sim 6 \times 10^{21} \text{ cm}^{-2}$, $U_X \sim 0.09$ and $N_{H,z} \sim 13 \times 10^{21} \text{ cm}^{-2}$, $U_X \sim 0.11$ for the MCG-6-30-15(1,2) datasets respectively). Photoionization models for the extended (4 day) *ASCA* observation carried out in 1994 July have been presented by Otani et al (1996) and R97. The source exhibited a factor ~ 4 variability in the observed flux during this observation (covering the two flux states represented by MCG-6-30-15(1,2)) leading Otani et al to divide the observation into 2 parts. They found $N_{H,z} \sim 5 \times 10^{21} \text{ cm}^{-2}$, $U_X \sim 0.04$ for the first 300 ks of the observation, but $N_{H,z} \sim 10 \times 10^{21} \text{ cm}^{-2}$, $U_X \sim 0.18$ for the last 60 ks. For reference, R97 analysed the time-averaged spectrum and obtained $U_X^{R97} \simeq 0.05$ and $N_{H,z} \sim 6 \times 10^{21} \text{ cm}^{-2}$) The physical implications of these results have been further explored by Reynolds & Fabian (1995).

Curiously (but see Reynolds & Fabian 1995) MCG-6-30-15 appears to be heavily reddened in the optical/UV thus little is known regarding the presence of UV absorption features.

IC 4329A:

This Seyfert 1.0 galaxy was first detected in X-rays by *Ariel-V* (Elvis et al 1978). In our analysis of the data from *ASCA* observation performed in 1993 August, we find no model in §5 which satisfies our formal criteria for acceptability. However we do find a significant improvement in the fits for models including ionized gas, with $U_X \sim 0.02$ – 0.04 , $N_{H,z} \sim 2 \times 10^{21} \text{ cm}^{-2}$ and $\Gamma \sim 1.9$ for all models $B(i)$ – $C(ii)$. A substantial column density of neutral gas is also required for this source $N_{H,0} \sim 4 \times 10^{21} \text{ cm}^{-2}$, far in excess of $N_{H,0}^{gal}$, but consistent with previous findings and the edge-on orientation of the host galaxy. Cappi et al (1996) and R97 have both performed independent analyses of this *ASCA* dataset. Both find the addition of two edges to a single powerlaw model ($\Gamma \sim 1.9$) significantly improved the goodness-of-fit over the 0.6–1.0 keV band. R97 fixed the edge energies to those appropriate

for OVII and OVIII and found $\tau_{O7} \sim 0.6$ and $\tau_{O8} \sim 0.1$. Cappi et al allowed the line energies to be free and obtained a different ratio of optical depths, but otherwise similar results. Both Cappi et al and R97 also fitted the data with a similar photoionization model and obtained $\xi \sim 10$ ($\equiv U_X^{R97} \sim 0.02$), $N_{H,z} \sim 3 \times 10^{21} \text{ cm}^{-2}$ and $N_{H,0} \sim 3 \times 10^{21} \text{ cm}^{-2}$. These results are consistent with those found in a *ROSAT* PSPC observation (Madejski et al 1995).

We also found evidence for a strong Compton-reflection component in this source with $\mathcal{F} \sim 4$ (§6.4.1), similar to that found by Cappi et al. This hard tail was also found in *HEAO-1* (W95) and *Ginga* (Miyoshi et al 1988; Piro, Yamauchi & Matsuoka 1990) observations, and offers an explanation the *CGRO* OSSE spectrum of this source (Madejski et al 1995).

None of the models quoted by Cappi et al (1996) and R97 formally satisfy our criteria for acceptability (though some of the fits described by Cappi et al are considered acceptable to those workers). It consider it likely that the poverty of the various fits to the *ASCA* data are a combination of unaccounted for systematics errors in the calibration and additional spectral complexity in the soft X-ray band. As can be seen from Table 10, even we applied the Compton-reflection fit, an excess of counts remains < 0.6 keV. A similar effect was reported by Cappi et al. This may be the result of a real steepening of the intrinsic emission from IC 4329A, or the result of contamination of the *ASCA* data by emission from the nearby elliptical galaxy, IC 4329 (see Madejski et al 1995).

NP94 found evidence for absorption by ionized gas in *Ginga* observations, with $N_{H,z} \sim 10^{22} \text{ cm}^{-2}$.

NGC 5548:

This Seyfert 1.2 galaxy was first detected in X-rays by *OSO-7* (Hayes et al 1980). Absorption by ionized gas in NGC 5548 was first suggested by *Ginga* observations (Nandra et al 1991) and confirmed by the *ROSAT* PSPC (Nandra et al 1993). In our analysis of the data from *ASCA* observation performed in 1993 July, we find acceptable solutions with $U_X \sim 0.1$, $N_{H,z} \sim 3 \times 10^{21} \text{ cm}^{-2}$ and $\Gamma \sim 1.9$ for all models $B(i)$ & $C(i)$. Consistent results are also obtained for model $B(ii)$, with no requirement for an unattenuated ($D_f = 0$). This confirms the results of R97 who found the addition of OVII and OVIII edges ($\tau_{O7} \sim 0.25$ & $\tau_{O8} \sim 0.16$) significantly improved their fit to a single powerlaw model ($\Gamma \sim 1.9$) to these *ASCA* data. R97 also fitted a single-zone photoionization model and found $U_X^{R97} \sim 0.08$, $N_{H,z} \sim 5 \times 10^{21} \text{ cm}^{-2}$, assuming a single optical–X-ray continuum $\Gamma \sim 1.9$. Mathur, Elvis & Wilkes (1995) have also presented photoionization calculations based on previously published *ASCA* results and obtain $U_X \sim 0.06$ (for their quoted optical–X-ray continuum) assuming $N_{H,z} \sim 4 \times 10^{21} \text{ cm}^{-2}$.

We find a significant improvement in the goodness-of-fit is achieved assuming model $C(ii)$. However the best-fitting solution occupies the region of high- $N_{H,z}$, high- U_X , high- D_f parameter-space and does not extrapolate well < 0.6 keV (Fig 12). A yet superior improvement was found in §6.4.2 consisting of the combination of a steep powerlaw ($\Gamma_s \sim 3.2$) dominating the lowest energies and a flatter powerlaw ($\Gamma_h \sim 1.5$) dominating at highest energies. The ionized gas in this case has $U_X \sim 0.2$, $N_{H,z} \sim 7 \times 10^{21} \text{ cm}^{-2}$ but also requires a neutral column density ($N_{H,0} \sim 1.7 \times 10^{21} \text{ cm}^{-2}$) far in excess of $N_{H,0}^{gal}$.

A spectral flattening towards higher energies also seen in *HEAO-1* (W95) and *Ginga* (NP94) along with evidence for absorption by ionized gas, with $N_{H,z} \sim 5 \times 10^{22} \text{ cm}^{-2}$. A 'soft excess' has been proposed in NGC 5548 from the analysis of *EXOSAT* (TP89) and *ROSAT* (Nandra et al 1993; Done et al 1995) datasets, but we find any such component to be insignificant > 0.6 keV from the analysis presented here.

NGC 5548 has been observed to have variable absorption lines of C IV, N V and Ly α in the UV (Shull & Sachs 1993; Mathur, Elvis & Wilkes 1995). A detailed comparison between the UV and X-ray absorption systems indicates the same gas is probably responsible (Mathur, Elvis & Wilkes 1995).

Mrk 841:

This Seyfert 1.5 galaxy was first detected in X-rays by *Einstein* (Tananbaum et al 1986) and has since been observed to exhibit dramatic spectral variability (eg. George et al 1993 and references therein). In our analysis of the data from two *ASCA* observations performed in 1993 August and 1994 February, we find model evidence for ionized gas in Mrk 841(1), with model $B(i)$ offering an acceptable description of the data with $\Gamma \sim 1.9$, $U_X \sim 0.16$, $N_{H,z} \sim 3 \times 10^{21} \text{ cm}^{-2}$. However the features are relatively weak (Fig 6) and not required by the Mrk 841(2) dataset, presumably due to its lower signal-to-noise ratio. A superior fit is obtained for Mrk 841(2) assuming model $B(ii)$. However the solution occupies the region of high- $N_{H,z}$, high- U_X , high- D_f parameter-space and the parameters are poorly constrained, primarily since any derivations from a single powerlaw are rather subtle (e.g. Fig 9). R97 also found a lack of evidence for OVII and OVIII absorption edges in their analysis of the *ASCA* data from Mrk 841(2). Interestingly, all models suggest the underlying continuum was flatter during Mrk 841(2) (typically $\Gamma \sim 1.6$ – 1.7) although the observed fluxes in the 2–10 keV band were similar ($F_{2-10} \sim 1.2$ and $1.1 \times 10^{-11} \text{ erg cm}^{-2} \text{ s}^{-1}$ respectively).

No significant improvement in the goodness-of-fit are obtained for models $C(i)$ & $C(ii)$ with the high values for the intensity of the ionized emitter derived in these cases ($\Omega/4\pi \sim 50$) most likely being an artifact of a separate soft component. The existence of a separate soft component has been suggested by some (but not all) previous observations (e.g. see George et al 1993). Most recently, the spectrum from an extended *ROSAT* PSPC

observation of Mrk 841, performed over a ~ 6 day period in 1992 can be well described by a powerlaw with $\Gamma \sim 2.2$ (i.e. steeper than that found here) along with a $kT \sim 0.08$ keV blackbody (Nandra et al 1995). However the data were equally well described by a yet steeper powerlaw ($\Gamma \sim 2.4$) and a photoionized absorber with $N_{H,z} \sim 2 \times 10^{21} \text{ cm}^{-2}$ $U_X \sim 0.04$ (assuming a powerlaw optical–X-ray continuum). Unfortunately, as described in §7.4, given the signal-to-noise ratio of all the datasets and the dramatic spectral variability exhibited by the source, a further interpretation of these results is somewhat problematic. However we do note that the extrapolation of the underlying powerlaw implied by the PSPC spectrum does agree remarkably well with the UV data, implying the luminosity of the component dominating the 13.6–100 eV band may have been grossly overestimated in the past (e.g. see fig 3 of Nandra et al 1995).

NGC 6814:

In the early 1990s, NGC 6814 had its 15 months of fame due to the apparent detection of a periodicity in its X-ray lightcurve (Mittaz & Branduardi-Raymont 1989; Done et al 1992) spawning a frenzy of theoretical activity. However, subsequent observations by the *ROSAT* PSPC revealed the periodicity to be the result of strong contamination by a Galactic source within the field-of-view of previous instruments (Madejski et al 1993). It now appears that the X-ray emission from this Seyfert 1.2 galaxy is relatively weak. *ASCA* observed NGC 6814 on 3 occasions prior to 1994 May, but only one dataset (NGC 6814(1)) met the criteria for inclusion in our sample (Paper I). The count rate for this observation, performed in 1993 May, is a factor ten lower than any of the other sources in our sample. Given the signal-to-noise ratio, it is perhaps not surprising that we find the dataset to be consistent with a simple powerlaw ($\Gamma \sim 1.7$) absorbed by $N_{H,0}^{gal}$. R97 also found a lack of evidence for OVII and OVIII absorption edges in their analysis of this dataset.

Mrk 509:

This Seyfert 1.2 galaxy was first detected in X-rays by *Ariel-V* (Cooke et al 1978). In our analysis of the data from an *ASCA* observation performed in 1994 April, we find a simple powerlaw (model $A(i)$ with $\Gamma \sim 1.9$) provides a reasonable description of the data (§5.1). Whilst a significant improvement in the goodness-of-fit is achieved assuming model $A(ii)$, $\sim 80\%$ of the continuum is unattenuated giving rise to a relatively subtle change in the spectrum $\lesssim 1$ keV (Fig 4). A further, significant improvement in the goodness-of-fit is obtained for model $B(i)$, with $\Gamma \sim 2.0$, $U_X \sim 10^{-2}$, $N_{H,z} \sim 8 \times 10^{20} \text{ cm}^{-2}$, but again the features imprinted on the continuum are relatively weak (Fig 6). This confirms the results of R97 who found the addition of shallow OVII and OVIII edges ($\tau_{O7} \sim 0.11$ & $\tau_{O8} \sim 0.04$) significantly improved their fit to a single powerlaw model ($\Gamma \sim 2$) to these *ASCA* data. R97 also fitted a single-zone photoionization model and found $U_X^{R97} \sim 0.1$, $N_{H,z} \sim 3 \times 10^{21} \text{ cm}^{-2}$, the discrepancy with our results possibly arising as a result of their

flatter continuum ($\Gamma \sim 1.9$).

No significant improvement in the goodness-of-fit are obtained assuming the subsequent models in §5, despite the suggestion of line-like soft-excess by *Einstein* (T91) and *EXOSAT* (Morini, Lipani, Molteni 1987) observations. However a significant improvement is achieved if a moderate ($1 \lesssim \mathcal{F} \lesssim 5$) Compton-reflection component is included (§6.4.1). Such a component is also suggested by *HEAO-1* (W95) and *Ginga* (NP94) observations of the source and its inclusion steepens slightly the underlying powerlaw ($\Delta\Gamma \sim 0.2$) and gives rise to a larger ionized column density ($N_{H,z} \sim 2 \times 10^{21} \text{ cm}^{-2}$) whilst leaving U_X as for model $B(i)$.

NGC 7469:

This Seyfert 1.2 galaxy was first detected in X-rays by *UHURU* (Forman et al 1978), and observed by *ASCA* on 3 occasions over a period of ~ 9 days in 1993 November. However, only one observation (NGC 7469(2)) met the criteria for inclusion in our sample (Paper I). We find a simple powerlaw (model $A(i)$ with $\Gamma \sim 2.0$) provides an acceptable description of the spectrum. However there is evidence for some spectral curvature, leading to a significant improvement in the goodness-of-fit for models $A(ii)$, $B(ii)$ and $C(ii)$ if the bulk of continuum is unattenuated ($D_f \gtrsim 0.6$) whilst the remainder is absorbed by a large column density ($N_{H,z} \gtrsim \text{few} \times 10^{23} \text{ cm}^{-2}$), or if there is a strong ($\mathcal{F} \sim 7$) Compton-reflection component (§6.4.1).

Guainazzi et al (1994) have presented a combined analysis of the NGC 7469(1,2) datasets. They found a $\sim 40\%$ decrease in intensity between the two epochs, with some evidence for a steeper spectrum in the soft X-ray band ($\lesssim 0.8 \text{ keV}$) when the source is brighter. No such spectral variability was seen $\gtrsim 2 \text{ keV}$, with both epochs consistent with a powerlaw with $\Gamma \sim 1.9$. We see no reliable evidence for a soft-excess in our analysis of the NGC 7469(2) dataset, however we note that the results of Guainazzi et al (their Fig. 3) indicate such a component would be almost indistinguishable at that epoch. Spectral complexity in NGC 7469 $\lesssim 1 \text{ keV}$ has been suggested by previous *Einstein*, *EXOSAT* and *ROSAT* observations although its form remains illusive (e.g. Brandt et al 1993; Leighly et al 1996a and references therein). We note some soft flux is provided in our models which include emission but generally this is small (except in the case of our model including a Compton-reflection component).

In their analysis of the mean spectra from the NGC 7469(1,2) datasets, Guainazzi et al find the putative soft-excess to be consistent with a blackbody with $kT \sim 0.08 \text{ keV}$. Guainazzi et al find no evidence for OVII and/or OVIII absorption edges, whilst R97 find the addition of an OVII edge (of optical depth $\tau_{OV} \sim 0.2$) significantly improved the fit to a single powerlaw model ($\Gamma \sim 2.1$) to the NGC 7469(1) dataset.

In §6.4.1 we found that a strong Compton-reflection component is allowed by the data. Such a result is also obtained from previous *HEAO-1* (W95) and *Ginga* (NP94; Leighly et al 1996a) observations.

Finally we note that NGC 7469 has recently been the subject of an intense monitoring campaign in the optical, UV and X-ray bands. Most interestingly, preliminary results from the *RossixTE* observations reveal the X-rays to have exhibited large-amplitude variability apparently uncorrelated with the variations seen in the UV and optical (Nandra et al 1997d).

MCG-2-58-22:

This Seyfert 1.2 galaxy was first detected in X-rays by *Ariel-V* (Cooke et al 1978). In our analysis of the data from an *ASCA* observation performed in 1993 May, we find a simple powerlaw (model *A(i)* with $\Gamma \sim 1.7$) provides a reasonable description of the spectrum (§5.1). A similar result was obtained by Weaver et al (1995) from an independent analysis of these data, who suggested the source to be a 'bare' Seyfert 1 continuum with weak (if any) additional absorption or emission features. These workers also noted that the continuum was relatively flat compared to the canonical $\Gamma \simeq 1.9\text{--}2.0$ for most Seyfert 1 galaxies popularized by the *Ginga* results of NP94. However, as shown in §5, we do find significantly better fits when the more complex models are assumed, and in some cases obtain a derived index $\Gamma \sim 1.9$ (e.g. models *B(ii)* & *C(ii)*). Some of these models obviously contain ionized gas, but the constraints of U_X and $N_{H,z}$ are poor. We note that previous *Einstein* (T91), *EXOSAT* (Ghosh & Soundararajaperumal 1992a) and *ROSAT* PSPC (Turner, George & Mushotzky 1993) observations of MCG-2-58-22 have shown evidence for additional emission (features) $\lesssim 1$ keV.

In §6.4.1 we found a solution including Compton-reflection, but its strength is poorly constrained ($\mathcal{F} \sim 2\text{--}40$), and all but the lower values difficult to reconcile with the observed equivalent width of the Fe fluorescent line. However, we note that NP94 found no evidence for a Compton-reflection component in the *Ginga* data ($\mathcal{F} \sim 0.1$), but did find evidence for absorption by ionized gas in *Ginga* observations, with $N_{H,z} \sim 10^{23}$ cm⁻².

REFERENCES

- Anders, E., Grevesse, N., 1989, *Geochimica et Cosmochimica Acta* 53, 197
- Arnaud, K.A., et al., 1985, *MNRAS*, 217, 105
- Arnaud, K.A., 1996, *Astronomical Data Analysis Software and Systems V* eds Jacoby, G., Barnes, J, p17, ASP Conf. Series vol 101.
- Boller, Th., Meurs, E.J.A., Brinkmann, W., Fink, H.H., Zimmermann, U., Adorf, H.-M., 1992, *A&A*, 261, 57
- Bromage, G.E., et al., 1985, *MNRAS*, 215, 1
- Brandt, W.N., Fabian, A.C., Nandra, K., Tsuruta, S., 1993, *MNRAS*, 265, 996
- Brandt, W.N., Fabian, A.C., Pounds, K.A., 1996, *MNRAS*, 278, 326
- Burke, B.E., Mountain, R.W., Daniels, P.J., Dolat, V.S., 1994, *IEEE Trans. Nuc. SCI.* 41, 375
- Cappi, M., Mihara, T., Matsuoka, M., Hayashida, K., Weaver, K.A., Otani, C., 1996, *ApJ*, 458, 149
- Cappi, M., Matsuoka, M., Comastri, A., Brinkman, W., Elvis, M., Palumbo, G.G.C., Vignali, C., 1997, *ApJ*, 478, 492
- Cooke, B.A, Elvis, M., Ward, M.J., Fosbury, R.A.E., Penston, M.V., Maccacaro, T., 1976, *MNRAS*, 177, 121
- Cooke, B.A, et al, 1978, *MNRAS*, 182, 489
- Crenshaw, D.M., 1997, In *Emission Lines in Active Galaxies: New Methods and Techniques*, eds. Peterson, B.M, Cheng, F.-Z., Wilson, A.S. (ASP, San Fransisco), p.240
- Crenshaw, D.M., Maran, S.P., Mushotzky, R.F. 1997, in preparation
- Crenshaw, D.M., Bogges, A., Wu, C.-C., 1995, *AJ*, 110, 1026
- Courvoisier, T.J.-L., Paltani, S., 1992, *IUE – ULDA Access Guide No. 4*, ESA SP 1153, (ESTEC, Noordwijk)
- De Zotti, G., Gaskell, C.M., 1985, *A&A*, 147, 1
- Dickey, J.M., Lockman, F.J., 1990, *ARA&A*, 28, 215
- Done, C., Madejski, G.M., Mushotzky, R.F., Turner, T.J., Koyama, K., Kunieda, H., 1992, *ApJ*, 400, 138
- Done, C., Pounds, K.A., Nandra, K., Fabian, A.C., 1995, *MNRAS*, 275, 417
- Dotani, T., et al., 1996, *ASCA News*, 4, 3

- Elvis, M., Maccacaro, T., Wilson, A.S., Ward, M.J., Penston, M.V., Fosbury, R.A.E., Perola, G.C., 1978, MNRAS, 183, 129
- Elvis, M., Briel, U.G., Henry, J.P., 1983, ApJ, 268, 105
- Elvis, M., Lockman, F. J., Wilkes, B., 1989, AJ, 97, 777
- Fabian, A.C., Rees, M.J., Stella, L., White, N.E., 1989, MNRAS, 238, 729
- Fabian, A.C., et al., 1994, PASJ, 46, 59
- Feldman, U., 1992, Physica Scripta 46, 202
- Fiore, F., Perola, G.C., Ramano, M., 1990, MNRAS, 243, 522
- Fiore, F., Elvis, M., Mathur, S., Wilkes, B.J., McDowell, J.C., 1993, ApJ, 415, 129
- Forman, W., Jones, C., Cominsky, L., Julien, P., Murray, S., Peters, G., Tananbaum, H., Giacconi, R., 1978, ApJS, 38, 357
- George, I.M., Fabian, A.C., 1991, MNRAS, 249, 352
- George, I.M., Nandra, K., Fabian, A.C., Done, C., Day, C.S.R., 1993, MNRAS, 260, 111
- George, I.M., Turner, T.J., Netzer, H., 1995, ApJ, 438, L67
- George, I.M., Nandra, K., Laor, A., Turner, T.J., Fiore, F., Netzer, H., Mushotzky, R.F., 1997a, ApJ, submitted
- George, I.M., et al. 1997b, ApJ, in preparation (3783)
- Ghosh, K.K., Soundararajaperumal, S., 1991, ApJ, 383, 574
- Ghosh, K.K., Soundararajaperumal, S., 1992a, ApJ, 398, 501
- Ghosh, K.K., Soundararajaperumal, S., 1992b, MNRAS, 259, 175
- Ghosh, K.K., Soundararajaperumal, S., Kalai Selvi, M., Sivarani, T., 1992, A&A, 255, 119
- Giacconi, R., Murray, S., Gursky, H., Kellogg, E., Schreier, E., Matilsky, T., Koch, D., Tananbaum, H., 1974, ApJS, 27, 37
- Giuricin, G., Mardirossian, F., Mezzetti, M., 1995, ApJ, 446, 550
- Guainazzi, M., Matsuoka, M., Piro, L., Mihara, T., Yamauchi, M., 1994, ApJ, 436, L35
- Guainazzi, M., Mihara, T., Otani, C., Matsuoka, M., 1996, PASJ, 48, 781
- Halpern, J.P., 1982, PhD Thesis, Havard Univ.
- Halpern, J.P., 1984, ApJ, 281, 90
- Hayes, M.J.C., Culhane, J.L., Blissett, R.J., Barr, P., Burnell, S.J.B., 1980, MNRAS, 193, P15

- Holt, S.S., Mushotzky, R.F., Boldt, E.A., Serlemitsos, P.J., Becker, R.H., Szymkowiak, A.E., White, N.E., 1980, *ApJ*, 241, L13
- Kolman, M., Halpern, J.P., Martin, C., Awaki, H., Koyama, K., 1993, *ApJ*, 403, 592
- Koratkar, A.P., et al., 1996, *ApJ*, 470, 378
- Korista, K.T., Voit, G.M., Morris, S.L., Weymann, R. J., 1993, *ApJS*, 88, 357
- Korista, K.T., et al., 1995, *ApJS*, 97, 285
- Kriss, G.A., Canizares, C.R., Ricker, G.R., 1980, *ApJ*, 242, 492
- Kriss, G.A., et al., 1992, *ApJ*, 392, 485
- Kriss, G.A. et al., 1996a, *ApJ*, 467, 629
- Kriss, G.A., Espey, B.R., Krolik, J.H., Zheng, W., Davidsen, A.F., 1996b, *ApJ*, 467, 622
- Krolik, J., Kriss, G., 1995, *ApJ*, 447, 512
- Kruper, J.S., Canizares, C., Urry, C.M., 1990, *ApJS*, 74, 347
- Laor, A., Draine, B.T., 1993, *ApJ*, 402, 441
- Lawrence, A., Watson, M.G., Pounds, K.A., Elvis, M., 1987, *Nature*, 325,
- Lee, M.G., Balick, B., Halpern, J.P., Heckman, T.M., 1988, *ApJ*, 331, 154
- Leighly, K.M., Kunieda, H., Awaki, H., Tsuruta, S., 1996a, *ApJ*, 463, 158
- Leighly, K.M., Mushotzky, R.F., Yaqoob, T., Kunieda, H., Edelson, R., 1996b, *ApJ*, 469, 147
- Lu, L., Savage, B.D., Sembach, K.R., 1994, *ApJ*, 426, 563
- McHardy, I.M, Green, A.R., Done, C., Puchnarewicz, E.M., Mason, K.O., Branduardi-Raymont, G., Jones, M.H., 1995, *MNRAS*, 273, 549
- Maccacaro, T., Garilli, B., Mereghetti, S., 1987, *AJ*, 93, 1484
- Maccacaro, T., et al., 1988, *ApJ*, 326, 680
- Madejski, G.M., Done, C., Turner, T.J., Mushotzky, R.F., Serlemitsos, P., Fiore, F., Sikora, M., Begelman, M.C., 1993, *Nature*, 365, 626
- Madejski, G.M., et al., 1995, *ApJ*, 438, 672
- Makishima, K., 1994, *Proc. New Horizon of X-ray Astronomy — First Results from ASCA*, ed. Makino, F., Ohashi, T., (Universal Academy Press, Tokyo, Japan), p.171
- Makishima, K., et al., 1996, *PASJ*, 48, 171
- Maran, S.P, Crenshaw, D.M., Mushotzky, R.F., Reichert, G.A., Carpenter, K.G., Smith, A.M., Hutchings, J.B., Weymann, R., 1996, *ApJ*, 465, 733

- Marshall, F.E., Boldt, E.A., Holt, S.S., Mushotzky, R.F., Rothschild, R.E., Serlemitsos, P.J., Pravdo, S.H., 1979, ApJS, 40, 657
- Marshall, F.E., Holt, S.S., Mushotzky, R.F. Becker, R.H., 1983, ApJ, 269, L31
- Mathews, W.G., Ferland, G.J., 1987, ApJ, 323, 456
- Mathur, S., 1994, ApJ, 431, L75
- Mathur, S., 1997, In Proc. of the workshop on Mass Ejection from AGN, in press
- Mathur, S., Wilkes, B., Elvis, M., Fiore, F., 1994, ApJ, 434, 493
- Mathur, S., Elvis, M., Wilkes, B., 1995, ApJ, 452, 230
- Mathur, S., Wilkes, B., Aldcroft, T., 1997, ApJ, in press
- Mihara, T., Matsuoka, M., Mushotzky, R.F., Kunieda, H., Otani, C., Miyamoto, S., Yamauchi, M., 1994, PASJ, 46, L137
- Mineo, T., Stewart, G.C., 1993, MNRAS, 262, 817
- Mittaz, J.P.D., Branduardi-Raymont, G., 1989, MNRAS, 238, 1029
- Miyoshi, S., et al., 1988, PASJ, 40, 127
- Molendi, S., Maccacaro, T., Schaeidt, S., 1993, A&A, 271, 18
- Molendi, S., Maccacaro, T., 1994, A&A, 291, 420
- Molendi, S., et al., 1997, in Proc. 2nd National Meeting on AGN: From micro- to mega-parsecs, in press
- Morini, M., et al. 1986, ApJ, 307, 486
- Morini, M., Lipani, N.A., Molteni, D., 1987, ApJ, 317, 145
- Morse, J.A., Wilson, A.S., Elvis, M., Weaver, K.A., 1995, ApJ, 439, 121
- Mushotzky, R.F., Fabian, A.C., Iwasawa, K., Kunieda, H., Matsuoka, M., Nandra, K., Tanaka, Y., 1995, MNRAS, 272, L9
- Murphy, E.M., Lockman, F.J., Laor, A., Elvis, M., 1996, ApJS, 105, 369
- Nandra, K., Pounds, K.A., 1992, Nature, 359, 215
- Nandra, K., Pounds, K.A., 1994, MNRAS, 268, 405 (NP94)
- Nandra, K., Pounds, K.A., Stewart, G.C., 1990, MNRAS, 242, 660
- Nandra, K., Pounds, K.A., Stewart, G.C., George, I.M, Hayashida, K., Makino, F., 1991, MNRAS, 248, 760
- Nandra, K., et al., 1993, MNRAS, 260, 504

- Nandra, K., Turner, T.J., George, I.M., Fabian, A.C., Shrader, C., Sun, W.-H., 1995, MNRAS, 273, 85
- Nandra, K., George, I.M., Mushotzky, R.F., Turner, T.J., Yaqoob, T., 1997a, ApJ, 476, 70 (Paper I)
- Nandra, K., George, I.M., Mushotzky, R.F., Turner, T.J., Yaqoob, T., 1997b, ApJ, 477, 602 (Paper II)
- Nandra, K., Mushotzky, R.F., Yaqoob, T., George, I.M., Turner, T.J., Yaqoob, T., 1997c, MNRAS, 284, L7
- Nandra, K., et al., 1997d, in preparation
- Nandra, K., et al., 1997e, in preparation
- Netzer, H., 1990, in *Active Galactic Nuclei*, eds. Blandford, R.D., Netzer, H., Woltjer, L., (Springer-Verlag, Berlin), p107
- Netzer, H., 1993, ApJ, 411, 594
- Netzer, H., 1996, ApJ, 473, 781
- Netzer, H., Laor, A., 1993, ApJ, 404, L51
- Netzer, H., Turner, T.J., George, I.M., 1994, ApJ, 435, 106
- Ohashi, T., et al., 1996, PASJ, 48, 157
- Orr, A., Molendi, S., Fiore, F., Grandi, P., Parmar, A., Owens, A., 1997, A&A, submitted
- Otani, C., et al., 1996, PASJ, 48, 211
- Pan, H.C., Stewart, G.C., Pounds, K.A., 1990, MNRAS, 242, 177
- Parmar, A., et al., 1997, in preparation
- Penston, M.V., et al., 1981, MNRAS, 196, 857
- Piro, L., Yamauchi, M., Matsuoka, M., 1990, ApJ, 260, L35
- Pounds, K.A., Nandra, K., Fink, H.H., Makino, F., 1994, MNRAS, 267, 193
- Pounds, K.A., Stanger, V.J., Turner, T.J., King, A.R., Czenry, B., 1987, MNRAS, 224, 443
- Ptak, A., Yaqoob, T., Serlemitsos, P.J., Mushotzky, R.F., Otani, C., 1994, ApJ, 436, L31
- Reichert, G.A., Mushotzky, R.F., Holt, S.S., Petre, R., 1985, ApJ, 296, 69
- Reichert, G.A., et al., 1994, ApJ, 425, 582
- Reynolds, C.S., Fabian, A.C., 1995, MNRAS, 273, 1167
- Reynolds, C.S., Fabian, A.C., Nandra, K., Inoue, H., Kunieda, H., Iwasawa, K., 1995, MNRAS, 277, 901

- Reynolds, C.S., 1997, MNRAS, 286, 513 (R97)
- Ricker, G.R., 1978, Nature, 271, 334
- Rush, B., Malkan, M., Fink, H.H., Voges, W., 1996, ApJ, 471, 190
- Schnopper, H.W., Epstein, A., Delvaile, J.P, Tucker, W., Doxsey, R., Jernigan, G., 1977, ApJ, 215, L7
- Serlemitsos, P.J., et al., 1995, PASJ, 47, 105
- Serlemitsos, P.J., Ptak, A., Yaqoob, T., 1996, in Proc. *The physics of LINERS in view of recent Observations*, eds. Eracleous, M., Koratkar, A., Leitherer, C., Ho, L., ASP Conf. Series, 103, p70
- Seyfert, C., 1943, ApJ, 07, 28
- Shields, J.C., Hamann, F., 1997, ApJ, in press
- Shull, J.M., Sachs, E.R., 1993, ApJ, 416, 536
- Stark, A.A., Gammie, C.F., Wilson, R.W., Bally, J., Linke, R.A., Heiles, C., Hurwitz, M., 1992, ApJS, 79, 77
- Tanaka, Y., Inoue, H., Holt, S.S., 1994, PASJ, 46, L37
- Tanaka, Y., et al., 1995, Nature, 375, 659
- Tananbaum, H., Peters, G., Forman, W., Giacconi, R., Jones, C., Avni, Y., 1978, ApJ, 223, 74
- Tananbaum, H., Avni, Y., Green, R.F., Schmidt, M., Zamorani, G., 1986, ApJ, 305, 57
- Turner, T.J., Pounds, K.A., 1988, MNRAS, 232, 463
- Turner, T.J., Pounds, K.A., 1989, MNRAS, 240, 833 (TP89)
- Turner, T.J., Weaver, K.A., Mushotzky, R.F., Holt, S.S., Madejski, G.M., 1991, ApJ, 381, 85 (T91)
- Turner, T.J., George, I.M., Mushotzky, R.F., 1993, ApJ, 412, 72
- Turner, T.J., Nandra, K, George, I.M., Fabian, A.C., Pounds, K.A. 1993a, ApJ, 419, 127
- Turner, T.J., et al 1993b, ApJ, 407, 556
- Turner, T.J., Netzer, H., George, I.M., 1996, ApJ, 463, 134
- Turner, T.J., George, I.M., Kallman, T., Yaqoob, T., Zycki, P.T., 1996, ApJ, 472, 571
- Turner, T.J., George, I.M., Nandra, K., Mushotzky, R.F., 1997a, ApJS, submitted
- Turner, T.J., George, I.M., Nandra, K., Mushotzky, R.F., 1997b, ApJ, submitted
- Turner, T.J., George, I.M., Nandra, K., Mushotzky, R.F., 1997b, ApJ, in preparation

- Ulrich, M.-H., 1988, MNRAS, 230, 121
- Veron-Cetty, M.-P, Veron, P., 1993, ESO Sci. Rep., 13, 1
- Walter, R., Fink, H.H., 1993, A&A, 274, 105
- Warwick, R.S., Done, C., Smith, D.A., 1995, MNRAS, 275, 1003
- Warwick, R.S., et al. 1996, ApJ, 470, 349
- Weaver, K.A., et al 1994a, ApJ, 423, 621
- Weaver, K.A., Yaqoob, T., Holt, S.S., Mushotzky, R.F., Matsuoka, M., Yamauchi., M., 1994b, ApJ, 436, L27
- Weaver, K. A., Arnaud, K.A., Mushotzky, R. F. 1995, ApJ, 447, 121 (W95)
- Weaver, K.A., Nousek, J., Yaqoob, T., Hatashida, K., Murakami, S., 1995, ApJ, 451, 147
- Whittle, M., 1992, ApJS, 79, 49
- Yaqoob, T., Warwick, R.S., 1991, MNRAS, 248, 773
- Yaqoob, T., Warwick, R.S., Pounds, K.A., 1989, MNRAS, 236, 153
- Zdziarski, A.A., Johnson, W.N., Magdziarz, P., 1996, MNRAS, 283, 193
- Zheng, W., et al., 1995a, ApJ, 444, 632
- Zheng, W., Kriss, G.A., Davidsen, A.F., Kruk, J.W., 1995b, ApJ, 454, L11

TABLE 1
THE SAMPLE

Name	z	a/b	$N_{H_0}^{gal}$ (10^{21} cm $^{-2}$)	$\langle f_{220} \rangle$ (mJy)	$(f_{125}/f_{220})_{obs}$	f_{2keV} (μ Jy)	α_{ro}	α_{ox}	$\log L_X$ (erg s $^{-1}$)	$\log L_{2-10}$ (erg s $^{-1}$)
Mrk 335	0.025	0.80	0.37	2.35 ± 0.94	3.55 ± 0.40	1.16 ± 0.06	-0.04	1.23	44.2	43.5
Fairall 9	0.046	0.80	0.32	4.64 ± 2.19	5.19 ± 1.14	2.37 ± 0.12	...	1.29	44.8	44.3
3C 120	0.033	0.76	1.23	0.31 ± 0.20	6.40 ± 3.44	5.29 ± 0.26	+0.72	0.69	44.9	44.4
NGC 3227	0.003	0.45	0.21	0.76 ± 0.08	0.19 ± 0.02	2.15 ± 0.11	+0.25	1.00	42.3	42.0
NGC 3516	0.009	0.75	0.29	1.49 ± 0.55	1.75 ± 0.45	7.49 ± 0.37	+0.13	0.90	43.8	43.4
NGC 3783	0.009	0.80	0.96	2.35 ± 1.00	3.30 ± 0.72	3.74 ± 0.19	+0.10	1.10	43.7	43.4
NGC 4051	0.002	0.68	0.13	1.46 ± 0.15	1.88 ± 0.19	2.67 ± 0.13	+0.22	1.07	42.7	41.6
NGC 4151	0.003	0.74	0.22	6.45 ± 2.97	2.21 ± 0.99	5.33 ± 0.93	+0.20	1.21	43.2	43.0
Mrk 766	0.012	...	0.18	2.26 ± 0.11	43.7	43.1
NGC 4593	0.009	0.78	0.20	1.20 ± 0.36	1.98 ± 0.52	3.93 ± 0.20	-0.02	0.98	43.5	43.1
MCG-6-30-15	0.008	0.58	0.41	0.56 ± 0.06	0.29 ± 0.03	4.70 ± 0.82	-0.01	0.81	43.6	43.1
IC 4329A	0.016	0.16	0.46	0.05 ± 0.02	...	7.45 ± 0.37	+0.44	0.32	44.3	43.9
NGC 5548	0.017	0.83	0.16	2.43 ± 0.71	3.25 ± 0.60	5.14 ± 0.26	+0.09	1.05	44.2	43.8
Mrk 841	0.036	...	0.22	1.14 ± 0.11	3.60 ± 0.36	1.21 ± 0.20	+0.07	1.17	44.2	43.8
NGC 6814	0.006	0.95	0.98	0.13 ± 0.01	41.6	41.3
Mrk 509	0.035	0.85	0.44	3.75 ± 0.85	3.29 ± 0.85	5.22 ± 0.26	-0.05	1.12	44.8	44.4
NGC 7469	0.017	0.58	0.48	2.62 ± 0.65	3.15 ± 0.48	3.27 ± 0.16	+0.21	1.05	44.2	43.7
MCG-2-58-22	0.047	0.67	0.35	1.55 ± 1.21	4.22 ± 1.07	1.36 ± 0.07	+0.08	1.20	44.6	44.2

NOTE.— Columns— (1) Source name; (2) redshift from Veron-Cetty & Veron (1993); (3) axial ratio from De Zotti & Gaskell (1985); (4) Galactic HI column density from the 21 cm measurements (from Murphy et al 1996; Dickey & Lockman 1990; Elvis, Lockman & Wilkes 1989; Stark et al 1992); (5) mean flux at 220 nm, $\langle f_{220} \rangle$ (from Courvoisier & Paltani 1992); (6) mean ratio of flux at 125 nm to that at 250 nm (from Courvoisier & Paltani 1992); (7) observed flux at 2 keV, f_{2keV} from the results presented in §5; (8) radio-to-optical spectral index α_{ro} ($= \log(f_{5GHz}/f_{220})/5.38$) using f_{5GHz} from Veron-Cetty & Veron (1993); (9) optical-to-X-ray spectral index α_{ox} ($= \log(f_{220}/f_{2keV})/2.548$); (10) luminosity, L_X , of the underlying continuum over the 0.1–10 keV band from the results presented in §5 (using $H_0 = 50$ km s $^{-1}$ Mpc $^{-1}$ and $q_0 = 0.5$); (11) corresponding luminosity, L_{2-10} , of the underlying continuum over the 2–10 keV band. All fluxes are measured at frequencies appropriate for the rest-frame of the source. For objects with more than one dataset presented here, f_{2keV} , L_X and L_{2-10} are exposure-weighted means. It should be remembered that the radio, UV and X-ray measurements are non-simultaneous.

TABLE 2
OBSERVATION LOG

Observation	Date	t_{exp} (SIS0) (10^3 s)	$Rate$ (SIS0) (count s^{-1})	N_{phot} (SIS0) (excl 5–7 keV)	N_{pts} (all)	$\Delta N_{0.6}$	F_{2-10} (10^{-12} erg cm^{-2} s^{-1})	References
Mrk 335	1993 Dec 09	19.3	0.528 ± 0.005	9837	650	14	9.5 ± 0.5	Re97
Fairall 9	1993 Nov 21	22.0	0.945 ± 0.007	19983	1146	26	19.0 ± 1.0	Re97
3C 120	1994 Feb 17	47.4	1.828 ± 0.006	83155	1150	26	43.8 ± 2.2	Re97
NGC 3227	1993 May 08	33.4	0.644 ± 0.004	20028	1162	14	25.5 ± 1.3	Pt94, Re97
NGC 3516	1994 Apr 02	29.4	2.353 ± 0.009	65410	1161	26	73.5 ± 3.7	Re97
NGC 3783(1)	1993 Dec 19	17.5	1.032 ± 0.008	16442	1065	14	46.4 ± 2.3	Ge95, Re97, Ge97
NGC 3783(2)	1993 Dec 23	14.9	1.267 ± 0.010	17270	1034	14	55.9 ± 2.8	Ge95, Re97, Ge97
NGC 4051	1993 Apr 25	27.6	0.939 ± 0.006	25131	1015	12	21.2 ± 1.1	Mi94, Re97
NGC 4151(2)	1993 Nov 05	13.4	2.126 ± 0.013	23726	816	22	182.5 ± 9.1	We94
NGC 4151(4)	1993 Dec 05	10.8	2.167 ± 0.015	18626	1483	19	198.7 ± 9.9	Wa96
NGC 4151(5)	1993 Dec 07	11.7	2.455 ± 0.015	23096	1263	14	223.4 ± 11.2	Wa96
Mrk 766	1993 Dec 18	33.7	0.828 ± 0.005	36761	1207	26	18.1 ± 0.9	Le96
NGC 4593	1994 Jan 09	21.4	1.463 ± 0.009	30079	1337	16	31.8 ± 1.6	Re97
MCG-6-30-15(1)	1993 Jul 09	29.8	1.806 ± 0.008	51748	1110	14	43.2 ± 2.2	Fa94, Re95
MCG-6-30-15(2)	1993 Jul 31	31.4	1.192 ± 0.007	35628	1088	14	35.6 ± 1.8	Fa94, Re95
IC 4329A	1993 Aug 15	29.2	2.075 ± 0.009	56677	1325	14	77.3 ± 3.9	Ca96
NGC 5548	1993 Jul 27	20.4	1.795 ± 0.010	34919	1188	14	46.1 ± 2.3	Re97
Mrk 841(1)	1993 Aug 22	30.5	0.440 ± 0.004	12897	759	14	12.2 ± 0.6	...
Mrk 841(2)	1994 Feb 21	20.9	0.332 ± 0.042	6623	420	14	10.3 ± 0.5	Re97
NGC 6814(1)	1993 May 04	40.3	0.028 ± 0.001	1001	211	5	1.2 ± 0.1	Re97
Mrk 509	1994 Apr 29	40.1	2.008 ± 0.008	77504	1318	26	42.9 ± 2.1	Re97
NGC 7469(2)	1993 Nov 26	14.5	1.052 ± 0.009	15202	1003	26	27.5 ± 1.4	Gu94
MCG-2-58-22	1993 May 25	13.3	0.423 ± 0.006	5309	860	17	14.0 ± 0.7	We95, Re97

NOTE.— Columns— (1) Source name; (2) observation date (start of exposure); (3) exposure time in SIS0 of selected data; (4) mean SIS0 count rate in the 0.6–10.0 keV band; (5) number of source photons detected by SIS0 in the 0.6–5.0, 7.0–10.0 keV band; (6) number of spectral data points (all instruments; 0.6–5.0, 7.0–10.0 keV band) included in the spectral analysis; (7) number of good-quality spectral data points (SIS0 & SIS1) below 0.6 keV; (8) observed flux in the 2–10 keV band (excluding any Fe line emission) with 5% errors; (9) references to other papers discussing the same *ASCA* dataset: Fa95 - Fabian et al 1994; Ge95 - George, Turner, Netzer 1995; Ge97 - George et al 1997b; Gu94 - Guainazzi et al 1994; Le96 - Leighly et al 1996b; Mi94 - Mihara et al 1994; Pt94 - Ptak et al 1994; Re95 - Reynolds et al 1995; Re97 - Reynolds 1997; Wa96 - Warwick et al 1996; We94 - Weaver et al 1994b; We95 - Weaver et al 1995. All datasets are also discussed in Papers I & II.

TABLE 3
 MODEL $A(i)$: RESULTS FOR A NEUTRAL ABSORBER (WITH $D_f = 0$ - SEE §5.1)

Name	$N_{H,0}$ (10^{21} cm $^{-2}$)	Γ	$N_{H,z}$ (10^{21} cm $^{-2}$)	$\chi^2_{A_i}$	P_{A_i}	$\frac{\Delta\chi^2_{0.6}}{\Delta N_{0.6}}$	$\overline{R_{0.6}}$
Mrk 335	$0.40^{+0.02}_{-0.00}$ (<i>p</i>)	$2.18^{+0.03}_{-0.02}$	$0.00^{+0.02}_{-0.00}$ (<i>p</i>)	719	0.98	8.1	1.3
Fairall 9	$0.30^{+0.07}_{-0.00}$ (<i>p</i>)	$1.98^{+0.01}_{-0.01}$	$0.00^{+0.08}_{-0.00}$ (<i>p</i>)	1230	0.97	2.6	0.9
3C 120	$1.23^{+0.62}_{-0.00}$ (<i>p</i>)	$2.00^{+0.01}_{-0.02}$	$0.46^{+0.07}_{-0.46}$ (<i>p</i>)	1186	0.82	9.6	0.8
NGC 3227	$2.11^{+0.18}_{-1.89}$ (<i>p</i>)	$1.55^{+0.03}_{-0.02}$	$0.00^{+2.07}_{-0.00}$ (<i>p</i>)	1268	0.99	20.3	2.4
NGC 3516	$1.60^{+0.88}_{-1.31}$ (<i>p</i>)	$1.64^{+0.01}_{-0.02}$	$0.00^{+0.60}_{-0.00}$ (<i>p</i>)	3214	1.00	128.2	3.1
NGC 3783(1)	$5.62^{+0.31}_{-3.10}$	$1.44^{+0.03}_{-0.03}$	$0.00^{+3.16}_{-0.00}$ (<i>p</i>)	2121	1.00	17.9	15.1
NGC 3783(2)	$4.04^{+0.28}_{-2.66}$	$1.37^{+0.03}_{-0.03}$	$0.00^{+2.69}_{-0.00}$ (<i>p</i>)	2114	1.00	22.7	12.6
NGC 4051	$0.13^{+0.01}_{-0.00}$ (<i>p</i>)	$2.09^{+0.02}_{-0.01}$	$0.00^{+0.01}_{-0.00}$ (<i>p</i>)	1703	1.00	60.7	1.7
NGC 4151(2)	$0.21^{+8.98}_{-0.00}$ (<i>p</i>)	$1.02^{+0.04}_{-0.02}$	$13.99^{+0.66}_{-13.99}$ (<i>p</i>)	1995	1.00	18.7	8.8
NGC 4151(4)	$0.21^{+4.36}_{-0.00}$ (<i>p</i>)	$0.95^{+0.03}_{-0.04}$	$20.10^{+0.80}_{-20.10}$ (<i>p</i>)	3235	1.00	16.1	9.5
NGC 4151(5)	$0.21^{+3.75}_{-0.00}$ (<i>p</i>)	$1.09^{+0.03}_{-0.03}$	$22.78^{+0.69}_{-22.78}$ (<i>p</i>)	3518	1.00	23.9	8.8
Mrk 766	$0.16^{+0.10}_{-0.00}$ (<i>p</i>)	$1.82^{+0.02}_{-0.01}$	$0.00^{+0.10}_{-0.00}$ (<i>p</i>)	1415	1.00	16.4	1.4
NGC 4593	$0.16^{+0.57}_{-0.00}$ (<i>p</i>)	$1.93^{+0.02}_{-0.02}$	$0.49^{+0.10}_{-0.49}$ (<i>p</i>)	1402	0.92	17.1	1.3
MCG-6-30-15(1)	$0.41^{+0.59}_{-0.00}$ (<i>p</i>)	$1.88^{+0.02}_{-0.01}$	$0.51^{+0.09}_{-0.51}$ (<i>p</i>)	1942	1.00	136.0	2.0
MCG-6-30-15(2)	$1.04^{+0.14}_{-0.63}$ (<i>p</i>)	$1.67^{+0.02}_{-0.03}$	$0.00^{+0.56}_{-0.00}$ (<i>p</i>)	2051	1.00	127.3	2.5
IC 4329A	$0.45^{+3.24}_{-0.00}$ (<i>p</i>)	$1.84^{+0.01}_{-0.01}$	$4.14^{+0.11}_{-4.05}$	1710	1.00	17.6	2.2
NGC 5548	$0.32^{+0.10}_{-0.16}$ (<i>p</i>)	$1.81^{+0.02}_{-0.01}$	$0.00^{+0.12}_{-0.00}$ (<i>p</i>)	1377	1.00	26.8	1.3
Mrk 841(1)	$0.22^{+0.12}_{-0.00}$ (<i>p</i>)	$1.81^{+0.03}_{-0.02}$	$0.00^{+0.12}_{-0.00}$ (<i>p</i>)	834	0.98	9.6	1.3
Mrk 841(2)	$0.22^{+0.07}_{-0.00}$ (<i>p</i>)	$1.63^{+0.03}_{-0.03}$	$0.00^{+0.10}_{-0.00}$ (<i>p</i>)	407	0.43	3.3	1.3
NGC 6814(1)	$1.00^{+0.76}_{-0.02}$ (<i>p</i>)	$1.68^{+0.13}_{-0.07}$	$0.00^{+0.08}_{-0.00}$ (<i>p</i>)	160	0.01	0.0	1.0
Mrk 509	$0.42^{+0.31}_{-0.00}$ (<i>p</i>)	$1.93^{+0.02}_{-0.01}$	$0.25^{+0.08}_{-0.25}$ (<i>p</i>)	1335	0.69	4.5	1.1
NGC 7469(2)	$0.62^{+0.15}_{-0.14}$ (<i>p</i>)	$2.01^{+0.01}_{-0.02}$	$0.00^{+0.28}_{-0.00}$ (<i>p</i>)	998	0.54	1.8	1.1
MCG-2-58-22	$0.34^{+0.12}_{-0.00}$ (<i>p</i>)	$1.74^{+0.03}_{-0.02}$	$0.00^{+0.13}_{-0.00}$ (<i>p</i>)	931	0.97	1.1	1.0

NOTE.— Fits undertaken in the 0.6–10.0 keV band, **excluding** the 5.0–7.0 keV band. Error bars on the fit parameters are 68 per cent confidence limits for 3 interesting parameters. (*p*) indicates that the parameter ‘pegged’ at the specified limit. Columns— (1) Source name; (2) the column density of neutral gas at $z = 0$ (constrained to be $\geq N_{H,0}^{gal}$ given in Table 1); (3) photon index; (4) the column density at the redshift of the source; (5) χ^2 -statistic for the fit for the N_{pts} data points given in Table 2; (6) probability that the χ^2 -statistic should be less than $\chi^2_{A_i}$ for the number of degrees of freedom, *dof*, given by $N_{pts} - 8$; (7) ratio of the increase in the χ^2 -statistic to the increase in the number of data points when the best-fitting model is extrapolated below 0.6 keV; (8) mean data/model ratio for data points below 0.6 keV

TABLE 4
 MODEL $A(ii)$: RESULTS FOR A NEUTRAL ABSORBER, WITH D_f FREE (SEE §5.2)

Name	$N_{H,0}$ (10^{21} cm $^{-2}$)	Γ	$N_{H,z}$ (10^{21} cm $^{-2}$)	$\log D_f$	χ^2_{Aii}	P_{Aii}	$\frac{\Delta\chi^2_{0.6}}{\Delta N_{0.6}}$	$\overline{R}_{0.6}$	$F(\frac{Aii}{A})$
Mrk 335	$0.40^{+0.12}_{-0.00}$ (p)	$2.40^{+0.08}_{-0.07}$	$55.87^{+28.34}_{-15.25}$	$-0.215^{+0.050}_{-0.049}$	636	0.46	2.7	1.1	83.7
Fairall 9	$0.38^{+0.17}_{-0.08}$ (p)	$2.02^{+0.06}_{-0.04}$	$305.65^{+4791.39}_{-191.6}$	$-0.097^{+0.077}_{-0.079}$	1222	0.96	2.0	0.9	7.4
3C 120	$1.79^{+0.08}_{-0.09}$	$2.04^{+0.02}_{-0.03}$	$538.96^{+278.92}_{-162.82}$	$-0.173^{+0.062}_{-0.035}$	1142	0.52	9.0	0.8	44.0
NGC 3227	$0.22^{+0.35}_{-0.00}$ (p)	$1.66^{+0.04}_{-0.04}$	$5.02^{+0.86}_{-0.87}$	$-0.449^{+0.087}_{-0.047}$	1189	0.78	3.1	1.2	76.7
NGC 3516	$0.29^{+0.01}_{-0.00}$ (p)	$1.99^{+0.04}_{-0.03}$	$9.50^{+0.51}_{-0.45}$	$-0.446^{+0.017}_{-0.025}$	1962	1.00	31.0	1.5	736.0
NGC 3783(1)	$0.87^{+0.05}_{-0.00}$ (p)	$1.89^{+0.05}_{-0.06}$	$14.77^{+0.93}_{-0.93}$	$-0.788^{+0.037}_{-0.038}$	1338	1.00	6.4	2.1	618.5
NGC 3783(2)	$0.87^{+0.04}_{-0.00}$ (p)	$1.84^{+0.06}_{-0.06}$	$13.98^{+1.01}_{-1.00}$	$-0.668^{+0.039}_{-0.038}$	1429	1.00	10.2	2.5	491.7
NGC 4051	$0.13^{+0.01}_{-0.00}$ (p)	$2.51^{+0.07}_{-0.03}$	$27.60^{+2.49}_{-0.06}$	$-0.299^{+0.040}_{-0.041}$	1439	1.00	12.6	1.2	184.7
NGC 4151(2)	$0.21^{+0.12}_{-0.00}$ (p)	$1.40^{+0.06}_{-0.06}$	$22.57^{+1.04}_{-1.02}$	$-1.212^{+0.041}_{-0.040}$	911	1.00	3.9	8.8	961.8
NGC 4151(4)	$0.21^{+0.22}_{-0.00}$ (p)	$1.30^{+0.04}_{-0.05}$	$33.27^{+1.29}_{-1.27}$	$-1.199^{+0.032}_{-0.032}$	1577	0.97	3.8	1.6	1551.0
NGC 4151(5)	$0.21^{+0.29}_{-0.00}$ (p)	$1.40^{+0.04}_{-0.04}$	$33.11^{+1.30}_{-1.01}$	$-1.302^{+0.032}_{-0.029}$	1439	1.00	4.4	1.4	1814.1
Mrk 766	$0.16^{+0.04}_{-0.00}$ (p)	$2.26^{+0.07}_{-0.06}$	$12.76^{+1.25}_{-1.25}$	$-0.317^{+0.045}_{-0.044}$	1201	0.53	4.4	1.2	213.8
NGC 4593	$0.20^{+0.12}_{-0.00}$ (p)	$2.01^{+0.05}_{-0.02}$	$4.40^{+1.37}_{-1.42}$	$-0.162^{+0.040}_{-0.032}$	1366	0.77	3.4	1.1	35.0
MCG-6-30-15(1)	$0.41^{+0.02}_{-0.00}$ (p)	$2.25^{+0.05}_{-0.05}$	$9.59^{+0.76}_{-0.78}$	$-0.338^{+0.031}_{-0.030}$	1494	1.00	28.1	1.3	330.4
MCG-6-30-15(2)	$0.41^{+0.03}_{-0.00}$ (p)	$2.15^{+0.05}_{-0.06}$	$12.05^{+0.85}_{-0.89}$	$-0.415^{+0.036}_{-0.035}$	1510	1.00	28.7	1.5	386.7
IC 4329A	$0.45^{+0.43}_{-0.00}$ (p)	$1.89^{+0.02}_{-0.03}$	$4.48^{+0.30}_{-0.29}$	$-1.134^{+0.136}_{-0.128}$	1658	1.00	1.1	1.0	41.3
NGC 5548	$0.17^{+0.03}_{-0.00}$ (p)	$1.91^{+0.04}_{-0.04}$	$7.09^{+1.80}_{-1.74}$	$-0.109^{+0.028}_{-0.028}$	1322	1.00	15.0	1.2	49.1
Mrk 841(1)	$0.22^{+0.14}_{-0.00}$ (p)	$1.92^{+0.08}_{-0.11}$	$11.43^{+19.21}_{-8.41}$	$-0.076^{+0.048}_{-0.074}$	829	0.98	7.6	1.2	4.5
Mrk 841(2)	$0.22^{+0.18}_{-0.00}$ (p)	$1.73^{+0.14}_{-0.12}$	$29.75^{+601.21}_{-29.43}$ (p)	$-0.071^{+0.071}_{-0.092}$ (p)	403	0.40	2.2	1.2	4.1
NGC 6814(1)	$0.98^{+1.14}_{-0.00}$ (p)	$1.76^{+0.46}_{-0.16}$	$10.78^{+620.02}_{-10.46}$ (p)	$-0.059^{+0.059}_{-5.941}$ (p)	160	0.01	0.1	0.9	0.5
Mrk 509	$0.44^{+0.16}_{-0.0}$ (p)	$1.97^{+0.03}_{-0.04}$	$2.83^{+0.40}_{-1.97}$	$-0.088^{+0.058}_{-0.082}$	1326	0.63	2.7	1.0	8.9
NGC 7469(2)	$0.80^{+0.19}_{-0.19}$	$2.07^{+0.04}_{-0.05}$	$519.49^{+976.63}_{-237.92}$	$-0.244^{+0.130}_{-0.414}$	979	0.37	2.8	1.2	19.5
MCG-2-58-22	$0.53^{+0.46}_{-0.19}$ (p)	$1.84^{+0.14}_{-0.08}$	$201.30^{+237.91}_{-92.34}$	$-0.130^{+0.073}_{-0.005}$	917	0.94	1.1	1.0	13.0

NOTE.— As for Table 3, except error bars on the fit parameters are 68 per cent confidence limits for 4 interesting parameters ($do_f = N_{pts} - 9$), D_f is the fraction of the observed continuum **unattenuated** by the column $N_{H,z}$, and $F(\frac{Aii}{A})$ is the F -statistic for model $A(ii)$ versus $A(i)$.

TABLE 5
 MODEL $B(i)$: RESULTS FOR AN IONIZED ABSORBER (WITH $D_f = 0$ - SEE §5.3)

Name	$N_{H,0}$ (10^{21} cm $^{-2}$)	Γ	$N_{H,z}^*$ (10^{21} cm $^{-2}$)	U_X^*	χ_{Bi}^2	P_{Bi}	$\frac{\Delta\chi_{0.6}^2}{\Delta N_{0.6}}$	$\overline{R}_{0.6}$	$F(\frac{Bi}{Ai})$
Mrk 335	$0.40^{+0.08}_{-0.00}$ (p)	$2.20^{+0.04}_{-0.03}$	$40.51^{+22.59}_{-15.59}$	$1.966^{+1.048}_{-0.660}$	641	0.51	2.9	1.1	78.1
Fairall 9	$0.30^{+0.11}_{-0.00}$ (p)	$1.98^{+0.03}_{-0.02}$	$63.59^{+129.30}_{-63.27}$ (p)	$9.828^{+1.418}_{-0.698}$ (p)	1228	0.97	2.9	0.9	1.9
3C 120	$1.68^{+0.08}_{-0.07}$	$2.00^{+0.02}_{-0.02}$	$20.01^{+22.09}_{-10.69}$ (p)	$9.997^{+0.003}_{-3.953}$ (p)	1182	0.81	11.3	0.8	3.9
NGC 3227	$0.44^{+0.84}_{-0.22}$ (p)	$1.63^{+0.03}_{-0.03}$	$4.00^{+0.72}_{-1.00}$	$0.014^{+0.037}_{-0.005}$	1175	0.68	1.3	1.0	91.3
NGC 3516	$0.48^{+0.12}_{-0.12}$	$1.92^{+0.03}_{-0.02}$	$8.71^{+0.68}_{-0.65}$	$0.106^{+0.013}_{-0.011}$	1400	1.00	2.7	1.0	1494.2
NGC 3783(1)	$1.14^{+0.38}_{-0.24}$	$1.81^{+0.07}_{-0.05}$	$23.40^{+2.54}_{-2.16}$	$0.146^{+0.027}_{-0.013}$	1134	0.95	1.1	0.8	914.7
NGC 3783(2)	$0.87^{+0.24}_{-0.00}$ (p)	$1.78^{+0.06}_{-0.04}$	$22.65^{+2.74}_{-1.97}$	$0.158^{+0.018}_{-0.014}$	1087	0.91	1.4	0.8	969.8
NGC 4051	$0.13^{+0.02}_{-0.00}$ (p)	$2.29^{+0.04}_{-0.03}$	$20.92^{+2.78}_{-3.87}$	$0.686^{+0.070}_{-0.105}$	1283	1.00	3.8	1.1	329.7
NGC 4151(2)	$2.51^{+0.30}_{-0.28}$	$1.40^{+0.05}_{-0.06}$	$49.44^{+2.57}_{-2.78}$	$0.144^{+0.008}_{-0.006}$	1032	1.00	1.8	1.2	754.1
NGC 4151(4)	$2.89^{+0.27}_{-0.26}$	$1.38^{+0.05}_{-0.04}$	$95.19^{+3.57}_{-4.03}$	$0.212^{+0.007}_{-0.006}$	1721	1.00	2.3	1.3	1297.3
NGC 4151(5)	$3.47^{+0.26}_{-0.24}$	$1.52^{+0.04}_{-0.04}$	$96.74^{+3.23}_{-3.33}$	$0.208^{+0.006}_{-0.005}$	1648	1.00	4.6	1.3	1424.2
Mrk 766	$0.18^{+0.07}_{-0.00}$ (p)	$2.09^{+0.04}_{-0.03}$	$6.05^{+1.00}_{-0.89}$	$0.163^{+0.027}_{-0.026}$	1104	0.03	1.6	1.0	337.8
NGC 4593	$0.51^{+0.16}_{-0.31}$ (p)	$2.02^{+0.04}_{-0.04}$	$1.95^{+0.99}_{-0.66}$	$0.089^{+0.061}_{-0.079}$	1344	0.63	3.1	1.1	57.4
MCG-6-30-15(1)	$0.41^{+0.09}_{-0.00}$ (p)	$2.14^{+0.03}_{-0.02}$	$5.85^{+0.58}_{-0.59}$	$0.111^{+0.019}_{-0.017}$	1188	0.97	7.6	1.0	699.4
MCG-6-30-15(2)	$0.41^{+0.06}_{-0.00}$ (p)	$2.02^{+0.03}_{-0.03}$	$9.87^{+0.91}_{-0.91}$	$0.171^{+0.016}_{-0.017}$	1161	0.96	5.5	1.0	827.9
IC 4329A	$3.63^{+0.35}_{-0.41}$	$1.89^{+0.02}_{-0.03}$	$2.14^{+0.61}_{-0.68}$	$0.037^{+0.049}_{-0.023}$	1672	1.00	5.4	1.3	29.9
NGC 5548	$0.17^{+0.05}_{-0.00}$ (p)	$1.94^{+0.02}_{-0.03}$	$3.21^{+0.77}_{-0.79}$	$0.115^{+0.027}_{-0.028}$	1232	0.86	5.5	1.0	138.9
Mrk 841(1)	$0.22^{+0.16}_{-0.00}$ (p)	$1.92^{+0.07}_{-0.06}$	$3.05^{+2.86}_{-1.78}$	$0.163^{+0.164}_{-0.079}$	816	0.95	3.8	1.1	16.1
Mrk 841(2)	$0.22^{+0.12}_{-0.00}$ (p)	$1.70^{+0.09}_{-0.08}$	$3.00^{+21.41}_{-2.68}$ (p)	$0.258^{+10.988}_{-0.204}$ (p)	402	0.38	1.6	1.1	5.1
NGC 6814(1)	$0.98^{+0.97}_{-0.11}$ (p)	$1.71^{+0.24}_{-0.11}$	$2.51^{+35.51}_{-2.19}$ (p)	$0.307^{+10.913}_{-0.306}$ (p)	160	0.01	0.1	0.9	0.3
Mrk 509	$0.42^{+0.17}_{-0.00}$ (p)	$1.97^{+0.03}_{-0.03}$	$0.82^{+0.24}_{-0.35}$	$0.010^{+0.039}_{-0.035}$	1312	0.53	4.4	0.9	23.0
NGC 7469(2)	$0.69^{+0.17}_{-0.16}$	$2.02^{+0.04}_{-0.04}$	$109.09^{+184.40}_{-91.06}$	$8.142^{+2.834}_{-4.242}$ (p)	990	0.47	2.1	1.1	8.1
MCG-2-58-22	$0.34^{+0.28}_{-0.00}$ (p)	$1.74^{+0.06}_{-0.03}$	$127.79^{+241.53}_{-108.16}$	$7.505^{+3.741}_{-5.314}$ (p)	921	0.95	1.1	1.0	9.1

NOTE.— As for Tables 3 & 4, except error bars on the fit parameters are 68 per cent confidence limits for 4 interesting parameters ($dof = N_{pts} - 9$), U_X is the ionization parameter of the ionized gas, and $F(\frac{Bi}{Ai})$ is the F -statistic for model $B(i)$ versus $A(i)$.

TABLE 6
MODEL $B(ii)$: RESULTS FOR AN IONIZED ABSORBER, WITH D_f FREE (SEE §5.4)

Name	$N_{H,0}$ (10^{21} cm $^{-2}$)	Γ	$N_{H,z}^*$ (10^{21} cm $^{-2}$)	U_X^*	$\log D_f$	χ_{Bii}^2	P_{Bii}	$\frac{\Delta\chi_{0.6}^2}{\Delta N_{0.6}}$	$\overline{R}_{0.6}$	$F(\frac{Bii}{Aii})$	$F(\frac{Bii}{B(i)})$
Mrk 335	$0.40^{+0.19}_{-0.00}$ (p)	$2.36^{+0.15}_{-0.14}$	$140.93^{+468.47}_{-59.82}$	$0.613^{+0.956}_{-0.420}$	$-0.198^{+0.090}_{-0.074}$	631	0.41	4.2	0.9	5.1	10.0
Fairall 9	$0.36^{+0.27}_{-0.00}$ (p)	$2.01^{+0.08}_{-0.04}$	$528.45^{+102.51}_{-403.28}$ (p)	$0.005^{+11.241}_{-0.004}$ (p)	$-0.086^{+0.078}_{-0.084}$	1223	0.96	2.4	0.9	†	4.7
3C 120	$1.80^{+0.10}_{-0.10}$	$2.04^{+0.03}_{-0.02}$	$630.96^{+0.00}_{-128.04}$ (p)	$0.082^{+9.918}_{-0.081}$ (p)	$-0.122^{+0.007}_{-0.029}$	1146	0.56	8.7	0.8	†	34.7
NGC 3227	$0.38^{+0.90}_{-0.16}$ (p)	$1.64^{+0.04}_{-0.04}$	$5.03^{+3.22}_{-1.59}$	$0.013^{+0.001}_{-0.005}$	$-0.915^{+0.493}_{-5.085}$ (p)	1175	0.69	1.4	0.9	13.7	0.0
NGC 3516	$0.48^{+0.14}_{-0.13}$	$1.92^{+0.03}_{-0.03}$	$8.71^{+0.76}_{-0.72}$	$0.106^{+0.015}_{-0.013}$	$-6.000^{+0.000}_{-0.000}$ (p)	1400	1.00	2.7	1.0	462.6	0.0
NGC 3783(1)	$0.87^{+0.17}_{-0.00}$ (p)	$1.88^{+0.08}_{-0.07}$	$25.42^{+2.58}_{-2.18}$	$0.096^{+0.021}_{-0.012}$	$-1.020^{+0.068}_{-0.172}$	1121	0.92	1.4	0.8	204.3	12.1
NGC 3783(2)	$0.87^{+0.27}_{-0.00}$ (p)	$1.78^{+0.07}_{-0.04}$	$22.65^{+2.99}_{-2.17}$	$0.158^{+0.019}_{-0.016}$	$-6.000^{+0.000}_{-0.000}$ (p)	1087	0.92	1.4	0.9	322.6	0.0
NGC 4051	$0.13^{+0.09}_{-0.00}$ (p)	$2.35^{+0.04}_{-0.03}$	$100.53^{+12.61}_{-20.36}$	$0.792^{+0.044}_{-0.133}$	$-0.260^{+0.024}_{-0.036}$	1178	1.00	3.6	0.9	223.9	83.2
NGC 4151(2)	$0.21^{+0.35}_{-0.00}$ (p)	$1.49^{+0.08}_{-0.07}$	$43.74^{+2.67}_{-3.01}$	$0.062^{+0.005}_{-0.009}$	$-1.355^{+0.060}_{-0.019}$	868	0.94	2.0	1.0	88.4	128.4
NGC 4151(4)	$0.21^{+0.59}_{-0.00}$ (p)	$1.42^{+0.05}_{-0.06}$	$66.07^{+5.23}_{-3.84}$	$0.080^{+0.017}_{-0.012}$	$-1.328^{+0.048}_{-0.042}$	1486	0.60	2.3	0.9	90.0	201.4
NGC 4151(5)	$0.21^{+0.48}_{-0.00}$ (p)	$1.52^{+0.05}_{-0.05}$	$63.50^{+4.05}_{-3.20}$	$0.067^{+0.013}_{-0.015}$	$-1.412^{+0.028}_{-0.055}$	1344	0.96	2.9	1.0	88.7	231.5
Mrk 766	$0.18^{+0.15}_{-0.00}$ (p)	$2.18^{+0.08}_{-0.07}$	$16.07^{+4.34}_{-4.87}$	$0.111^{+0.053}_{-0.033}$	$-0.346^{+0.044}_{-0.036}$	1088	0.01	2.1	1.0	124.4	17.4
NGC 4593	$0.50^{+0.19}_{-0.30}$ (p)	$2.02^{+0.04}_{-0.04}$	$1.97^{+1.17}_{-0.75}$	$0.089^{+0.069}_{-0.080}$	$-6.000^{+0.000}_{-0.000}$ (p)	1344	0.63	3.1	1.1	21.8	0.0
MCG-6-30-15(1)	$0.41^{+0.10}_{-0.00}$ (p)	$2.14^{+0.03}_{-0.03}$	$5.85^{+0.70}_{-0.67}$	$0.111^{+0.022}_{-0.020}$	$-6.000^{+0.000}_{-0.000}$ (p)	1188	0.97	7.6	1.0	283.6	0.0
MCG-6-30-15(2)	$0.41^{+0.08}_{-0.00}$ (p)	$2.02^{+0.04}_{-0.03}$	$9.87^{+1.01}_{-1.01}$	$0.171^{+0.018}_{-0.019}$	$-6.000^{+0.000}_{-0.000}$ (p)	1161	0.96	5.5	1.0	324.3	0.0
IC 4329A	$3.57^{+0.43}_{-0.39}$	$1.89^{+0.02}_{-0.03}$	$2.27^{+0.55}_{-0.87}$	$0.032^{+0.042}_{-0.20}$	$-6.000^{+0.000}_{-0.000}$ (p)	1672	1.00	2.8	1.3	†	0.0
NGC 5548	$0.17^{+0.06}_{-0.00}$ (p)	$1.94^{+0.03}_{-0.03}$	$3.21^{+0.87}_{-0.88}$	$0.115^{+0.030}_{-0.032}$	$-6.000^{+0.000}_{-0.000}$ (p)	1232	0.87	5.5	1.0	86.1	0.0
Mrk 841(1)	$0.22^{+0.21}_{-0.00}$ (p)	$1.93^{+0.07}_{-0.07}$	$5.13^{+82.21}_{-3.51}$	$0.168^{+0.463}_{-0.099}$	$-0.472^{+0.409}_{-5.528}$ (p)	816	0.96	3.6	1.1	11.7	0.0
Mrk 841(2)	$0.22^{+0.60}_{-0.00}$ (p)	$1.78^{+0.18}_{-0.15}$	$48.85^{+582.11}_{-38.04}$ (p)	$0.255^{+1.036}_{-0.187}$	$-0.122^{+0.030}_{-0.087}$	396	0.32	0.7	1.0	6.9	6.2
NGC 6814(1)	$0.98^{+1.04}_{-0.00}$ (p)	$1.71^{+0.33}_{-0.22}$	$0.32^{+630.64}_{-0.00}$ (p)	$0.001^{+9.999}_{-0.000}$ (p)	$-0.857^{+0.143}_{-5.143}$ (p)	160	0.01	0.1	1.0	0.0	0.0
Mrk 509	$0.42^{+0.20}_{-0.00}$ (p)	$1.97^{+0.03}_{-0.03}$	$0.82^{+0.05}_{-0.39}$	$0.010^{+0.057}_{-0.007}$	$-2.455^{+2.322}_{-3.545}$ (p)	1312	0.54	4.4	0.9	14.0	0.0
NGC 7469(2)	$0.82^{+0.33}_{-0.21}$	$2.08^{+0.06}_{-0.05}$	$630.96^{+0.00}_{-236.05}$ (p)	$0.094^{+0.014}_{-0.093}$ (p)	$-0.184^{+0.106}_{-0.065}$	979	0.38	2.9	1.2	0.0	11.1
MCG-2-58-22	$0.78^{+0.74}_{-0.44}$ (p)	$1.90^{+0.21}_{-0.13}$	$630.09^{+0.00}_{-118.41}$ (p)	$1.477^{+0.462}_{-1.476}$ (p)	$-0.149^{+0.081}_{-0.100}$	913	0.93	1.3	0.9	3.7	7.4

NOTE.— As for Tables 3–5, except error bars on the fit parameters are 68 per cent confidence limits for 5 interesting parameters ($dof = N_{pts} - 10$), $F(\frac{Bii}{Aii})$ is the F -statistic for model $B(ii)$ versus $A(ii)$, and $F(\frac{Bii}{B(i)})$ is that for model $B(ii)$ versus $B(i)$. The increase in χ_{Bii}^2 compared to χ_{Aii}^2 for the datasets marked with a † is an artifact of the limited range in $N_{H,z}$ - U_X parameter-space considered in our ION models. For these 3 datasets a superior fit is obtained assuming model $A(ii)$ in which the absorbing material is assumed to be neutral (i.e. $U_X = 0$). The grids used for models $B(i)$ - $C(ii)$ have a minimum $U_X = 10^{-3}$ (§3). Due to the interplay between the data and model during the spectral analysis, the solutions for these 3 datasets most likely represent local minima in χ^2 -space. However we note that in all 3 cases yet superior fits are obtained for subsequent models presented here, and none of our conclusions rely upon the results from these datasets.

TABLE 7
 MODEL $C(i)$: RESULTS FOR AN IONIZED ABSORBER (WITH $D_j = 0$) AND AN IONIZED EMITTER (SEE §5.5)

Name	$N_{H,0}$ (10^{21} cm $^{-2}$)	Γ	$N_{H,z}^*$ (10^{21} cm $^{-2}$)	U_X^*	$\log(\Omega/4\pi)$	$\chi^2_{C_i}$	P_{C_i}	$\frac{\Delta\chi^2_{0.6}}{\Delta N_{0.6}}$	$\overline{R}_{0.6}$	$F(\frac{C_i}{B_i})$
Mrk 335	$0.40^{+0.15}_{-0.00}$ (p)	$2.17^{+0.06}_{-0.06}$	$51.50^{+41.68}_{-23.79}$	$2.291^{+1.559}_{-0.877}$	$-0.034^{+0.383}_{-0.546}$	633	0.43	3.0	1.1	8.1
Fairall 9	$0.31^{+0.19}_{-0.01}$ (p)	$1.97^{+0.04}_{-0.03}$	$48.37^{+156.04}_{-48.05}$ (p)	$5.802^{+5.444}_{-5.642}$ (p)	$0.732^{+0.574}_{-4.732}$ (p)	1225	0.97	2.5	0.9	2.8
3C 120	$1.69^{+0.10}_{-0.08}$	$1.98^{+0.02}_{-0.02}$	$68.58^{+45.24}_{-47.77}$	$9.847^{+0.153}_{-4.788}$ (p)	$0.375^{+0.252}_{-0.589}$	1168	0.72	10.5	0.8	13.7
NGC 3227	$0.22^{+0.94}_{-0.00}$ (p)	$1.64^{+0.04}_{-0.04}$	$4.23^{+0.50}_{-1.29}$	$0.009^{+0.037}_{-0.004}$	$0.828^{+0.387}_{-4.828}$	1173	0.67	6.0	0.8	2.0
NGC 3516	$0.50^{+0.20}_{-0.15}$	$1.92^{+0.03}_{-0.03}$	$8.74^{+0.81}_{-0.74}$	$0.107^{+0.017}_{-0.017}$	$-1.063^{+0.176}_{-2.937}$	1400	1.00	2.5	1.0	0.0
NGC 3783(1)	$1.62^{+0.38}_{-0.35}$	$1.83^{+0.08}_{-0.05}$	$23.77^{+4.09}_{-2.41}$	$0.149^{+0.027}_{-0.018}$	$0.180^{+0.187}_{-0.280}$	1104	0.86	0.5	0.9	28.7
NGC 3783(2)	$1.16^{+0.37}_{-0.29}$ (p)	$1.80^{+0.07}_{-0.07}$	$23.25^{+2.94}_{-3.50}$	$0.162^{+0.019}_{-0.027}$	$-0.114^{+0.277}_{-0.666}$	1076	0.87	0.8	0.9	10.5
NGC 4051	$0.13^{+0.06}_{-0.00}$ (p)	$2.21^{+0.05}_{-0.04}$	$16.99^{+5.34}_{-3.88}$	$0.595^{+0.137}_{-0.111}$	$-0.117^{+0.195}_{-0.094}$	1124	0.99	6.1	1.1	142.3
NGC 4151(2)	$2.97^{+0.35}_{-0.34}$	$1.40^{+0.07}_{-0.06}$	$48.90^{+2.99}_{-3.10}$	$0.142^{+0.009}_{-0.006}$	$0.118^{+0.163}_{-0.230}$	992	1.00	1.8	1.2	33.6
NGC 4151(4)	$3.15^{+0.34}_{-0.33}$	$1.39^{+0.05}_{-0.05}$	$94.97^{+4.14}_{-4.13}$	$0.211^{+0.008}_{-0.006}$	$-0.272^{+0.253}_{-0.556}$	1709	1.00	2.4	1.4	10.3
NGC 4151(5)	$3.62^{+0.31}_{-0.31}$	$1.53^{+0.04}_{-0.05}$	$96.89^{+3.11}_{-3.69}$	$0.207^{+0.007}_{-0.005}$	$-0.577^{+0.336}_{-3.423}$ (p)	1643	1.00	4.7	1.3	3.8
Mrk 766	$0.20^{+0.27}_{-0.02}$ (p)	$2.07^{+0.06}_{-0.04}$	$5.36^{+1.56}_{-1.20}$	$0.136^{+0.050}_{-0.044}$	$0.105^{+0.288}_{-0.472}$	1085	0.01	2.5	0.9	20.9
NGC 4593	$0.51^{+0.18}_{-0.31}$ (p)	$2.02^{+0.04}_{-0.04}$	$1.95^{+0.15}_{-0.75}$	$0.091^{+0.067}_{-0.084}$	$-4.000^{+4.764}_{-0.000}$ (p)	1344	0.63	3.2	1.1	0.0
MCG-6-30-15(1)	$0.41^{+0.15}_{-0.00}$ (p)	$2.14^{+0.03}_{-0.03}$	$5.83^{+0.74}_{-0.72}$	$0.109^{+0.025}_{-0.022}$	$-0.988^{+0.883}_{-3.012}$ (p)	1188	0.97	7.4	1.0	0.0
MCG-6-30-15(2)	$0.41^{+0.34}_{-0.00}$ (p)	$2.00^{+0.06}_{-0.04}$	$8.89^{+1.68}_{-0.92}$	$0.144^{+0.040}_{-0.023}$	$0.099^{+0.266}_{-0.289}$	1135	0.89	5.6	0.9	24.7
IC 4329A	$3.76^{+0.54}_{-0.53}$	$1.88^{+0.02}_{-0.03}$	$1.69^{+0.91}_{-1.01}$	$0.020^{+0.042}_{-0.011}$	$0.852^{+0.434}_{-4.852}$ (p)	1666	1.00	5.0	1.3	4.7
NGC 5548	$0.17^{+0.12}_{-0.00}$ (p)	$1.93^{+0.03}_{-0.03}$	$3.09^{+0.85}_{-1.01}$	$0.104^{+0.034}_{-0.046}$	$-0.102^{+0.455}_{-3.898}$ (p)	1228	0.85	5.5	0.9	3.8
Mrk 841(1)	$0.22^{+0.28}_{-0.00}$ (p)	$1.88^{+0.06}_{-0.07}$	$0.99^{+2.46}_{-0.67}$ (p)	$0.023^{+0.056}_{-0.020}$	$1.233^{+0.679}_{-1.183}$	810	0.94	1.7	1.0	5.6
Mrk 841(2)	$0.22^{+0.37}_{-0.00}$ (p)	$1.65^{+0.08}_{-0.07}$	$0.68^{+1.56}_{-0.36}$ (p)	$0.044^{+0.081}_{-0.037}$	$1.349^{+0.358}_{-0.552}$	390	0.25	1.4	0.9	12.7
NGC 6814(1)	$2.23^{+1.77}_{-1.25}$ (p)	$1.78^{+0.29}_{-0.16}$	$0.32^{+624.71}_{-0.00}$ (p)	$0.055^{+9.945}_{-0.054}$ (p)	$2.910^{+0.662}_{-6.910}$ (p)	154	0.01	0.1	0.9	7.3
Mrk 509	$0.42^{+0.20}_{-0.00}$ (p)	$1.97^{+0.03}_{-0.01}$	$0.82^{+0.27}_{-0.38}$	$0.010^{+0.057}_{-0.009}$ (p)	$-4.000^{+6.065}_{-0.000}$ (p)	1312	0.54	4.4	0.9	0.0
NGC 7469(2)	$0.72^{+0.25}_{-0.19}$	$2.02^{+0.04}_{-0.05}$	$129.69^{+175.59}_{-105.60}$	$7.952^{+2.048}_{-4.732}$ (p)	$-0.116^{+0.507}_{-3.884}$ (p)	988	0.46	2.3	1.1	2.1
MCG-2-58-22	$0.42^{+0.45}_{-0.08}$ (p)	$1.73^{+0.09}_{-0.07}$	$105.56^{+263.59}_{-85.72}$	$5.732^{+4.268}_{-3.788}$ (p)	$-0.084^{+0.613}_{-3.916}$ (p)	920	0.95	1.1	1.0	1.0

NOTE.— As for Tables 3–6, except error bars on the fit parameters are 68 per cent confidence limits for 5 interesting parameters ($dof = N_{pts} - 10$), Ω is solid angle subtended by the emitting gas at the central source, and $F(\frac{C_i}{B_i})$ is the F -statistic for model $C(i)$ versus $B(i)$.

TABLE 8
MODEL $C(ii)$: RESULTS FOR AN IONIZED ABSORBER AND AN IONIZED EMITTER (SEE §5.3)

Name	$N_{H,0}$ (10^{21} cm $^{-2}$)	Γ	$N_{H,z}$ (10^{21} cm $^{-2}$)	U_X	$\log D_f$	$\log(\Omega/4\pi)$	χ^2_{Cii}	P_{Cii}	$\frac{\Delta\chi^2_{0.6}}{\Delta N_{0.6}}$	$\overline{R}_{0.6}$	$F(\frac{Cii}{Bii})$	$F(\frac{Cii}{Ci})$
Mrk 335	$0.40^{+0.62}_{-0.00}$ (p)	$2.41^{+0.37}_{-0.42}$	$74.27^{+556.69}_{-42.94}$ (p)	$0.217^{+1.462}_{-0.216}$ (p)	$-0.104^{+0.104}_{-0.160}$ (p)	$1.742^{+0.328}_{-5.742}$ (p)	629	0.40	5.6	0.9	2.0	3.4
Fairall 9	$0.39^{+0.24}_{-0.09}$ (p)	$2.02^{+0.21}_{-0.07}$	$630.96^{+0.00}_{-629.23}$ (p)	$1.048^{+10.172}_{-1.047}$ (p)	$0.000^{+0.000}_{-0.154}$ (p)	(u)	1221	0.96	3.7	0.9	1.9	3.7
3C 120	$1.79^{+0.12}_{-0.10}$	$2.04^{+0.04}_{-0.03}$	$630.96^{+0.00}_{-306.48}$ (p)	$0.178^{+1.092}_{-0.177}$ (p)	$-0.057^{+0.057}_{-0.097}$ (p)	$0.777^{+0.708}_{-4.777}$ (p)	1139	0.51	9.6	0.8	6.5	28.9
NGC 3227	$0.22^{+1.09}_{-0.00}$ (p)	$1.65^{+0.05}_{-0.05}$	$5.00^{+3.07}_{-1.78}$	$0.009^{+0.039}_{-0.003}$	$-1.013^{+0.580}_{-4.987}$	$0.789^{+0.081}_{-4.789}$ (p)	1173	0.68	3.1	0.8	2.0	0.0
NGC 3516	$0.50^{+0.20}_{-0.16}$	$1.92^{+0.03}_{-0.03}$	$8.72^{+0.90}_{-0.79}$	$0.107^{+0.018}_{-0.015}$	$-6.000^{+4.959}_{-0.000}$ (p)	$-1.093^{+0.454}_{-2.907}$ (p)	1400	1.00	2.5	1.0	0.0	0.0
NGC 3783(1)	$1.62^{+0.54}_{-0.58}$	$1.83^{+0.08}_{-0.08}$	$23.77^{+4.45}_{-2.61}$	$0.149^{+0.029}_{-0.019}$	$-6.000^{+0.000}_{-0.000}$ (p)	$0.178^{+0.079}_{-0.516}$	1104	0.86	0.5	0.9	16.3	0.0
NGC 3783(2)	$1.16^{+0.40}_{-0.29}$ (p)	$1.80^{+0.08}_{-0.08}$	$23.21^{+3.24}_{-0.80}$	$0.162^{+0.021}_{-0.028}$	$-6.000^{+0.000}_{-0.000}$ (p)	$-0.119^{+0.296}_{-0.749}$	1076	0.88	0.8	0.9	10.5	0.0
NGC 4051	$0.13^{+0.22}_{-0.00}$ (p)	$2.19^{+0.06}_{-0.07}$	$74.23^{+82.08}_{-31.62}$	$0.817^{+0.431}_{-0.212}$	$-0.170^{+0.082}_{-0.135}$	$0.553^{+0.245}_{-0.200}$	1102	0.98	3.3	1.1	68.4	20.1
NGC 4151(2)	$0.21^{+0.67}_{-0.00}$ (p)	$1.51^{+0.11}_{-0.10}$	$43.46^{+3.15}_{-3.43}$	$0.060^{+0.009}_{-0.009}$	$-1.353^{+0.072}_{-0.067}$	$0.277^{+0.495}_{-4.277}$	866	0.93	1.9	0.8	1.9	117.4
NGC 4151(4)	$0.43^{+0.68}_{-0.22}$ (p)	$1.49^{+0.11}_{-0.11}$	$66.88^{+5.21}_{-5.72}$	$0.080^{+0.016}_{-0.015}$	$-1.321^{+0.059}_{-0.056}$	$0.642^{+0.295}_{-0.898}$	1476	0.53	3.5	0.8	10.0	232.5
NGC 4151(5)	$0.21^{+0.61}_{-0.00}$ (p)	$1.56^{+0.12}_{-0.07}$	$63.39^{+4.73}_{-3.58}$	$0.065^{+0.014}_{-0.016}$	$-1.432^{+0.053}_{-0.045}$	$0.400^{+0.328}_{-4.400}$ (p)	1340	0.96	2.6	1.0	3.7	283.4
Mrk 766	$0.18^{+0.45}_{-0.00}$ (p)	$2.14^{+0.13}_{-0.09}$	$13.04^{+9.87}_{-7.64}$	$0.103^{+0.097}_{-0.036}$	$-0.355^{+0.078}_{-5.645}$	$0.409^{+0.590}_{-4.409}$	1083	0.01	3.7	0.9	5.5	2.2
NGC 4593	$0.51^{+0.20}_{-0.31}$ (p)	$2.02^{+0.05}_{-0.05}$	$2.02^{+1.23}_{-0.32}$	$0.091^{+0.075}_{-0.084}$	$-6.000^{+0.000}_{-0.000}$ (p)	$-4.000^{+4.777}_{-0.000}$ (p)	1343	0.63	3.1	1.1	1.0	1.0
MCG-6-30-15(1)	$0.41^{+0.18}_{-0.00}$ (p)	$2.14^{+0.03}_{-0.03}$	$5.86^{+0.83}_{-0.81}$	$0.110^{+0.028}_{-0.025}$	$-6.000^{+0.000}_{-0.000}$ (p)	$-1.062^{+1.001}_{-2.938}$	1188	0.97	7.4	1.0	0.0	0.0
MCG-6-30-15(2)	$0.43^{+0.34}_{-0.02}$ (p)	$2.00^{+0.06}_{-0.04}$	$8.92^{+1.77}_{-1.11}$	$0.145^{+0.041}_{-0.028}$	$-6.000^{+0.000}_{-0.000}$ (p)	$0.118^{+0.262}_{-0.351}$	1135	0.89	5.1	1.0	24.7	0.0
IC 4329A	$3.79^{+0.06}_{-0.57}$	$1.88^{+0.02}_{-0.03}$	$1.57^{+1.10}_{-1.25}$	$0.016^{+0.040}_{-0.008}$	$-6.000^{+0.000}_{-0.000}$ (p)	$-0.914^{+0.358}_{-3.086}$	1666	1.00	5.4	1.4	4.7	0.0
NGC 5548	$1.05^{+0.25}_{-0.18}$	$1.95^{+0.04}_{-0.04}$	$630.96^{+0.00}_{-70.69}$ (p)	$2.000^{+0.156}_{-0.419}$	$0.000^{+0.000}_{-0.017}$ (p)	(u)	1206	0.73	14.8	1.3	25.4	21.5
Mrk 841(1)	$0.22^{+0.16}_{-0.00}$ (p)	$1.89^{+1.13}_{-0.08}$	$3.65^{+15.71}_{-2.91}$	$0.023^{+0.046}_{-0.020}$	$-0.154^{+0.154}_{-5.846}$ (p)	$1.660^{+0.003}_{-0.579}$	809	0.94	1.8	1.0	6.5	0.0
Mrk 841(2)	$0.22^{+0.47}_{-0.00}$ (p)	$1.64^{+0.32}_{-0.07}$	$1.83^{+629.13}_{-1.51}$ (p)	$0.029^{+0.573}_{-0.025}$	$-0.131^{+0.131}_{-0.058}$	$1.697^{+1.167}_{-5.697}$	390	0.25	1.2	0.9	6.3	0.0
NGC 6814(1)	$2.82^{+1.43}_{-1.84}$ (p)	$1.78^{+0.23}_{-0.18}$	$0.32^{+630.64}_{-0.00}$ (p)	$0.052^{+9.948}_{-0.051}$ (p)	$0.000^{+0.000}_{-6.000}$ (p)	(u)	154	0.01	0.1	0.9	7.8	0.0
Mrk 509	$0.98^{+0.26}_{-0.19}$	$2.01^{+0.07}_{-0.05}$	$630.96^{+0.00}_{-407.14}$ (p)	$1.573^{+893}_{-0.890}$	$-0.006^{+0.006}_{-0.055}$ (p)	(u)	1297	0.43	3.3	1.0	15.1	15.1
NGC 7469(2)	$1.05^{+0.31}_{-0.33}$	$2.14^{+0.09}_{-0.09}$	$588.17^{+42.79}_{-410.42}$ (p)	$1.177^{+0.500}_{-1.176}$ (p)	$0.000^{+0.000}_{-0.104}$ (p)	(u)	973	0.32	2.0	1.1	6.1	15.3
MCG-2-58-22	$0.77^{+4.70}_{-0.43}$ (p)	$1.91^{+2.75}_{-0.17}$	$265.64^{+365.32}_{-214.35}$	$0.579^{+1.475}_{-0.578}$ (p)	$0.000^{+0.000}_{-0.259}$ (p)	(u)	913	0.94	1.3	0.9	0.1	6.5

NOTE.— As for Tables 3–6, except error bars on the fit parameters are 68 per cent confidence limits for 6 interesting parameters, ($dof = N_{pts} - 11$), Ω is solid angle subtended by the emitting gas at the central source, $F(\frac{Cii}{Bii})$ is the F -statistic for model $C(ii)$ versus $B(ii)$, and $F(\frac{Cii}{Ci})$ is that for model $C(ii)$ versus $C(i)$. (u) indicates that meaningful constraints on Ω could not be obtained ($0 \leq \Omega/4\pi \leq 10$).

TABLE 9
ADDITIONAL EDGE FITS (SEE §6.2)

Name	$N_{H,0}$ (10^{21} cm $^{-2}$)	Γ	$N_{H,z}$ (10^{21} cm $^{-2}$)	U_X	E_{ONe} (eV)	τ_{ONe}	χ^2_{ONe}	P_{ONe}	$\frac{\Delta\chi^2_{0.6}}{\Delta N_{0.6}}$	$\overline{R_{0.6}}$	$F(\frac{ONe}{B1})$
NGC 3516	$0.29^{+0.15}_{-0.00}$ (p)	$1.86^{+0.03}_{-0.02}$	$4.97^{+0.92}_{-0.68}$	$0.056^{+0.020}_{-0.010}$	853^{+17}_{-16}	$0.32^{+0.07}_{-0.07}$	1283	1.00	2.2	1.0	105.0
NGC 3783(1)	$1.09^{+0.38}_{-0.22}$ (p)	$1.75^{+0.07}_{-0.06}$	$16.43^{+4.18}_{-3.19}$	$0.119^{+0.028}_{-0.027}$	953^{+29}_{-33}	$0.50^{+0.19}_{-0.16}$	1065	0.60	0.6	0.9	68.4
NGC 3783(2)	$0.87^{+0.14}_{-0.00}$ (p)	$1.71^{+0.07}_{-0.06}$	$14.74^{+3.52}_{-3.06}$	$0.129^{+0.019}_{-0.021}$	888^{+39}_{-36}	$0.57^{+0.23}_{-0.21}$	1025	0.52	0.8	1.0	61.9
MCG-6-30-15(1)	$0.41^{+0.08}_{-0.0}$ (p)	$2.13^{+0.03}_{-0.04}$	$4.43^{+1.00}_{-0.02}$	$0.086^{+0.024}_{-0.023}$	862^{+225}_{-35}	$0.14^{+0.08}_{-0.08}$	1166	0.92	7.1	1.0	20.8
MCG-6-30-15(2)	$0.41^{+0.07}_{-0.0}$ (p)	$2.02^{+0.04}_{-0.05}$	$7.90^{+1.46}_{-1.32}$	$0.141^{+0.026}_{-0.026}$	947^{+48}_{-139}	$0.14^{+0.13}_{-0.08}$	1138	0.90	5.4	1.0	21.8

NOTE.— As for Table 5, except error bars on the fit parameters are 68 per cent confidence limits for 6 interesting parameters ($dof = N_{pts} - 11$), τ_{ONe} is the optical depth of the additional absorption edge required at a (rest-frame) energy of E_{ONe} , and $F(\frac{ONe}{B1})$ is the F -statistic for χ^2_{ONe} and χ^2_{B1} .

TABLE 10
POWERLAW AND PARTIALLY-COVERED IONIZED ABSORBER + EMITTER FITS WITH REFLECTION (SEE §6.4.1)

Name	$N_{H,0}$ (10^{21} cm $^{-2}$)	Γ	$N_{H,z}^*$ (10^{21} cm $^{-2}$)	U_X	$\log D_J$	$\log(\Omega/4\pi)$	\mathcal{F}	χ_{cr}^2	P_{cr}	$\frac{\Delta\chi_{0.6}^2}{\Delta N_{0.6}}$	$\overline{R_{0.6}}$	$F(\frac{cr}{C_{ii}})$
Mrk 335	$0.40^{+0.22}_{-0.00}$ (p)	$2.29^{+0.10}_{-0.08}$	$21.58^{+6.60}_{-13.42}$	$1.218^{+1.057}_{-0.538}$	$-0.700^{+0.340}_{-5.300}$ (p)	$-0.005^{+0.485}_{-0.986}$	$3.8^{+2.2}_{-2.3}$	619	0.30	2.5	1.1	10.6
NGC 3783(2)	$1.81^{+0.63}_{-0.70}$	$2.01^{+0.20}_{-0.19}$	$25.15^{+5.17}_{-4.39}$	$0.281^{+0.053}_{-0.053}$	$-6.000^{+4.678}_{-0.000}$ (p)	$0.103^{+0.307}_{-0.546}$	$2.4^{+4.2}_{-2.05}$	1069	0.85	1.2	1.1	17.22
NGC 4051	$0.13^{+0.51}_{-0.00}$ (p)	$2.37^{+0.23}_{-0.09}$	$10.38^{+5.11}_{-2.91}$	$0.372^{+0.128}_{-0.094}$	$-1.918^{+0.252}_{-4.082}$	$0.221^{+0.249}_{-0.151}$	$3.8^{+4.0}_{-1.8}$	1077	0.95	1.6	1.0	23.3
NGC 4593	$1.10^{+0.44}_{-0.37}$	$2.32^{+0.17}_{-0.16}$	$4.42^{+2.48}_{-1.85}$	$0.186^{+0.095}_{-0.084}$	$-2.722^{+0.001}_{-3.278}$ (p)	$-4.000^{+4.068}_{-0.000}$ (p)	$4.5^{+3.3}_{-2.3}$	1299	0.31	4.4	1.1	44.9
MCG-6-30-15(1)	$0.41^{+0.39}_{-0.00}$ (p)	$2.35^{+0.19}_{-0.17}$	$10.22^{+2.67}_{-3.38}$	$0.056^{+0.023}_{-0.015}$	$-0.583^{+0.088}_{-0.323}$	$-4.000^{+4.154}_{-0.000}$ (p)	$2.6^{+2.5}_{-1.9}$	1176	0.95	7.6	1.0	11.2
MCG-6-30-15(2)	$0.41^{+0.79}_{-0.00}$ (p)	$2.41^{+0.41}_{-0.25}$	$16.59^{+4.79}_{-3.89}$	$0.069^{+0.035}_{-0.019}$	$-0.665^{+0.070}_{-0.060}$	$-0.585^{+1.234}_{-3.415}$ (p)	$4.8^{+7.5}_{-3.2}$	1123	0.84	7.7	0.9	11.5
IC 4329A	$4.28^{+0.44}_{-0.46}$	$2.23^{+0.16}_{-0.13}$	$5.62^{+2.04}_{-1.37}$	$0.145^{+0.083}_{-0.055}$	$-2.893^{+2.541}_{-3.107}$	$-0.993^{+0.171}_{-3.007}$ (p)	$4.3^{+2.5}_{-1.7}$	1568	1.00	4.0	1.2	166.8
NGC 5548	$0.90^{+0.48}_{-0.47}$	$2.29^{+0.21}_{-0.16}$	$6.22^{+2.92}_{-1.99}$	$0.192^{+0.085}_{-0.065}$	$-2.733^{+0.336}_{-3.267}$ (p)	$0.088^{+0.363}_{-1.066}$	$4.0^{+3.8}_{-2.3}$	1159	0.37	8.2	1.0	47.7
Mrk 509	$0.47^{+0.05}_{-0.68}$	$2.11^{+0.23}_{-0.09}$	$1.66^{+0.37}_{-0.80}$	$0.008^{+0.221}_{-0.003}$	$-0.929^{+0.573}_{-5.071}$ (p)	$0.716^{+1.203}_{-4.716}$ (p)	$2.4^{+3.0}_{-1.4}$	1285	0.34	11.2	0.9	12.2
NGC 7469(2)	$1.46^{+0.71}_{-0.98}$	$2.45^{+0.37}_{-0.27}$	$3.22^{+4.81}_{-2.55}$	$0.200^{+0.259}_{-0.197}$	$-2.909^{+2.909}_{-3.091}$ (p)	$0.207^{+0.015}_{-4.207}$ (p)	$6.9^{+0.9}_{-4.4}$	966	0.29	2.6	1.1	7.7
MCG-2-58-22	$2.19^{+1.01}_{-1.11}$	$2.80^{+0.53}_{-0.78}$	$50.23^{+85.13}_{-41.35}$	$0.377^{+1.388}_{-0.362}$	$-0.255^{+0.191}_{-5.745}$ (p)	$0.181^{+1.004}_{-4.181}$ (p)	$17.5^{+32.5}_{-15.4}$	904	0.91	1.8	0.9	9.4

NOTE.— As for Tables 3–8, except error bars on the fit parameters are 68 per cent confidence limits for 7 interesting parameters ($dof = N_{pts} - 12$, \mathcal{F} is the enhancement of the reflected continuum relative to that expected from a semi-infinite plane illuminated by a point source viewed face-on, and $F(\frac{cr}{C_{ii}})$ is the F -statistic for χ_{cr}^2 and $\chi_{C_{ii}}^2$).

TABLE 11
RESULTS FOR A DOUBLE-POWERLAW PLUS IONIZED ABSORBER AND AN IONIZED EMITTER (SEE §6.4.2)

Name	$N_{H,0}$ (10^{21} cm $^{-2}$)	Γ_s	$R_{s/h}$	Γ_h	$N_{H,z}$ (10^{21} cm $^{-2}$)	U_X	$\log(\Omega/4\pi)$	χ^2_{2p}	P_{2p}	$\frac{\Delta\chi^2_{0.6}}{\Delta N_{0.6}}$	$\overline{R}_{0.6}$	$F(\frac{2p}{C_{ii}})$
Mrk 335	$0.40^{+1.36}_{-0.00}$ (p)	$2.61^{+2.39}_{-1.11}$ (p)	2.9	$1.57^{+0.93}_{-1.57}$ (p)	$16.03^{+45.09}_{-15.71}$ (p)	$1.488^{+8.512}_{-1.487}$ (p)	$0.218^{+1.346}_{-4.218}$ (p)	618	0.29	2.1	1.0	11.3
NGC 4051	$0.74^{+1.53}_{-0.61}$ (p)	$3.41^{+1.59}_{-1.13}$ (p)	1.5	$1.85^{+0.27}_{-1.85}$ (p)	$9.30^{+4.88}_{-7.33}$	$0.312^{+0.174}_{-0.276}$	$0.342^{+0.336}_{-0.406}$	1081	0.95	9.0	0.9	19.5
IC 4329A	$5.29^{+1.13}_{-1.02}$	$3.22^{+0.83}_{-0.95}$	2.9	$1.55^{+0.18}_{-0.69}$	$7.16^{+2.70}_{-2.79}$	$0.161^{+0.067}_{-0.076}$	$-0.290^{+0.621}_{-3.710}$ (p)	1573	1.00	3.9	1.2	77.7
NGC 5548	$1.74^{+0.13}_{-1.15}$	$3.18^{+0.97}_{-0.99}$	3.1	$1.54^{+0.24}_{-0.31}$	$7.38^{+2.90}_{-2.81}$	$0.195^{+0.261}_{-0.134}$	$0.109^{+0.396}_{-0.829}$	1163	0.40	13.5	1.0	43.5

NOTE.— As for Tables 3–8, except error bars on the fit parameters are 68 per cent confidence limits for 7 interesting parameters ($dof = N_{pts} - 12$), Γ_s and Γ_h are the photon indices of the two powerlaws (constrained such that $1.5 \geq \Gamma_s \geq 5.0$ and $0.0 \geq \Gamma_h \geq 2.5$), $R_{s/h}$ is the ratio of the normalization of the soft powerlaw divided by that of the hard powerlaw at 1 keV (in the rest-frame of the source), $F(\frac{2p}{C_{ii}})$ is the F -statistic for model this double-powerlaw model compared to model $C(ii)$.

TABLE 12
SUMMARY OF FITS

Name	$A(i)$	$A(ii)$	Acceptability of Models				Ionized gas ?	Notes & Comments
			$B(i)$	$B(ii)$	$C(i)$	$C(ii)$		
Mrk 335	no	YES †	YES	YES †	YES †	YES †	...	complex continuum (§6.4.2)
Fairall 9	<i>yes</i> ^a	<i>yes</i> ^a	<i>yes</i> ^a	<i>yes</i> ^a	<i>yes</i> ^a	<i>yes</i> ^a	...	see Appendix
3C 120	YES	YES	YES	YES	YES	YES	...	
NGC 3227	no	YES	YES	YES	YES	YES	✓	
NGC 3516	no	no	<i>yes</i> ^{a,c}	<i>yes</i> ^{a,c}	<i>yes</i> ^{a,c}	<i>yes</i> ^{a,c}	✓	
NGC 3783(1)	no	no	YES	YES	YES	YES	✓	see also §7.1
NGC 3783(2)	no	no	YES	YES	YES	YES	✓	see also §7.1
NGC 4051	no	no	no	no	no	no	✓	spectral variability
NGC 4151(2)	no	no	no	YES	no	YES	✓	see also §7.2
NGC 4151(4)	no	no	no	YES	no	YES	✓	see also §7.2
NGC 4151(5)	no	no	no	<i>yes</i> ^{a,c}	no	<i>yes</i> ^{a,c}	✓	see also §7.2
Mrk 766	no	YES	YES ‡	YES ‡	YES ‡	YES ‡	✓	
NGC 4593	<i>yes</i> ^b	YES	YES	YES	YES	YES	✓	
MCG-6-30-15(1)	no	no	<i>yes</i> ^c	<i>yes</i> ^c	<i>yes</i> ^c	<i>yes</i> ^c	✓	see also §7.3
MCG-6-30-15(2)	no	no	<i>yes</i> ^c	<i>yes</i> ^c	YES	YES	✓	see also §7.3
IC 4329A	no	no	no	no	no	no	✓	complex continuum (§6.4)
NGC 5548	no	no	YES	YES	YES †	<i>yes</i> ^b	✓	
Mrk 841(1)	no	no	YES	<i>yes</i> ^{a,b}	YES	YES	✓	see also §7.4
Mrk 841(2)	<i>yes</i> ^b	YES †	YES †	YES †	YES †	YES †	✓	see also §7.4
NGC 6814(1)	YES ‡	YES ‡	YES ‡	YES ‡	YES ‡	YES ‡	...	
Mrk 509	YES	YES	YES	YES	YES	YES	✓	
NGC 7469(2)	YES	YES †	YES †	YES †	YES †	YES †	✓	
MCG-2-58-22	<i>yes</i> ^a	YES	YES	YES	YES	YES	...	
TOTAL	4 + 4	10 + 1	14 + 1	15 + 6	15 + 3	16 + 5	18	

NOTE.— Datasets marked by **YES** satisfy all our criteria for acceptability (see §4.1) for the given model, and the best-fitting values are used in the construction of the hatched histograms in Figs 2, 3, 5, 7 & 11. Datasets denoted by *yes* do not satisfy all the criteria due to: ^a the presence of (random) noise in the data/model residuals beyond that expected from purely statistical considerations; ^b failure to extrapolate < 0.6 keV; ^c the presence of a deficit in counts at ~1 keV (see §6.2). Nevertheless, in many cases the model is possibly still a reasonable description of the data, and the effect of including the best-fitting values shown as the open histograms in Figs 2, 3, 5, 7 & 11. The given model is not considered to offer an acceptable description of the datasets marked 'no'. For each dataset, the boxed model indicates which of the models considered in §5 is not improved at $\geq 99\%$ confidence by the inclusion of additional parameters. Datasets flagged with † have $P(\chi^2 | dof) < 0.5$ (i.e. reduced χ^2 values less than unity) and those flagged with ‡ have $P(\chi^2 | dof) < 0.05$. Further notes on individual objects are given in the Appendix.

Figure Captions

Figure 1: (a) The solid curves give the ratio of the 'X-ray ionization parameter' U_X (eqn. 1) to the more traditional ionization parameter U (defined over the entire Lyman continuum) for the form of the optical–X-ray continua used here (see §3) assuming $\alpha_{ox} = 1.0$ (upper curve) and $\alpha_{ox} = 1.5$ (lower curve). The dashed curves give U_X/U assuming the continuum is a single powerlaw of photon index Γ from 13.6 eV to 13.6 keV (upper curve) and to infinite energies (lower curve). (b) The solid curves give the ratio of U_X to ξ (in units of erg cm s^{-1}), defined as $\xi = L/n_H R^2$, where n_H and R are as in eqn.1, but where L is the integrated luminosity over the 13.6 eV to 13.6 keV band for the form of the optical–X-ray continua used here, assuming $\alpha_{ox} = 1.0$ (upper curve) and $\alpha_{ox} = 1.5$ (lower curve). The dashed curve gives U_X/ξ assuming the continuum is a single powerlaw of photon index Γ from 13.6 eV to 13.6 keV (as used by Reynolds 1997 amongst others). In both panels, the open and filled symbols indicate the corresponding ratios for the optical–X-ray continua given in Mathews & Ferland (1987) and Krolik & Kriss (1995) respectively.

Figure 2: Histograms showing the range of photon index (Γ) of the underlying continua derived assuming the various models described in §5. The histograms are generated by assigning a rectangle of equal area to each dataset, of width determined from the 1σ error bars for that parameter as listed in the relevant table. In all cases the hatched region shows the histogram which formally satisfy all the criteria given in §4.1. The open histogram shows the effect of also including the datasets which just fail to meet our formal criteria but for which the model is considered likely to be applicable (as described in the text and summarized in Table 12).

Figure 3: As for Fig. 2, but for the column density ($N_{H,z}$) of the material at the redshift of the source. It should be remembered that in models $A(i)$ & $A(ii)$, the material is assumed to be neutral, whilst in models $B(i)$ – $C(ii)$ it is photoionized (see §4).

Figure 4: The derived spectrum and the corresponding rebinned, mean data/model ratios for the 8 datasets for which model $A(ii)$ (§5.2; Table 4) is acceptable and offers an improvement at >99% confidence over model $A(i)$. Also shown are the corresponding plots for Fairall 9 and IC 4329A as, although the fits to these 2 datasets fail to satisfy our formal criteria for acceptability, in neither case is the goodness-of-fit significantly improved by the inclusion of the additional parameters in subsequent models presented in §5 (see text). The objects are presented in order of increasing Right Ascension. The observed spectrum, corrected for the effects of Galactic absorption, is shown in the upper panel of each plot as the solid, bold curve. The individual spectral components which contribute to the observed spectrum are also shown, as is the powerlaw (dashed) that would be visible if there was no attenuation along the line-of-sight at the redshift of the source (i.e. if $N_{H,z} = 0$). As

described in §2, for each observation the spectral analysis was performed by simultaneously fitting the mean spectra from all 4 instruments over the 0.6–5.0, 7.0–10.0 keV band. The data/model ratios plotted as filled triangles in the lower panel are the (error-weighted) means of the ratios from the individual detectors within this energy range, rebinned in energy-space for clarity. The open triangles show the corresponding rebinned, mean ratios when the best-fitting model is extrapolated < 0.6 keV and into the 5–7 keV band. It should be noted that significantly superior fits are obtained for more complex models in the case of Mrk 355 (§6.4.2), NGC 3227 & NGC 4593 (§5.3), Mrk 766 (§5.4) and Mrk 509 (§5.6).

Figure 5: As for Fig. 2, but for the fraction of the underlying continuum (D_f) which does not suffer attenuation by material at the redshift of the source.

Figure 6: As for Fig 4, but for the 8 datasets for which model $B(i)$ (§5.3; Table 5) is acceptable and offers an improvement at $>99\%$ confidence over both models $A(i)$ and $A(ii)$. Also shown are the corresponding plots for NGC 3516 and MCG-6-30-15(1) as, although the fits to these 2 datasets fail to satisfy our formal criteria for acceptability, in neither case is the goodness-of-fit significantly improved by the inclusion of the additional parameters in subsequent models presented in §5 (see text). It should be noted that significantly superior fits are obtained for more complex models in the case of NGC 3516 (§6.2), NGC 3783(1,2) (§5.5 & §6.2), Mrk 766 & Mrk 841(2) (§5.4) and Mrk 509 (§5.6).

Figure 7: As for Fig. 2, but for the ionization parameter (U_X) of the photoionized material, as defined by eqn. 1.

Figure 8: The best-fitting values for $N_{H,z}$ and U_X for each of the models including ionized gas considered in §5. Shown are only those datasets for which the model offers an adequate description of the data *and* leads to an improvement at $> 99\%$ over the corresponding model with neutral gas (i.e. model $A(i)$ or $A(ii)$). The solid symbols represent the datasets for which the model satisfies all our criteria for acceptability. The open symbols represent the datasets which do not satisfy our formal criteria, but for which we consider the measurements of $N_{H,z}$ and U_X to be reasonable estimates. Overlaid on each panel are curves showing the $\tau = 0.1$ (solid) and $\tau = 0.3$ (dotted) for OVII and OVIII. As further discussed in §8.5, ionized gas lying in the region of U_X – $N_{H,z}$ plane where $U_X > 10^{-22}N_{H,z}$ has an optical depth $\tau \lesssim 0.1$ for all ions with edges within the *ASCA* bandpass. For the signal-to-noise ratio typical of *ASCA* observations the ionized gas will thus be almost transparent.

Figure 9: As for Fig 4, but for the 5 datasets for which model $B(ii)$ (§5.4; Table 6) is acceptable and offers an improvement at $>99\%$ confidence over both models $A(ii)$ and $B(i)$. Also shown are the corresponding plots for NGC 4151(5) as, although the fit to

this dataset fails to satisfy our formal criteria for acceptability, the goodness-of-fit is not significantly improved by the inclusion of the additional parameters in subsequent models presented in §5 (see text). It should be noted that significantly superior fits are obtained for more complex models in the case of NGC 3783(1) (§5.5 & §6.2), NGC 4151(4) (§5.6) and Mrk 509 (§5.6).

Figure 10: As for Fig 4, but for the 4 datasets for which model $C(i)$ (§5.5; Table 7) is acceptable and offers an improvement at >99% confidence over both models $B(i)$ and $B(ii)$.

Figure 11: As for Fig. 2, but for the solid angle (Ω) subtended by the ionized gas at the origin of the illuminating continuum.

Figure 12: As for Fig 4, but for the 4 datasets for which model $C(ii)$ (§5.6; Table 8) is acceptable and offers an improvement at >99% confidence over both models $B(ii)$ and $C(i)$. It should be noted that NGC 4051 and NGC 5548 fail to satisfy all our formal criteria for acceptability assuming model $C(ii)$. Furthermore it should be noted that in the case of NGC 5548 the model predicts a stronger Fe $K\alpha$ emission than observed. Caution is urged in when interpreting these results for NGC 4051, NGC 5548 and Mrk 509 as the best-fitting solutions are really only indicative of relatively subtle curvature in the observed spectrum. Such curvature can arise as a result of curvature in the underlying continuum, spectral variability during the observation, and/or additional spectral components (see text and §6.4).

Figure 13: The mean data/model ratios (in the *observer's* frame) in the SIS and GIS for the 16 datasets satisfying our criteria for acceptability assuming model $C(ii)$. This plot was constructed by taking the error-weighted average of the individual data/model ratios for each detector from each of the appropriate observations. These averages were then rebinned for display purposes. Caution is urged when interpreting such plots. They potentially contain artificial features introduced by time-dependent errors in the calibration of the instruments (such as slight offsets in the gain of the detectors at the time of each observation), along with real features due to errors in the calibration of the instrument, as well as of astrophysical origin. Furthermore such plots are dominated by the datasets with the highest signal-to-noise ratio.

Figure 14: The mean data/model ratios in the 3–10 keV band (source frame) obtained in Paper II, and for models $B(ii)$, $C(i)$ and $C(ii)$ presented here. The corresponding profile assuming model $B(i)$ is almost identical to that assuming model $B(ii)$ and hence is not shown. The y -axis for each panel covers the same dynamic range. As described in the text, the 5–7 keV band is excluded from the spectral analysis presented here. The profiles were constructed from those datasets which satisfy our criteria for acceptability (§4.1) assuming

the best-fitting model and using the SIS data (only). The vertical, dotted line shows the location of the $K\alpha$ fluorescent line from neutral Fe (6.4 keV). There are naturally slight differences between the profiles, in particular in the case of models $C(i)$ & $C(ii)$ (which include Fe line-emission for the photoionized-emitter). However it can be seen that the profiles obtained from the analysis presented here have the same characteristics of the profile found in Paper-II. Specifically, the peak of the line is consistent with that expected from FeI, the wings of the profile show a significant breath (the FWHM of the instrumental resolution is ~ 0.12 keV at these energies), the profile appears asymmetric with more flux in the low-energy wing. The implications are of such a profile in the context of models in which it is due to emission from the innermost regions of an accretion disk are discussed in detail in Paper-II.

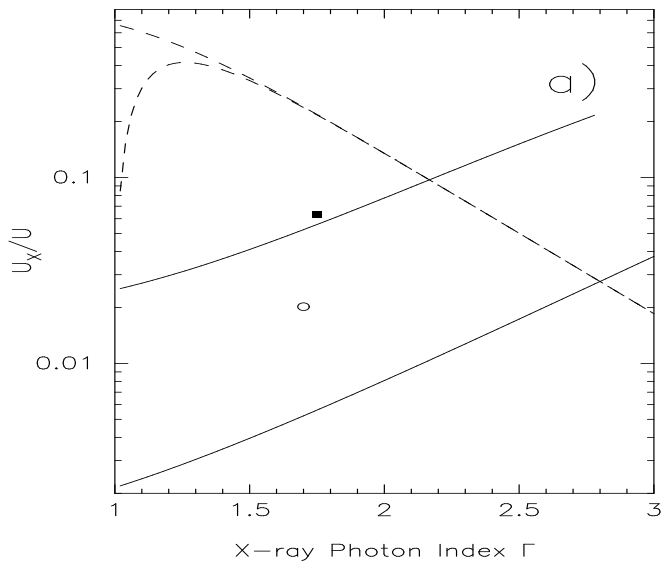
Figure 15: As for Fig 4, but for the 4 datasets for which the double-powerlaw model (§6.4.2; Table 11) provides a significant improvement over the fit obtained assuming model $C(ii)$ and in which both powerlaws of similar importance over a sizable fraction of the *ASCA* bandpass. As described in the text, the goodness-of-fit of 6 other datasets are also significantly improved assuming such a model. However in these cases the second powerlaw component makes a significant contribution only at either the very lowest or very highest energies. It should be noted that best-fitting solution to IC 4329A fails to satisfy our formal criteria for acceptability.

Figure 16: The solid contours show the 90% confidence limits (for 6 interesting parameters) in the $N_{H,z}$ - U_X plane for the individual observations of NGC 3783, NGC 4151 and MCG-6-30-15 assuming model $C(ii)$. The dashed contours show the corresponding limits for NGC 4151 when the optically thin plasma with $kT \sim 0.7$ keV is also included in the spectral model (§6.4.3). The dotted curves show the optical depths of the OVII and OVIII edges in this region of parameter-space. The implications of the changes in the state of the ionized gas in each source, particularly with regard to the corresponding behaviour of the illuminating continuum, is discussed in §7.

Figure 17: The derived continuum luminosity, L_X , in the 0.1–10 keV band (after correcting for absorption) versus the parameters of the ionized gas assuming model $C(ii)$. The solid symbols represent the datasets for which the model satisfies all our criteria for acceptability. The open symbols represent the datasets which do not satisfy our formal criteria, but for which we consider the measurements of $N_{H,z}$ and U_X to be reasonable estimates. As can be seen from the upper panel, there is no clear relation between $N_{H,z}$ and L_X . However from the lower panel it can be seen that there is some indication that $U_X \propto L_X$, which would have implications for the distribution of gas in these sources. However it should be noted that the majority of the sources considered here in which U_X

is well constrained cover only a decade in luminosity (10^{43} – 10^{44} erg s $^{-1}$). The addition of the two quasars PG 1114+445 and MR 2251-178 to the plot argues against any obvious relation between U_X and L_X (see §8.5).

Figure 18: The column density, $N_{H,z}$, derived assuming model $C(ii)$ versus the mean ratio of the flux observed at 125 nm to that at 220 nm, $(f_{125}/f_{220})_{obs}$ (from Table 1). It can be seen that the majority of sources are consistent with $2 \lesssim (f_{125}/f_{220})_{obs} \lesssim 5$, whilst 3 datasets (NGC 3227, MCG-6-30-15(1,2)) have values a factor ~ 10 lower. Clearly $(f_{125}/f_{220})_{obs} = (f_{125}/f_{220})_{int} e^{-\Delta\tau}$, where $(f_{125}/f_{220})_{int}$ is the intrinsic flux ratio, and $\Delta\tau$ ($= \tau_{125} - \tau_{220}$) the difference in optical depths at 125 nm and 220 nm. We stress that $(f_{125}/f_{220})_{int}$ is not necessarily a good indication of the underlying UV continuum (see text). The curves show $(f_{125}/f_{220})_{obs}$ assuming $(f_{125}/f_{220})_{int} = 3.1$ and (from top to bottom) $\Delta\tau = 0.0, 0.005N_{21}, 0.05N_{21}$ (dotted) and $\Delta\tau = 0.5N_{21}$ (dashed), where $N_{21} = N_{H,z}/10^{21}$. It can be seen that NGC 3227 and MCG-6-30-15(1,2) are consistent with $(f_{125}/f_{220})_{int}$ similar to the other sources if their fluxes at 125 nm and 220 nm are absorbed by a column density similar to that observed in the X-ray band and $\Delta\tau = 0.5N_{21}$. A comparison of such a value of $\Delta\tau$ with that expected from 'standard' dust models is provided in the text.



- 94 -

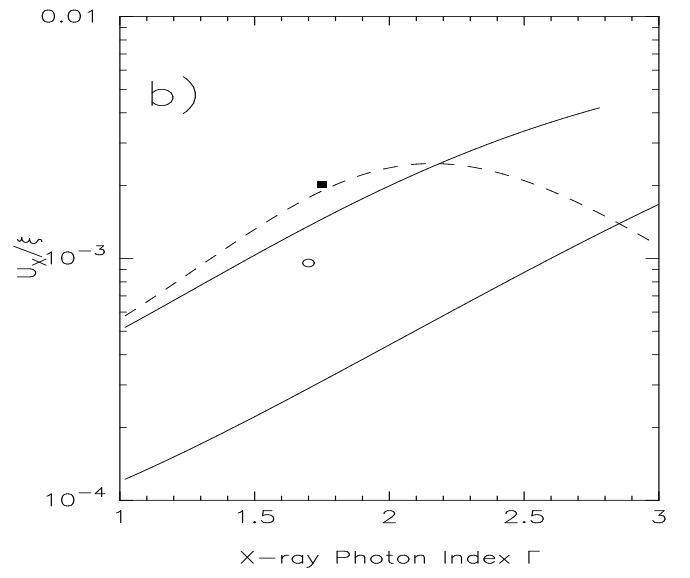


Fig. 1.—

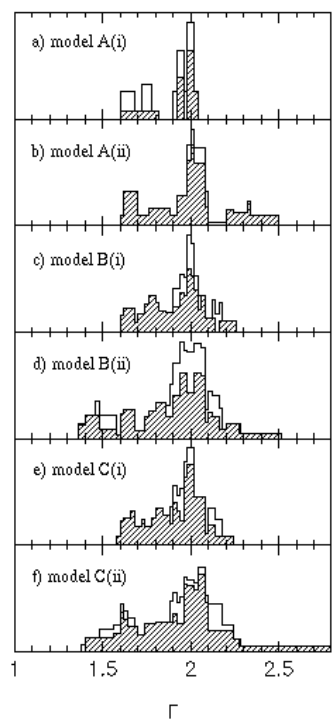


Fig. 2.—

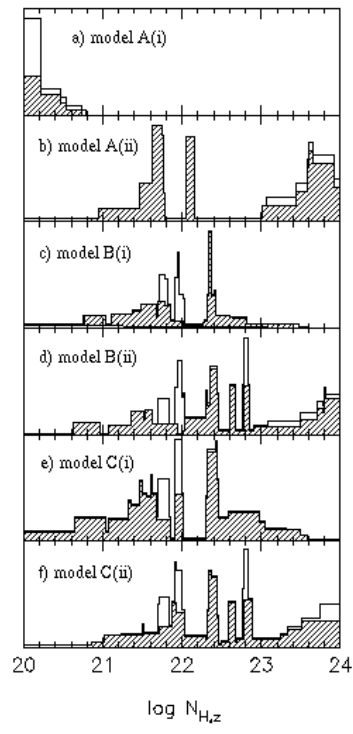


Fig. 3.—

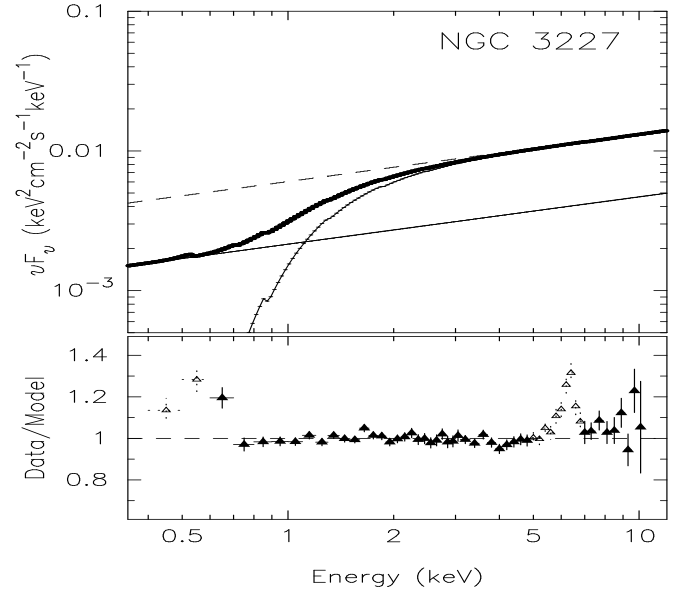
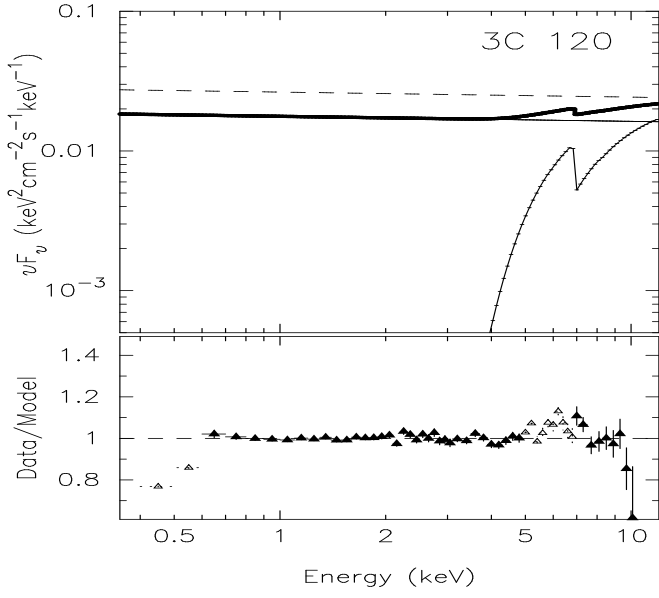
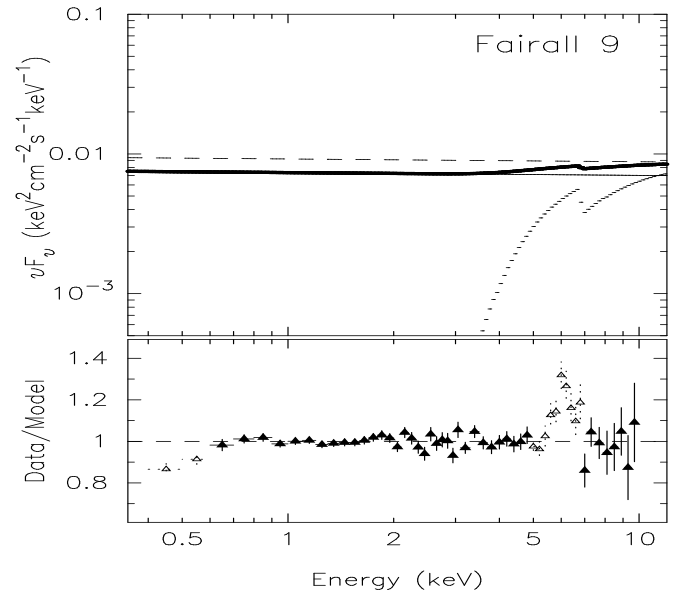
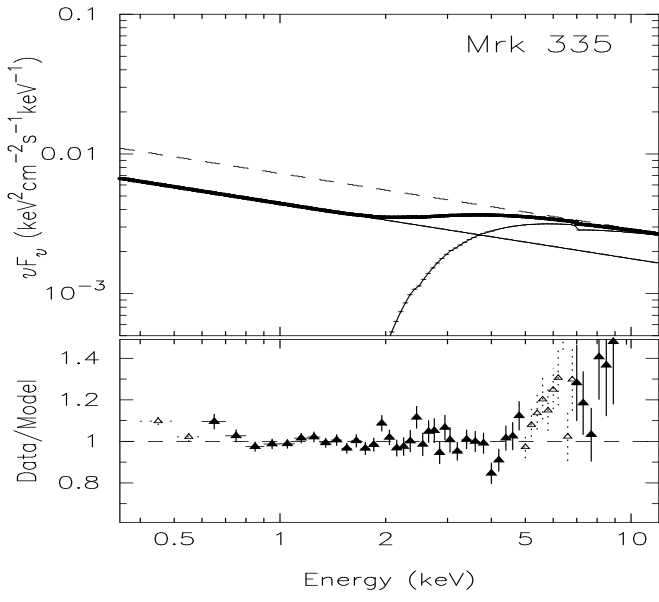


Fig. 4.—

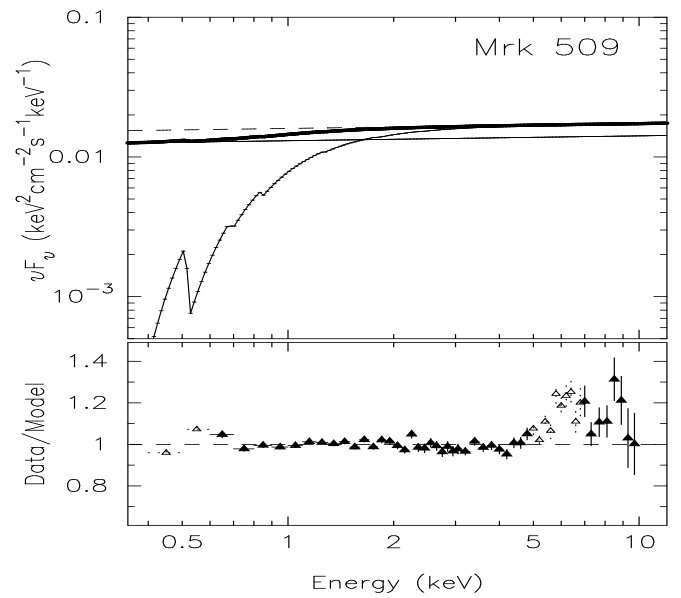
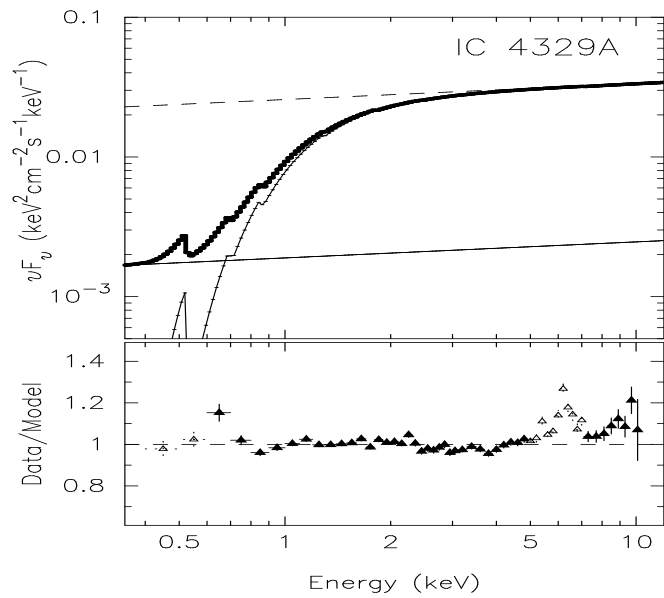
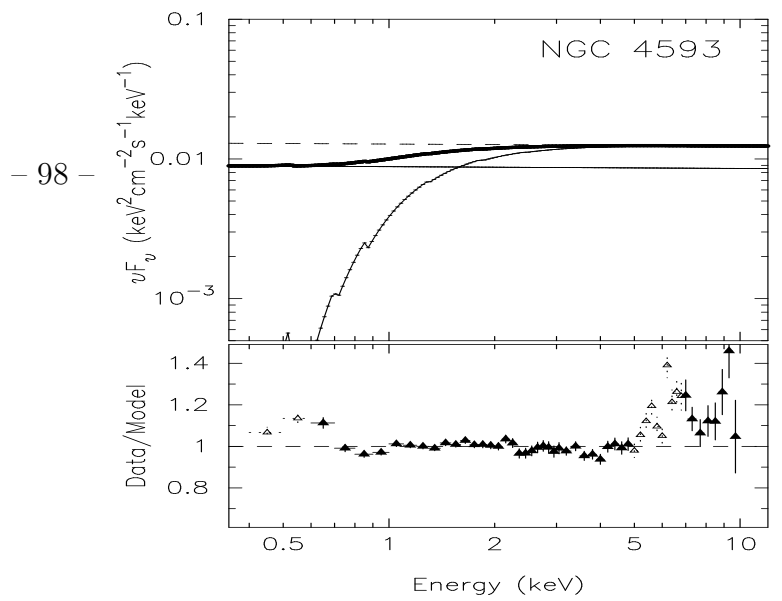
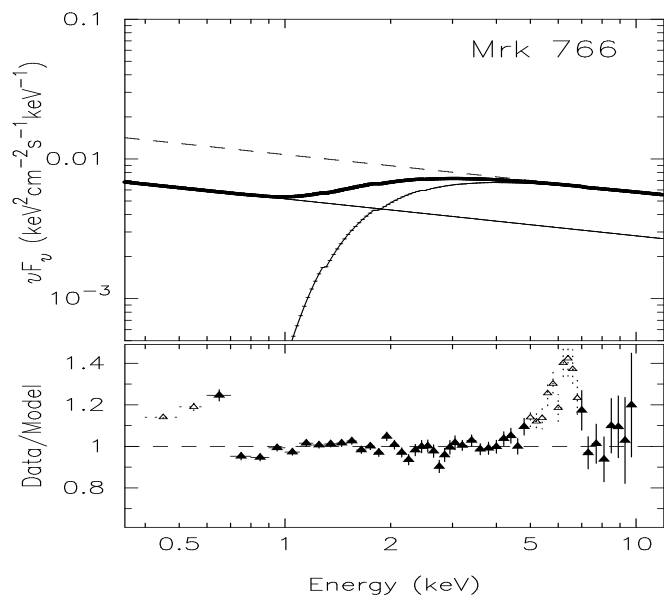


Fig. 4.— *continued*

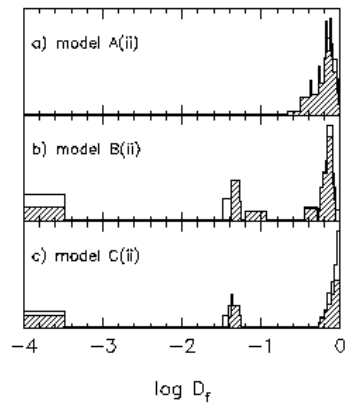


Fig. 5.—

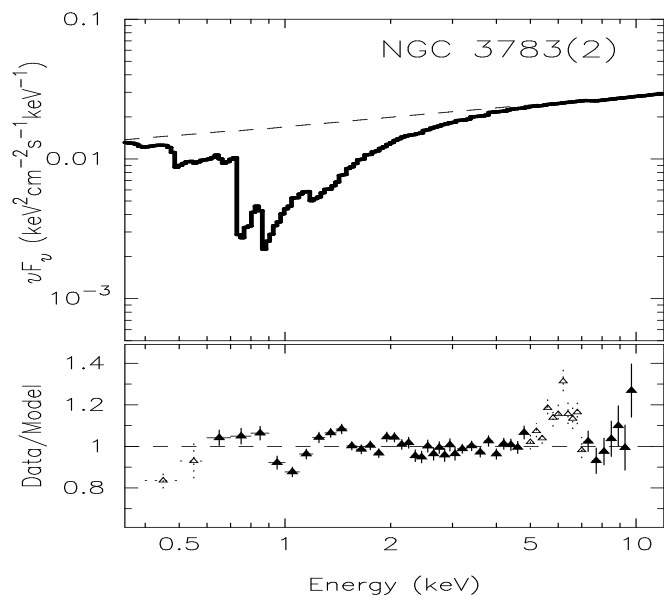
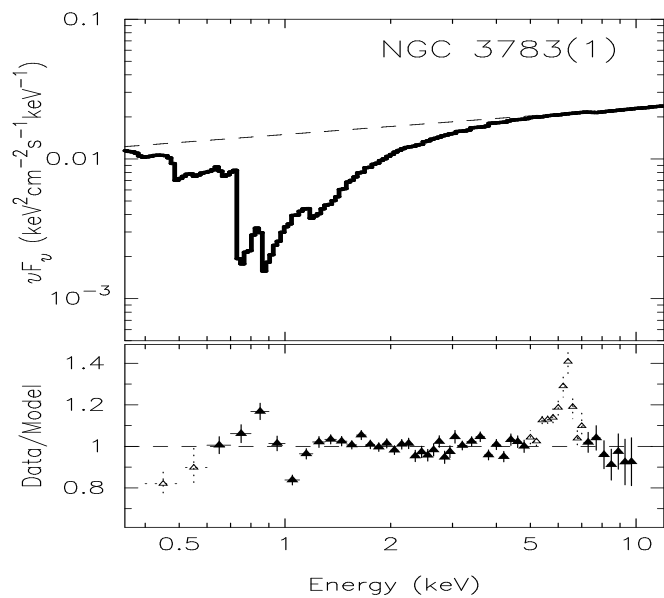
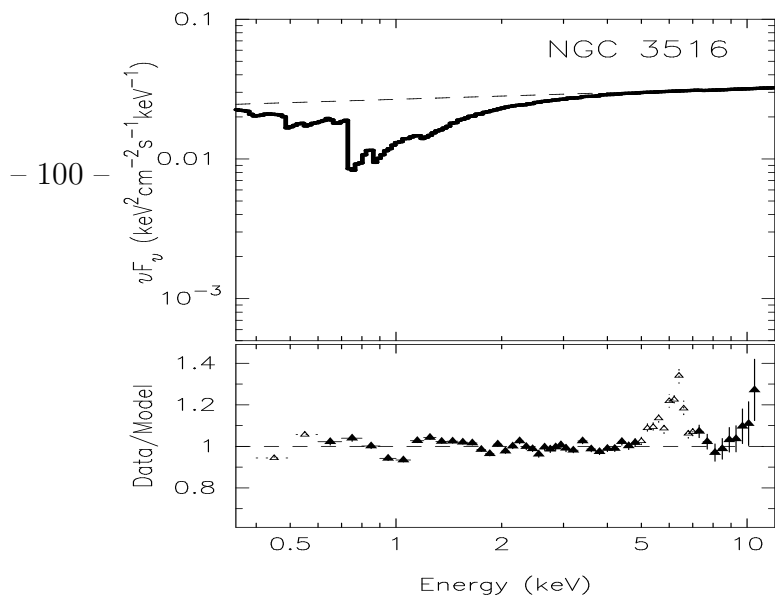
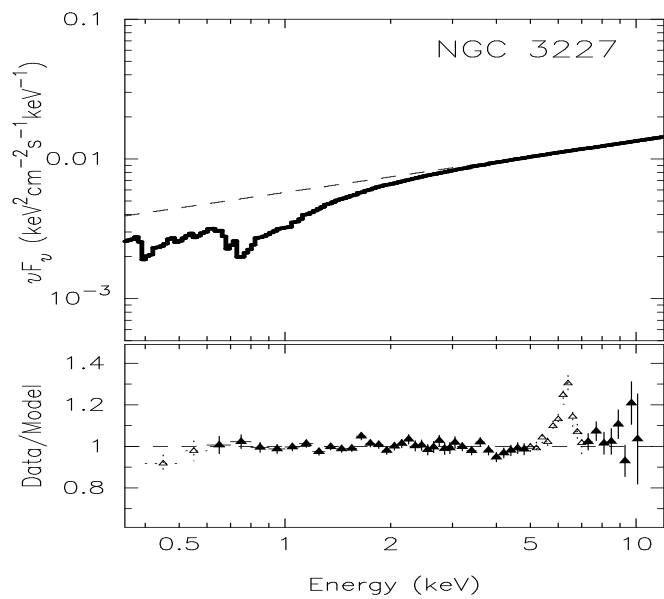


Fig. 6.—

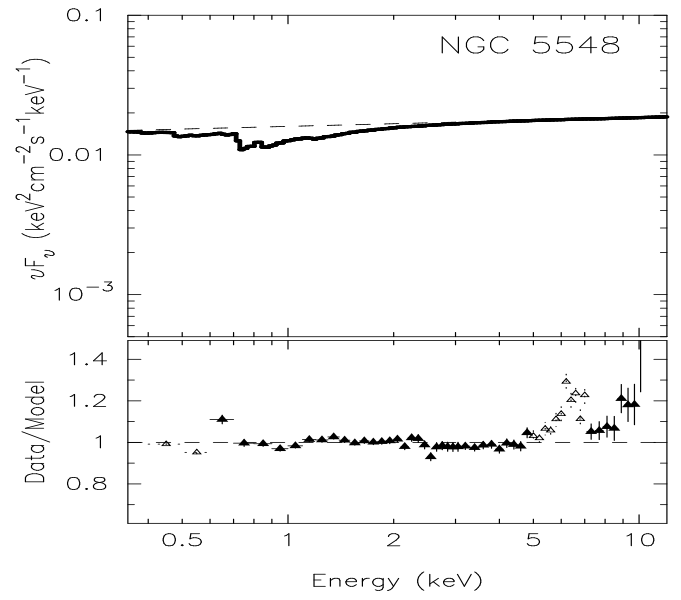
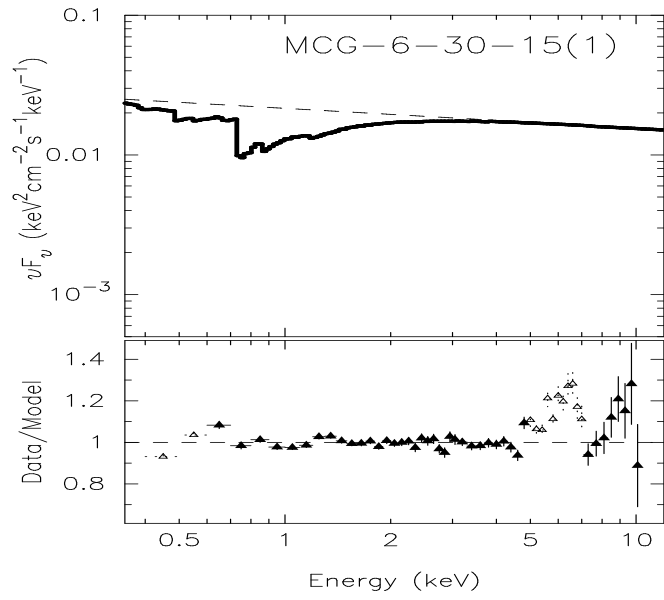
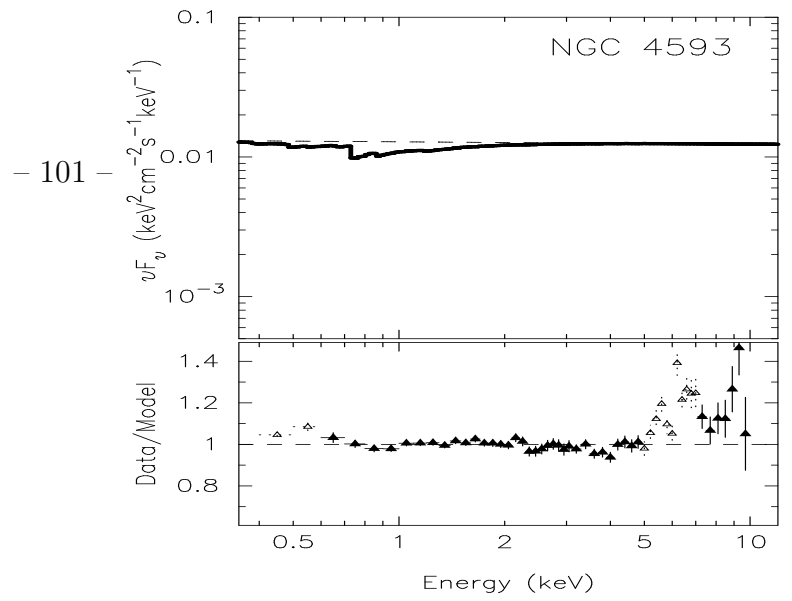
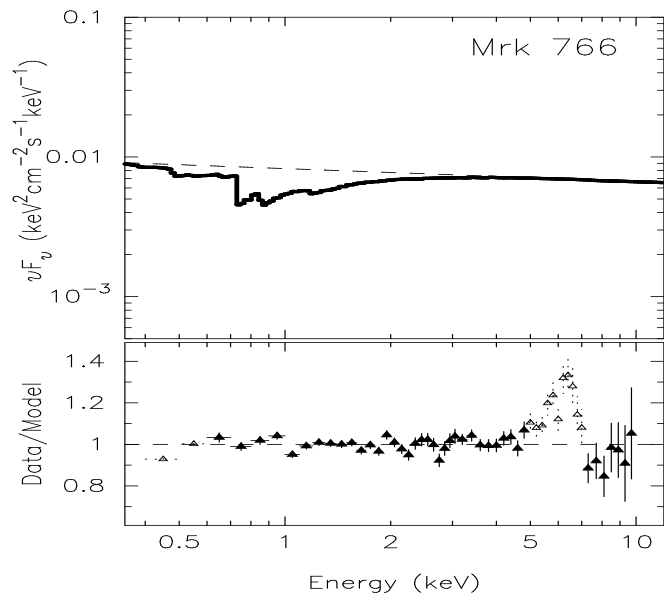


Fig. 6.— *continued*

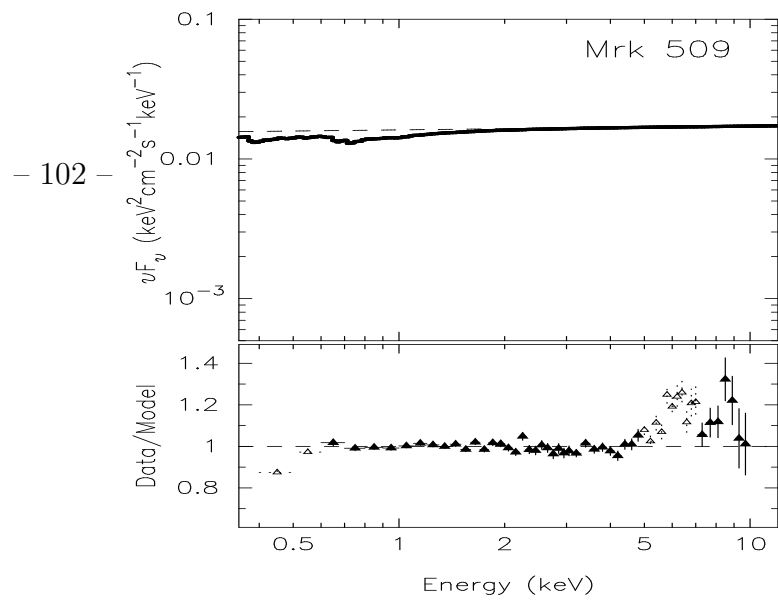
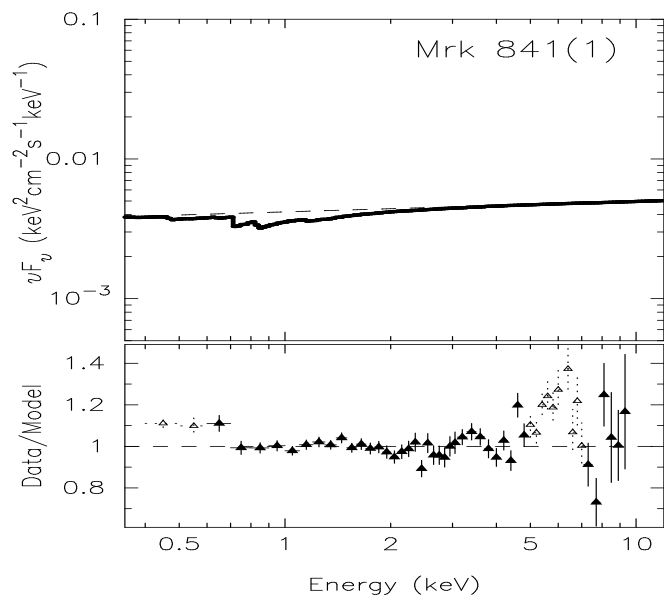


Fig. 6.— *continued*

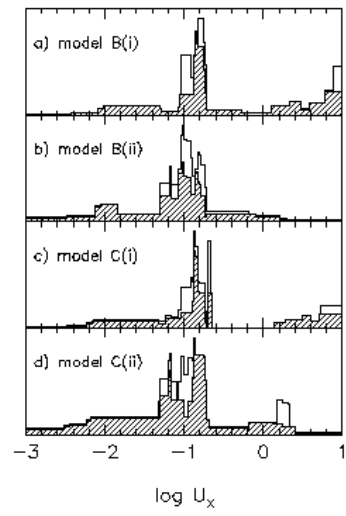


Fig. 7.—

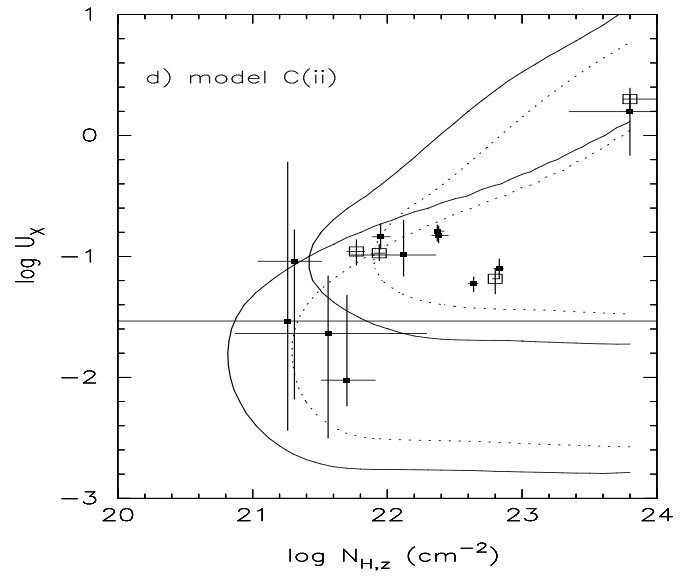
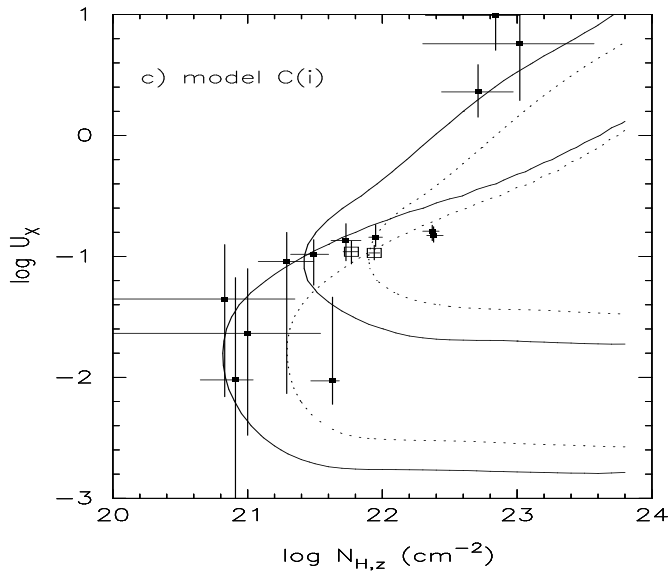
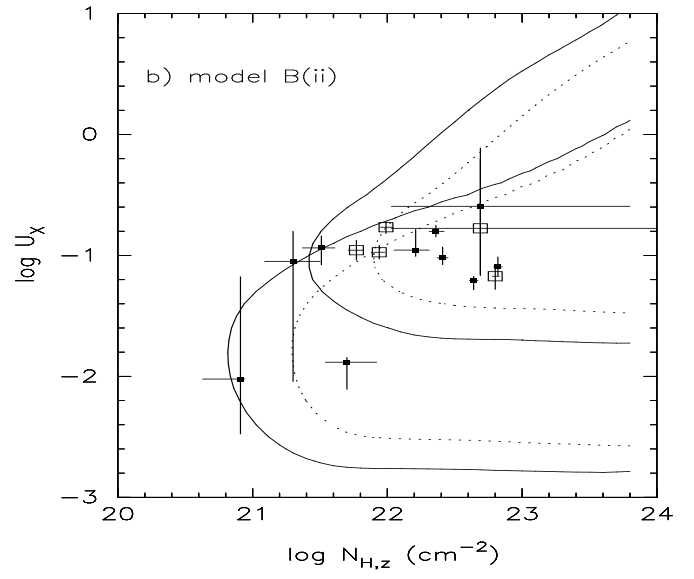
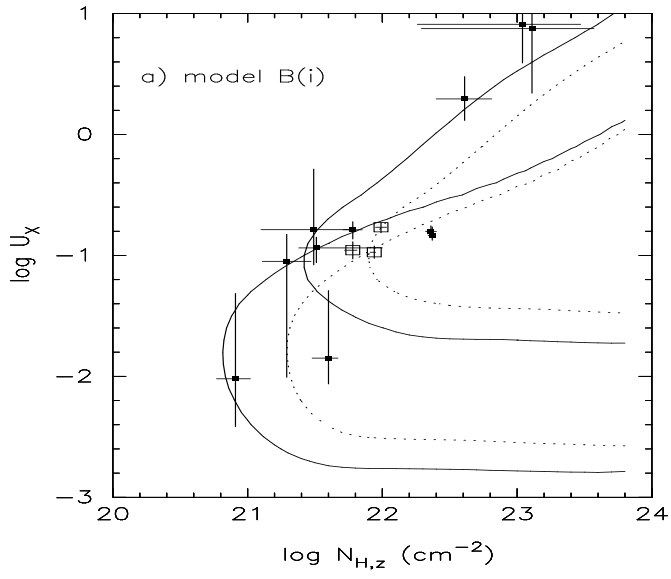
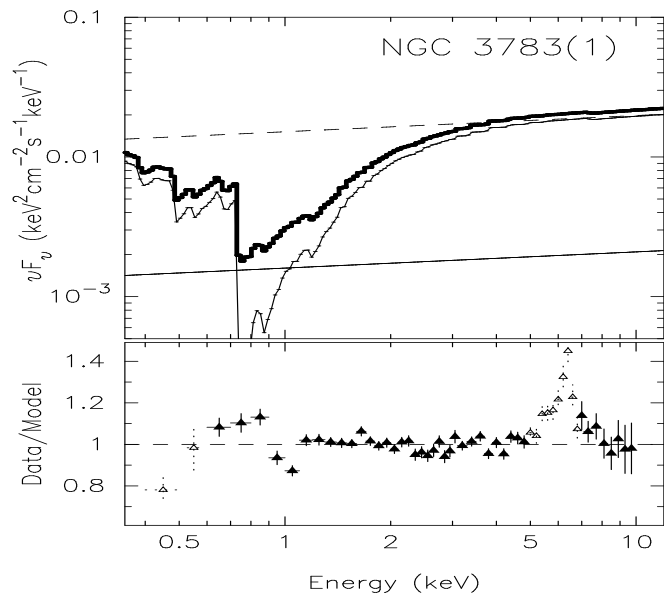


Fig. 8.—



- 105 -

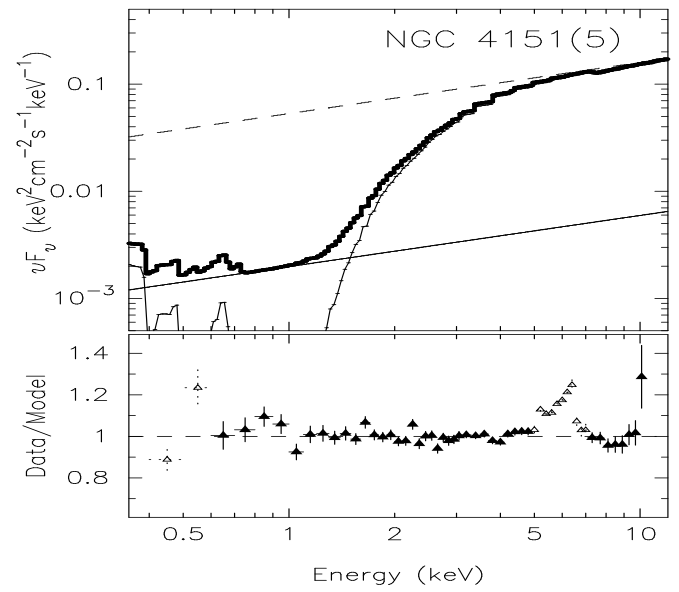
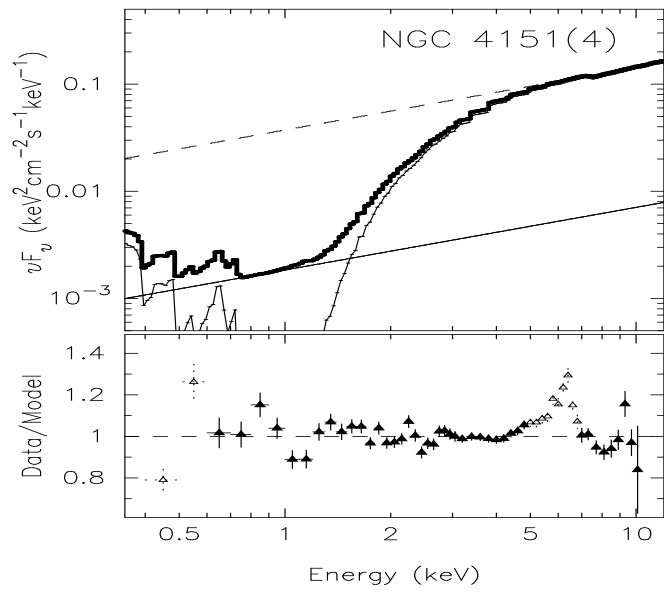
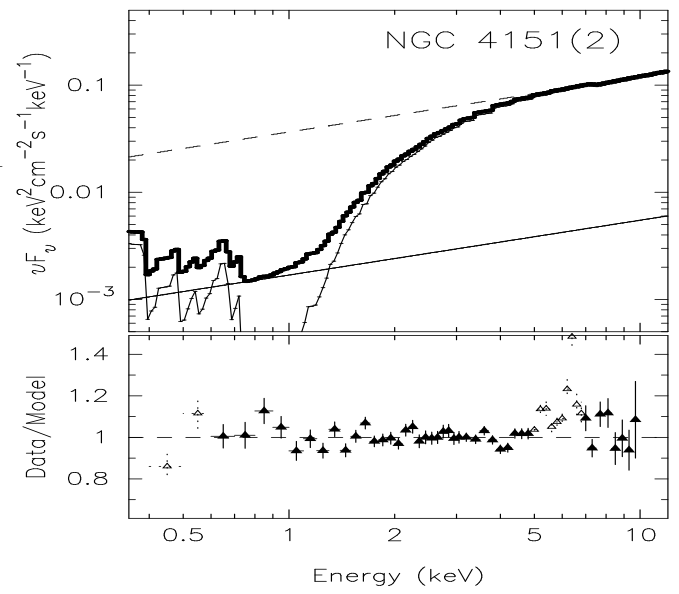


Fig. 9.—

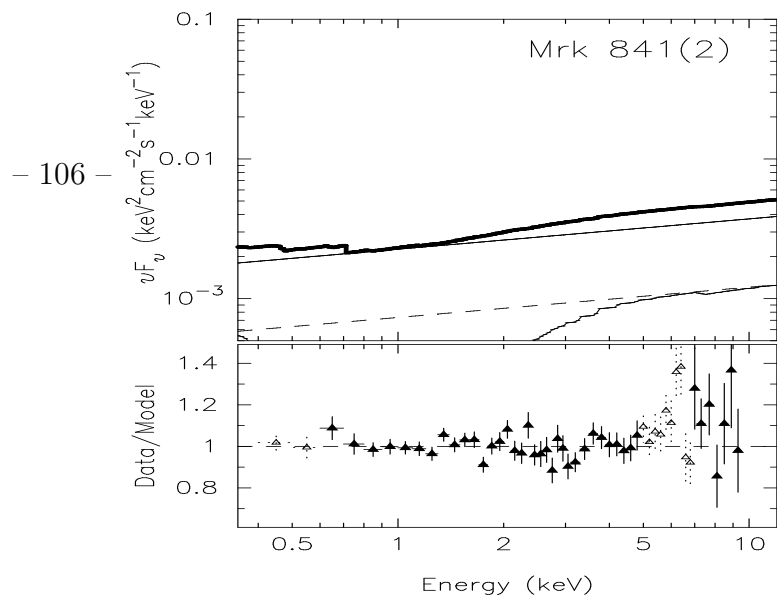
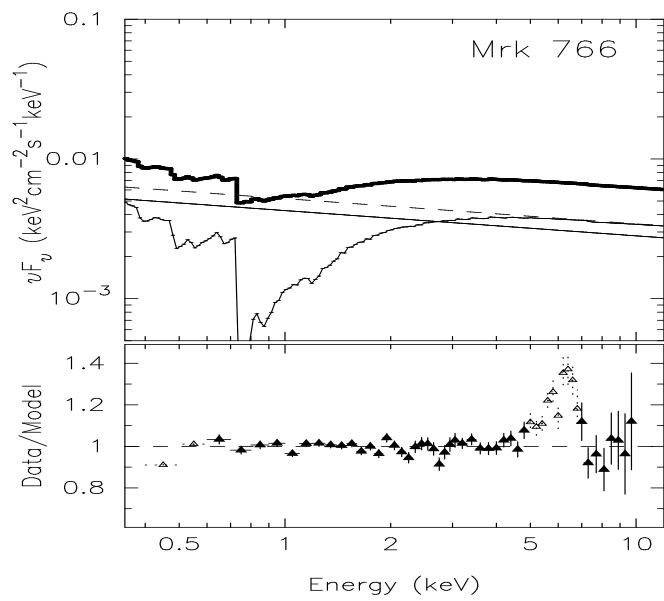


Fig. 9.— *continued*

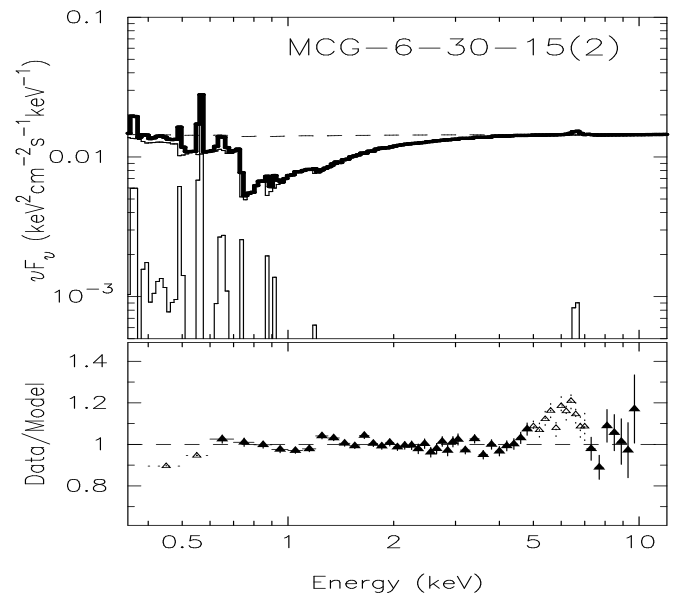
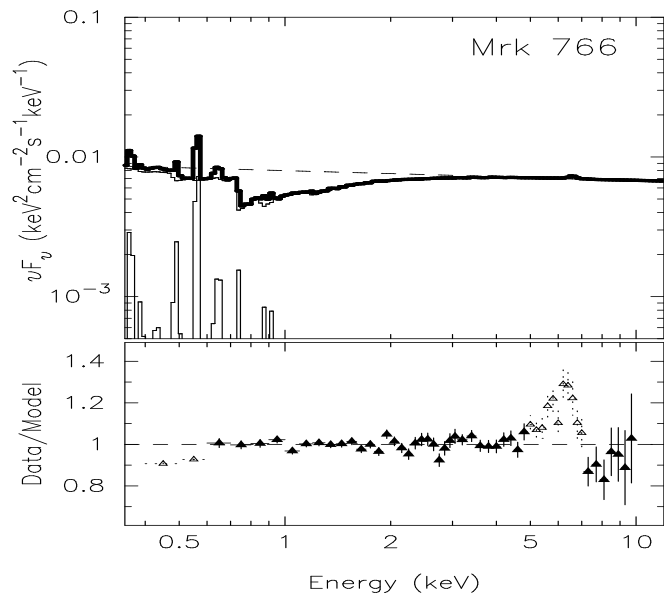
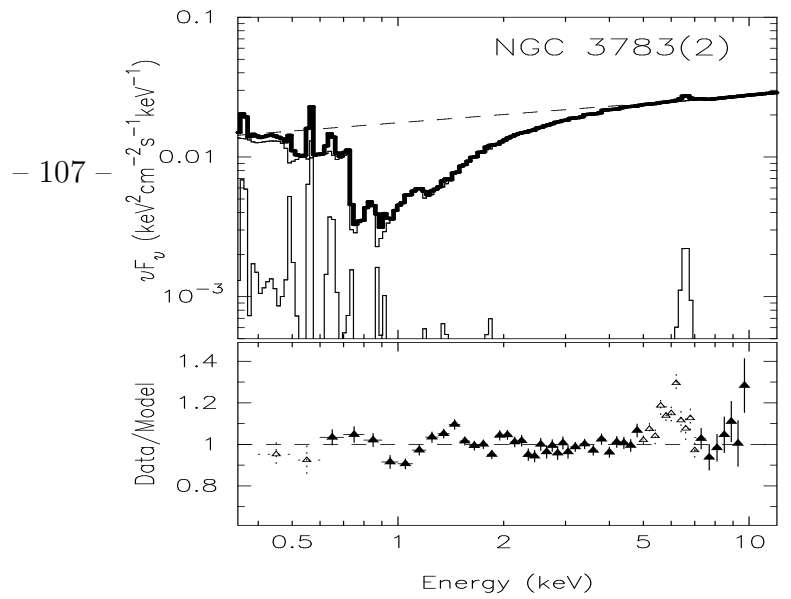
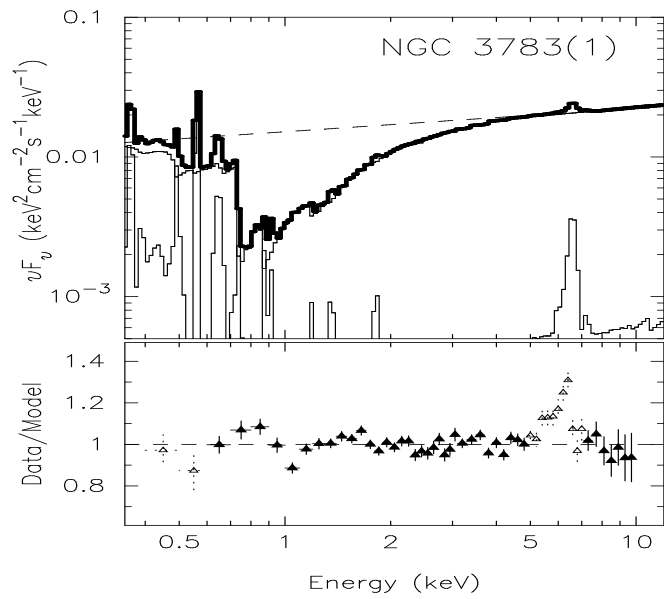


Fig. 10.—

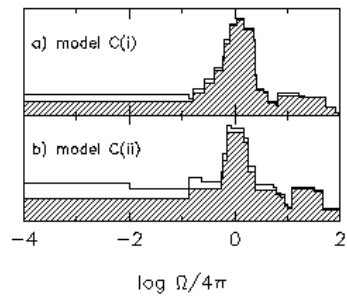


Fig. 11.—

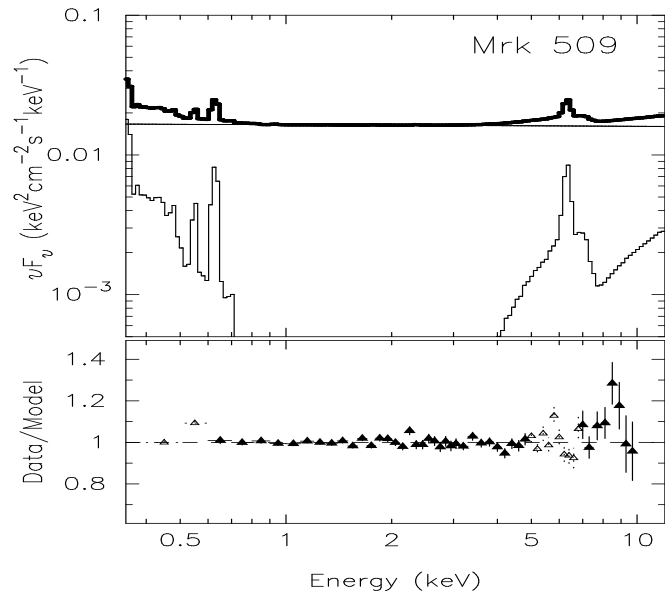
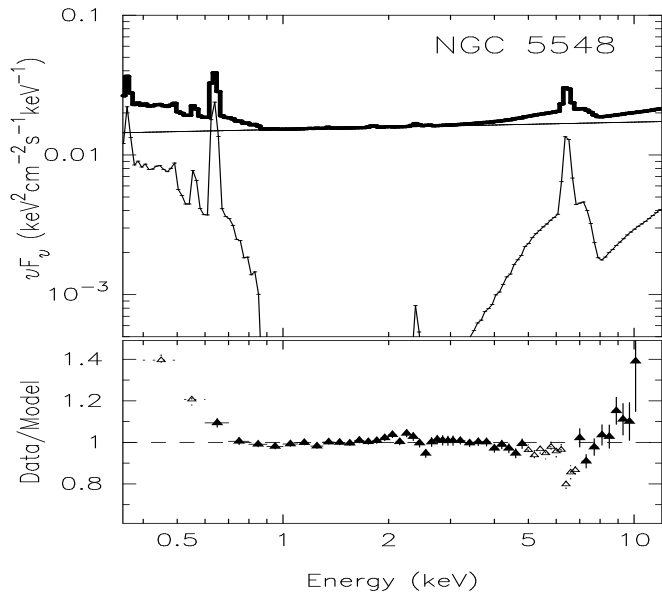
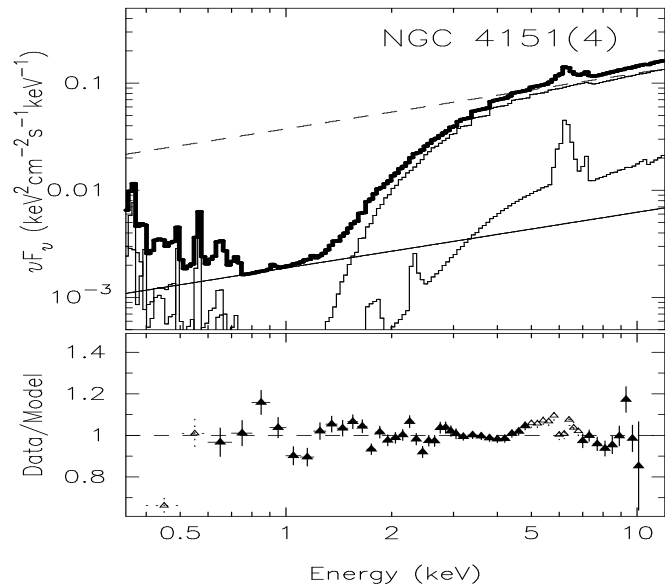
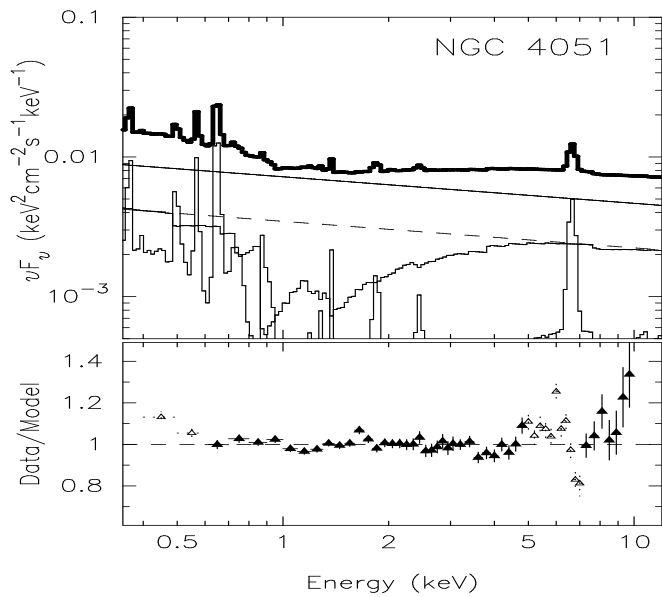


Fig. 12.—

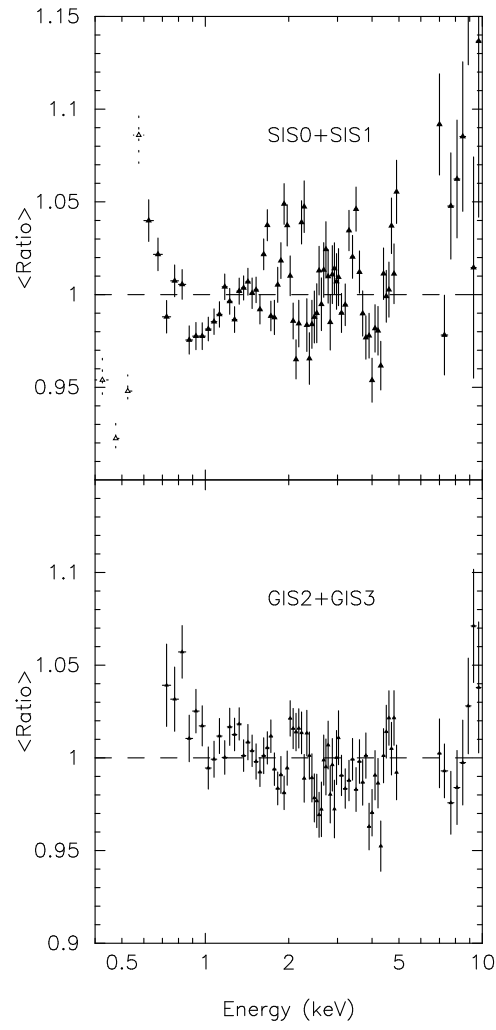


Fig. 13.—

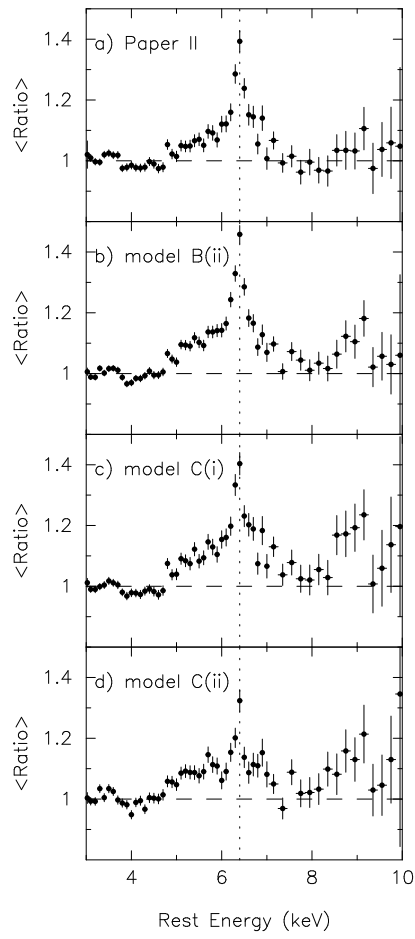


Fig. 14.—

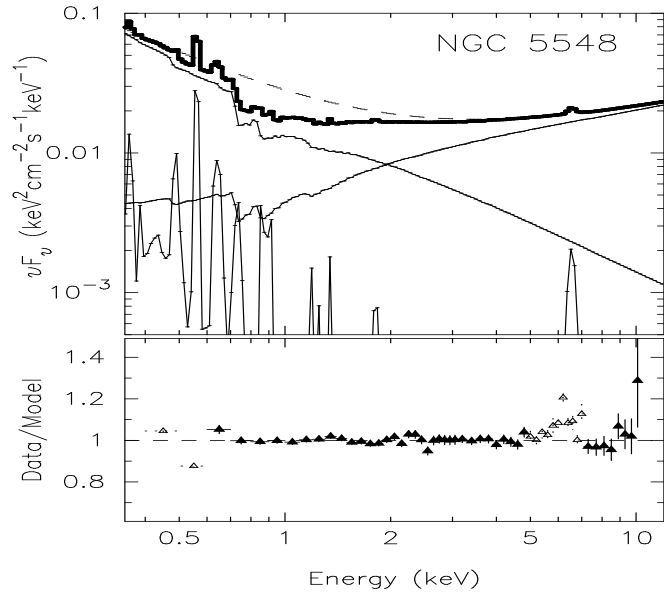
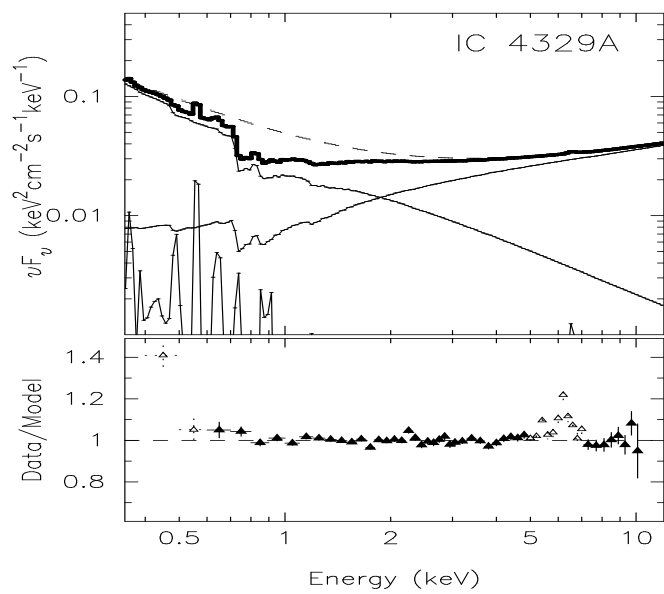
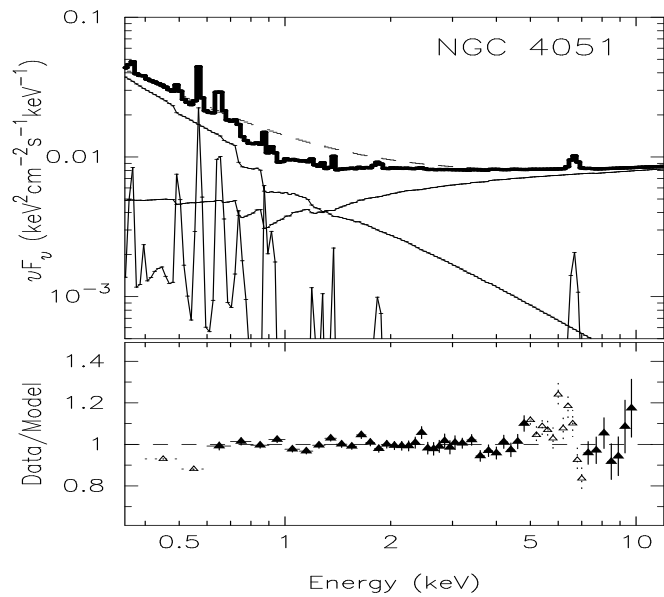
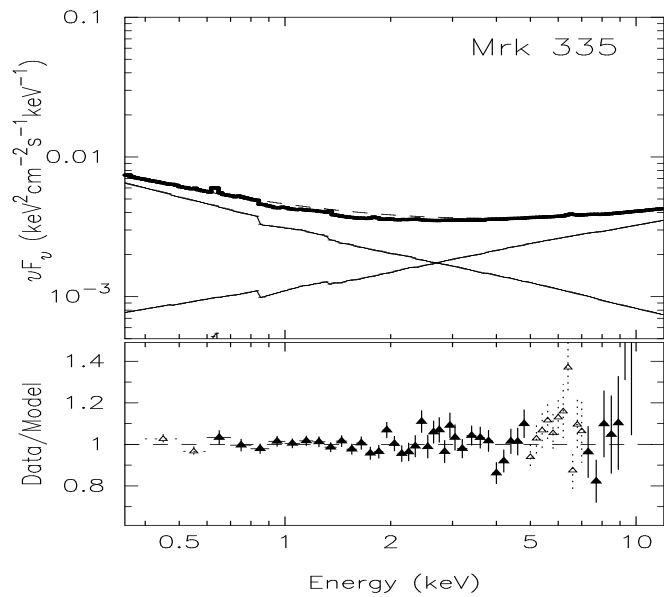


Fig. 15.—

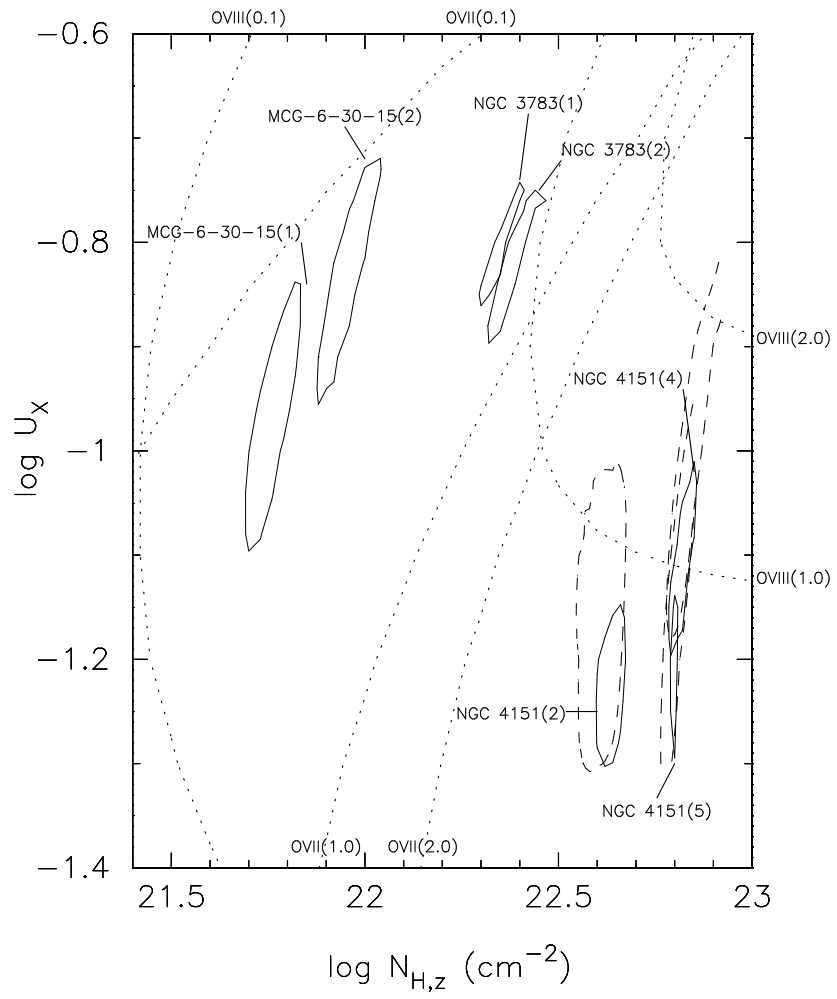


Fig. 16.—

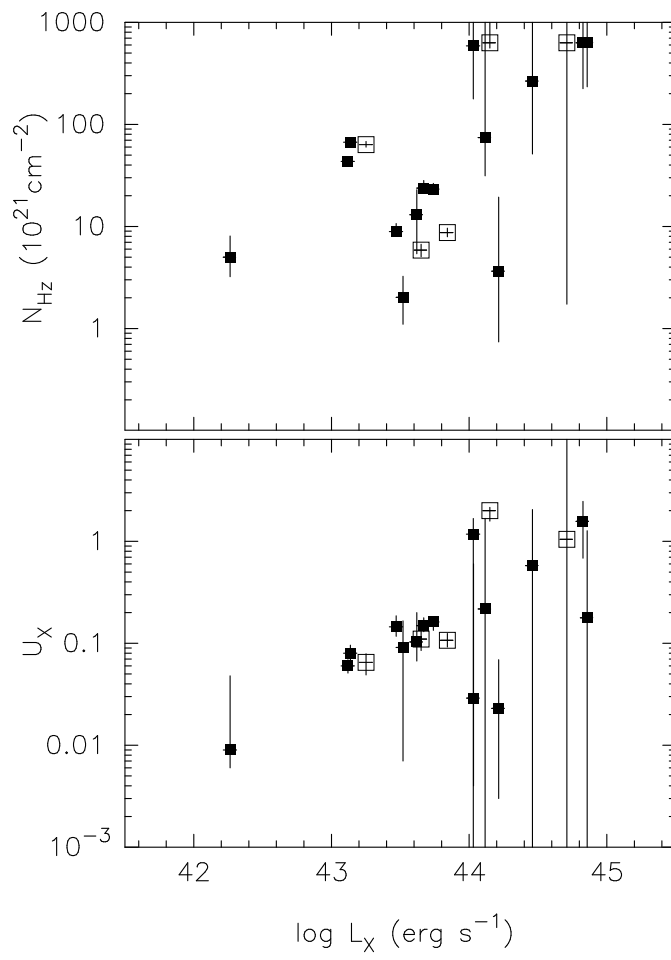


Fig. 17.—

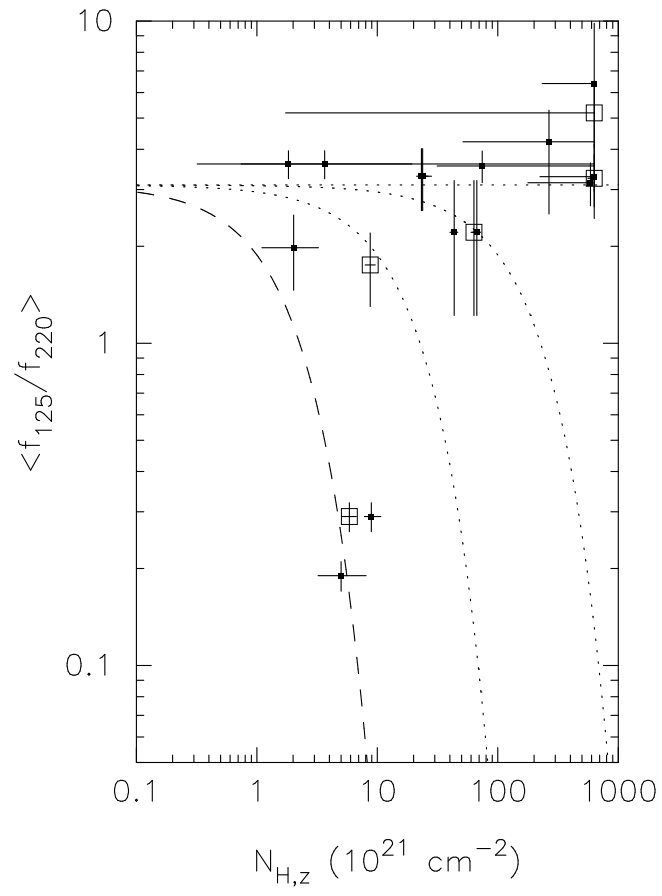


Fig. 18.—